HARVARD UNIVERSITY
Graduate School of Arts and Sciences

DISSERTATION ACCEPTANCE CERTIFICATE

The undersigned, appointed by the

Committee on Higher Degrees in Biophysics

have examined a dissertation entitled

All-optical neurophysiology using high-speed wide-area optical sectioning

presented by **Vicente José Parot**

candidate for the degree of Doctor of Philosophy and hereby certify that it is worthy of acceptance.

Signature _____

Typed name: Prof. David A. Boas

Signature _____

Typed name: Prof. Florian Engert

Signature _____

Typed name: Prof. Bence P. Ölveczky

Signature _____

Typed name: Prof. James M. Hogle

Date: May 9, 2019

All-optical neurophysiology using high-speed wide-area optical sectioning

A DISSERTATION PRESENTED
BY
VICENTE JOSÉ PAROT
TO
THE COMMITTEE ON HIGHER DEGREES IN BIOPHYSICS

IN PARTIAL FULFILLMENT OF THE REQUIREMENTS
FOR THE DEGREE OF
DOCTOR OF PHILOSOPHY
IN THE SUBJECT OF
BIOPHYSICS

HARVARD UNIVERSITY
CAMBRIDGE, MASSACHUSETTS
MAY 2019

© 2019 – Vicente José Parot
all rights reserved.

Dissertation advisor: Adam Ezra Cohen Vicente José Parot

All-optical neurophysiology using high-speed wide-area optical sectioning

Abstract

During my graduate work, I developed and applied optical and optogenetic methods to map neuronal function across large regions of the brain with single-cell resolution using high-speed optical sectioning.

I first introduce an all-optical assay to map neuronal function over large areas of brain tissue. The spectral overlap of optogenetic actuators and reporters challenges their simultaneous use, and optical scattering in brain tissue impedes high resolution fluorescence activity recordings. Spectral crosstalk was minimized by combining an optimized variant, eTsChR, of the most blue-shifted channelrhodopsin, with a nuclear-localized red-shifted Ca^{2+} indicator, H2B-jRGECO1a. Wide-area optically sectioned imaging in tissue was achieved with a structured illumination technique that uses orthogonal codes to encode spatial information, named Hadamard microscopy. The combination of eTsChR and H2B-jRGECO1a with Hadamard microscopy allowed wide-area maps of neuronal function spanning cortex and striatum. These tools were applied to probe the effects of antiepileptic drugs on neural excitability and the effects of AMPA and NMDA receptor blockers on functional connectivity.

Then I introduce a high-speed imaging extension for wide-area all-optical neurophysiology. Hadamard microscopy achieves optical sectioning via differential modulation of in-focus and

out-of-focus contributions to an image. Multiple wide-field camera images are analyzed to create an image of the focal plane. The requirement for multiple camera frames per image entails a loss of temporal resolution compared to conventional wide-field imaging. A new computational structured illumination imaging scheme, compressed Hadamard imaging, achieved simultaneously high spatial and temporal resolution for optical sectioning of 3D samples with low-rank dynamics (e.g. neurons labeled with fluorescent activity reporters). The technique was validated with numerical simulations, and then illustrated with wide-area optically sectioned recordings of membrane voltage dynamics in *ex vivo* mouse brain tissue and of calcium dynamics in live zebrafish brain. Finally, compressed Hadamard imaging enabled high-speed wide-area all-optical neurophysiology mapping of acute mouse brain slices.

The combination of éTsChR with jRGECO allows concurrent stimulation and recording of neuronal activity. Compressed Hadamard microscopy enables high-speed, high resolution optical sectioning in wide-area measurements of densely labeled fluorescent neural activity in scattering brain tissue. Together, these tools provide a powerful capability for wide-area mapping of neuronal excitability and functional connectivity in brain tissue.

Contents

Author List

Chapter 1 was written by V. J. Parot.

The following authors contributed to **Chapter 2**: S. L. Farhi[*], V. J. Parot[*], A. Grama, M. Yamagata, A. S. Abdelfattah, Y. Adam, S. Lou, J. J. Kim, R. E. Campbell, D. D. Cox, and A. E. Cohen.

The following authors contributed to **Chapter 3**: V. J. Parot[†], C. Sing-Long[†], Y. Adam, U. L. Böhm, L. Z. Fan, S. L. Farhi, and A. E. Cohen.

Contributions are further detailed at the end of Chapters **2** and **3**.

[*]These authors contributed equally.
[†]These authors contributed equally.

List of Figures

List of Tables

List of Algorithms

To my family.

Acknowledgments

First I want to thank God and my parents Sergio Parot and Sarita Fernandez for the gratuitous opportunities that enabled my curiosity. They continue to be a source of motivation.

No part of this work would have been possible without the unconditional support from my wife Cote Achurra and my children Vicente Jr. and Laura, who learned neuroscience with me and provided a firm anchor and motivation for life outside the Lab. I thank the rest of my family who also encouraged me along the way, especially my fellow expatriate scientists Julio Fernandez and Carmenlu Badilla who received us so many times at their home.

I want to thank Adam Cohen for being a kind and supportive advisor, for sharing his overflowing excitement and ideas, for many teaching moments, for help with technical debugging, for partaking in project explorations, for being a celebrator of achievements, and for teaching all-optical electrophysiology in Spanish to my nephews and nieces.

I am grateful to members of the Cohen Lab with whom I interacted, especially to Sami Farhi who was an indefatigable partner through experiments and revisions. Many others at the Lab were patient teachers and a source of inspiration. I had short interactions with Joel Kralj, Daniel Hochbaum, and Peng Zou. Kit Werley was my beacon of optical engineering. Shan Lou introduced me to genetics and molecular biology with a big heart. Miao-Ping Chien and Daan Brinks provided proper chemistry, physics-oriented wetlab skills, and cheerful companionship. Yoav Adam shared his neuroscience and his learning throughout our endeavors. Other grad students at

the Lab –in addition to Sami– kindly shared with me their years of learning: Linlin Fan, Harry McNamara, and Hao Wu. I thank Carlos Sing-Long for helpful collaboration during his visit. Many others at the Lab endured my questions, provided assistance, and maintained a stimulating environment: He Tian, Urs Böhm, Shane Nichols, Guilherme Silva, Zheng Shi, Benjamin Gmeiner, Simon Kheifets, Haitan Xu, Hongkang Zhang, Liz Wood, Xin Tang, Michael Xie, Yoree Ha, Amanda Klaeger, Eli Weinstein, Hanan Dache, Shahinoor Begum, Katherine Williams, Melinda Lee, and Vaibhav Joshi. I am also indebted to Maggie Kenar for assistance and counsel. I am also grateful to the Howard Hughes Medical Institute and to the Harvard Chemistry Department.

I extend my gratitude to all who were my mentors, teachers, collaborators, and committee members during these years in Boston who indirectly enabled this work, including: Elfar Adalsteinsson, Martha Gray, Ben Vakoc, Brett Bouma, Collin Stultz, Jacob Hooker, Giovanni Traverso, Nick Durr, Joaquin Lopez Herraiz, Eduardo Lage, Shivang Dave, Daryl Lim, German Gonzalez, Nao Uchida, Bence Ölveczky, David Boas, and Florian Engert. I also thank my graduate classmates, who contributed to make of these years an enjoyable and memorable experience.

I am indebted to Jim Hogle and Michele Jakoulov for institutional support and funding through the Harvard Biophysics Program.

I also thank Emery Brown, Wolfram Goessling, Traci Anderson, Laurie Ward, Joe Stein, and Patty Cunningham, for supporting me as their student in the Medical Physics and Medical Engineering program, at the Harvard–MIT division of Health Sciences and Technology.

I thank the Harvard Brain Initiative for funding of a Young Scientist Development Award.

I thank the Chilean government for funding through the Becas Chile program.

Observar sin pensar es tan peligroso como pensar sin observar.

Santiago Ramón y Cajal[1]

1

Introduction

Neuroscience research is accelerating with the adoption of optical methods to measure and modify neuronal activity. Optical tools have been usually applied at high magnification in small areas of tissue, and they have proved useful to uncover neurobiology mechanisms in neurons, synapses, and neuronal circuits. The goal of my PhD work is to expand the toolbox available for neuroscience research by creating protocols and methods for all-optical mapping of neuronal function in large areas of brain tissue. Here I review the fundamental principles for this application, and provide context and examples of related work.

1.1 Microscopy

While optical interrogation of biological tissues can be tuned to specific functional information of interest, one general difficulty is to localize and distinguish signals to achieve spatial specificity. Optical sectioning is the ability to discriminate signals as a function of depth, thereby achieving axial localization[2]. In this Section I review principles of biological optics as relevant to fluorescence microscopy and optical sectioning.

1.1.1 Interaction of visible light with biological matter

Visible light travels through biological tissues until their energy is deposited by absorption, or until photons are affected by scattering.

In uniformly opaque materials, light is absorbed with constant probability as it travels, resulting in transmitted intensity decaying exponentially with optical path length z following Beer's law,

$$I(z) = I_0 e^{-\mu_a z}$$

where I_0 is the incident intensity and the absorption coefficient μ_a is the inverse of the mean free path, i.e. average distance traveled between interactions. Absorption by the electronic resonance of chromophores at a broad peak of wavelengths causes transition to an electronic excited state that can spontaneously lead to vibrational dissipation as heat or sound (photothermal or photoacoustic), to chemical reactions (photochemistry), or to luminiscence (photoluminiscence).

Photoluminiscence can be further grouped in fluorescence, from singlet excited states, which is fast (nanoseconds) and has a lower energy than absorbed (typically ~10% lower); or phosphorescence, from tripled excited states where vibrational decay into forbidden states and inter-system crossing leads to longer and more variable lifetimes (milliseconds to hours)[3]. The bulk effect of many individual photons at low light intensity is the linear superposition of their individual effects. At high levels of intensity, multiple photons can deposit their combined energy, with a probability dependent on the presence of each photon independently, and thus the effect is nonlinear and proportional to the intensity squared in the case of two interacting photons[4].

Scattering or dispersion of visible light in tissue is mostly elastic, caused by refractive index variations, by which photons change direction maintaining the same energy[5].

Biological tissue is comprised of water ($n = 1.33$) solutions densely packed with macromolecules (e.g. sugar solution, $n \approx 1.5$), proteins ($n \approx 1.6$), and lipids ($n \approx 1.45$), creating refractive inhomogeneities[6]. Biological structures come in a continuous range of sizes, e.g. membranes (5 nm), microtubules (20 nm), vesicles (40 nm), cilia (200 nm), mitochondria (1 μm), cell nuclei (5 μm), cell bodies (10 μm), and beyond: cells will form all sorts and sizes of tissue structures that vary in density and composition. Brain tissue mass includes about 80% water and 10% lipids[7], the lipids organized in a dense arrangement of intermingled neuronal membranes. Also, tissue surface boundaries create refractive interfaces, and myelinated axon tracts are highly anisotropic structures.

Thus photons that continue their unmodified trajectory through tissue (called ballistic photons) decrease exponentially with distance, by the compound effect of absorption and scattering

in the law,

$$I(z) = I_0 e^{-(\mu_a + \mu_s)z}$$

Scattered photons follow unpredictable trajectories that hinder sharp light focusing. The angular scattering distribution depends on the size of scattering structures. In the limit of the particles being of negligible size compared to the light wavelength, it reduces to Rayleigh scattering as light diffracted by a point dipole. But for refractive index variations in the lengthscale of light, a relevant result first obtained by Mie is the diffraction due to a dielectric sphere. This theory explains the angular dependence of the scattering cross section with particle size for given wavelength and dielectric properties.

A simplified description of tissue anisotropy is the mean scattering angle cosine, g, with which a reduced scattering coefficient can be defined $\mu_{\text{eff}} = \mu_s(1 - g)$. The brain is a mostly forward-scattering material, with $g \approx 0.9$[8], and its anisotropy can be modeled in practice by random dielectric spheres of appropriate size distribution, for example 1 μm dia. polystyrene beads in water produce $g = 0.925$ at $\lambda = 561$ nm[9,10]. Rule of thumb mean free path values for $\lambda = 500$ nm light in mouse brain tissue are 100 μm for scattering, 1 mm for reduced scattering, 1 cm for absorption; precise values are highly variable and depend on wavelength and tissue type (for example in **Chapter 2**, signal decay with depth was measured in mouse brain cortical tissue at 561 nm obtaining 27 μm in fresh tissue and 113 μm in fixed tissue), and these variations have been reviewed previously[11,5,8].

In photochemistry, an electronic excited state induced by light absorption in a chromophore

can undergo electron transfer. This produces radicals, which can then go through other chemical reactions. On the blue end of the visible spectrum, photochemistry via photo-induced electron transfer is common, as in photosynthesis in plants. Other reactions induce breakage of a molecular bond (photolysis), as in synthesis of Vitamin D mediated by ~300 nm light. Another relevant photochemical reaction is photoisomerization, by which the structure of a molecule is rearranged. This process mediates vision, where the chromophore retinal in rhodopsins undergoes photoisomerization to start the visual signaling cascade. In optogenetics, neurons are artificially made light-sensitive leveraging the same process in channelrhodopsin. Photoisomerization also mediates conversion of bilirubin in phototherapy to treat neonatal jaundice, and mediates blinking and photobleaching of fluorophores[12].

Other interactions of light with biological tissue are less frequent. The energy of visible photons (3 eV for $\lambda = 413$ nm) is smaller than that required for ionization (at least ~4 eV for Cesium atoms, and radiation is considered safe up to 10 eV[13]), smaller than most biological tissue molecular bond dissociation energies at life temperatures (except if tissue is already heated up)[14], and smaller than required for a significant Compton scattering cross section: the Klein-Nishina relation describes the angular inelastic scattering cross-section as a function of photon energy, and for visible light it vanishes, reducing to Thompson (i.e. elastic) scattering[15]. Linear inelastic scattering still occurs in biological tissue with relatively small cross sections, through the Raman[16] and Brillouin[17] effects.

1.1.2 Contrast mechanisms for biological imaging

Transmission and reflectance can be used in bright and dark field modes to generate contrast from the density and refractive index of biological samples, but as they are nonspecific, these methods are most valuable for structural characterization of a sample. Fluorescent contrast agents can be detected using color filters, and allow highly specific labeling of structural or functional information. Using continuous illumination, the linear superposition of single photons (1P) can be used to form images of an area concurrently.

By using ultrashort-pulsed laser sources, the instantaneous intensity is dramatically increased, allowing efficient multi-photon excitation. One common application is two-photon excitation (2P) fluorescence microscopy[18], but more effects that arise with higher order nonlinearities of electric susceptibility[19] through sum frequency or wave mixing are three-photon excitation[20], non-degenerate excitation[21,22], second- and third- harmonic generation[23,24], coherent anti-stokes Raman spectroscopy[16]; other effects that exploit the temporal localization of ultrashort pulses include stimulated fluorescence[25,26], stimulated Raman scattering[27], fluorescence lifetime spectroscopy[28,29], and transient absorption[30].

In neuroscience, one- and two-photon fluorescence microscopies are extensively used for structural and functional imaging; refractive index contrast under oblique illumination is commonly used to assist electrophysiology and asses neuronal health.

1.1.3 Image formation and background

In widefield microscopy, light emitted by an illuminated sample volume is collected by the objective lens and projected onto a camera (or the retina), where signals are collapsed to two dimensions and form an image.

When samples are thick, one plane of the sample is focused on the detector while the rest of the volume is defocused, giving rise to background that reduces the contrast and mixes signals from out-of-focus planes[2]. This is a general problem in microscopy and is accentuated in thick turbid samples, where scattering of light in the sample contributes to distortion of the images beyond geometric defocusing[31].

1.1.3.1 Linear optical systems

Adding incoherent sources of illumination into an optical system results in the sum of light intensity composed at an image plane. Microscopes approximate the ideal condition that image formation properties are constant across the field-of-view. These conditions allow modeling microscopes as systems linear in intensity and invariant in space, where the point spread function (PSF, impulse response of the system) completely characterizes image formation[32]. In this framework, the lens aperture is related by a 2D Fourier transform to the diffraction limited PSF that determines the system resolution and the sharpness of focused image details[33]. The PSF can be measured as the sensitivity to a particle of known unresolvable size. Diffraction theory predicts a

limit to the optical resolution[34] given by

$$\frac{\lambda}{2NA}$$

in the lateral direction, and

$$\frac{2\lambda}{NA^2}$$

in the axial direction, where NA is the objective numerical aperture. Non-linear image formation techniques (not to be confused with non-linear excitation) allow fundamentally increasing the resolution from the diffraction limit to the localization limit in single-molecule localization microscopy (PALM/STORM)[35,36] and stimulated emission depletion (STED) microscopy[25].

1.1.3.2 Noise in optical measurements

The stochastic interaction between photons and detector materials gives rise to a Markovian process in linear photon counting devices, resulting in counts of photons in an interval being random with Poisson distribution having variance equal to counts (also called 'shot' noise)[37]. Thus the signal-to-noise ratio (*SNR*) of a shot noise limited measurement of N photoelectrons is $\sqrt{N}$. Static measurements can accumulate signal to reach a desired *SNR*, but for fluorescence dynamics, temporal resolution and total intensity constraints often result in shot-noise limited measurements. Digital cameras also have a Gaussian-distributed electronic noise floor that becomes dominant for optical signals under a nominal threshold per detector.

1.1.3.3 Noise limited detection

Ultimately, time-constrained signals of interest become undetectable when the signal level decreases below the level of the noise inherent to optical detection. In tissue, light scattering decreases signal amplitudes quickly as a function depth, limiting the maximum imaging depth to ~100 μm for 1P imaging and to ~1 mm for 2P imaging.

1.1.4 Optical sectioning

Reducing the level of background to increase contrast has been a longstanding effort in microscopy. Applications in neuroscience require microscopes with simultaneously high spatial resolution, background rejection, high temporal resolution, and large field of view. The microscope should also have good light collection efficiency to make optimal use of the limited photon budget. All microscopy techniques achieve a compromise of these goals.

In widefield epifluorescence microscopy, 1P excitation and emission of fluorescence of a sample area travel through the objective that acts as condenser and collector. In this format, excitation and emission paths are separated by a dichroic mirror and excitation and emission color filters, and images are detected by a digital camera or by direct eye observation. This approach can achieve high spatial and temporal resolution, and large field of view, but because all depths of the sample are illuminated at once, background signals defocus and mix onto the detector.

To achieve optical sectioning in 3D scattering samples, one must address two physically distinct processes. First, out-of-focus fluorescence leads to a background haze, even in samples that

are refractively homogeneous. Second, light scattering off refractive inhomogeneities degrades the point-spread function, preventing formation of a diffraction-limited excitation focus within the sample, and for a fluorescent point-source within the sample, preventing formation of a diffraction-limited image in the image plane.

Optical sectioning methods differ fundamentally on whether they physically reject background light, or they subtract it in post-processing.

1.1.4.1 Physical background rejection

The confocal microscope focuses 1P excitation onto a spot in the sample, light emitted from that spot is imaged onto a pinhole, and light transmitted by the pinhole is collected on a single element photodetector. Images are formed by raster scanning the sample. The confocality of spot and pinhole allows excluding defocused or scattered light from the detector[38].

Two photon (2P) fluorescence microscopy, like confocal, produces images from a focused spot by raster scanning the sample, but a high peak intensity source (typically a Ti:Sapph near-infrared laser with ~120 fs pulse duration, 80 MHz repetition rate, and ~100 mW power) is used for efficient 2P excitation. The nonlinear excitation proportional to the intensity squared is confined to an axially localized volume, generating no fluorescence signals from outside the focal spot. Thus all collected emission is focused on the photodetector with no pinhole to maximize sensitivity, and eliminating signal loss due to emission scattering in turbid tissue[39].

Two photon and confocal microscopies provide robust optical sectioning[2,18]. However as point scanning techniques they encounter upper limits on the number of pixels recorded per sec-

ond. In a typical two-photon system with an 80 MHz pulsed laser, the maximum pixel-rate is 8×10^7/s, 5-fold lower than in an sCMOS camera. Ultimately, serial scanning is limited at the order of this rate by the fluorescence lifetime, in the order of nanoseconds[40]. Typically in two photon microscopy one dwells for several laser pulses per pixel, so the pixel-rate is correspondingly reduced. In one-photon confocal microscopy, as the scan speed increases, the illumination intensity must increase proportionally to maintain the per-pixel photon count rate. Eventually nonlinear damage processes limit the maximum illumination intensity. These limitations on pixel bandwidth impose fundamental tradeoffs in spatial resolution, temporal resolution and field of view.

Spinning-disk confocal microscopy (SDCM) is a parallel version of the confocal microscopy in which a Nipkow disk with an array of pinholes filters light from the sample illuminated with a corresponding array of spots. Synchronized rotation of the disk allows densely filling a camera detector with signal from the focal plane at a fast framerate[41].

Commercially available SDCM systems are not compatible with low-magnification, high *NA* objectives because the SDCM systems lack sufficient etendue, i.e. they cannot accommodate the full range of optical rays transmitted by the objective.

Selective plane illumination microscopy (SPIM) refers to several variations in which the excitation and collection of fluorescence travel through non-overlapping paths to reduce background fluorescence[42,43]. The SPIM geometry works best with samples accessible from multiple directions, such as zebrafish, *Drosophila* embryos, or cleared (transparent) whole mouse brains[44,45]. SPIM is not optimal for wide-field imaging of planar or near-planar samples, such as rodent brain

in slice or in vivo, due to the requirement for optical access from multiple non-overlapping sets of angles. In one alternative configuration, non-overlapping excitation and collection paths are combined through a single microscope objective[46,47]. This approach divides the numerical aperture into separate components for excitation and illumination, decreasing the spatial resolution and light collection efficiency below the optical specifications of the objective.

1.1.4.2 Computational background rejection

Computational optical sectioning methods use multiple pictures of the sample acquired with different illumination patterns to calculate a background-free image of the focal plane. These methods are implemented or readily scalable for high-speed large-area imaging configuration. In structured illumination microscopy (SIM), stripe patterns are projected in various phases and orientations and then computationally demodulated[48], however these linear patterns suffer from scattering when projected into thick turbid tissue (>15 μm), resulting in artifacts present in reconstructed images[49,50]. SIM has been shown to perform correctly in samples limited to thin tissue, single cell layers, or thick transparent 3D samples[51].

Random illumination patterns have also been used to distinguish in-plane signals from background in tissue samples: In HiLo microscopy, one image under uniform illumination and one image under structured illumination are sufficient to calculate an optical section[52]. The method is insensitive to the precise pattern used for the structured illumination, which can be random or not[53–55].

In aperture correlation microscopy, illumination goes through a mask that is imaged onto the

sample. The light emitted from the sample is imaged back to the mask, from where the transmission is imaged onto a camera, and the reflection is imaged onto another camera. Patterned light from the focal plane is only present in the transmitted image, while background and scattering are present in both. These two images are scaled and subtracted to remove the background, and multiple images with different synchronized patterns are required for uniform coverage[56,57].

Methods based on a random pattern do not require foreknowledge of the illumination pattern, and do not use it in the analysis. As a result, they cannot distinguish emitted scattered photons from ballistic ones. By selecting image components with high spatial frequencies, these methods might spuriously reject large fluorescent structures in the focal plane.

The fastest computational optical sectioning methods use a single image pair per optical section, but are further prone to artifacts derived from using spatially non-uniform total illumination. Rotation of a mask disk, or cycling through multiple mask patterns allow averaging to remediate this problem, but this degrades temporal resolution.

In **Chapter 2**, I introduce a computational optical sectioning strategy for wide-area all-optical neurophysiology, named Hadamard microscopy, that uses orthogonal encoding of illumination patterns for neighboring sample locations, improving the axial sectioning compared to other structured illumination strategies. **Chapter 3** further extends this method with a compressed measurement strategy that matches the fastest temporal resolution of existing optical sectioning methods while keeping the improved resolution.

1.1.4.3 Noise in optical sectioning

To reduce contaminating background from thick samples, optical sectioning methods reject defocused light, obtaining images of the focal plane only. Physical rejection methods avoid detecting background, while computational rejection methods subtract background in post-processing. Because the noise is independent in every realization, when background is subtracted, the noise from its optical detection still accumulates. Thus computational methods can remove the background but cannot get rid of the noise associated with its detection[58].

1.2 Molecular tools for all-optical neurophysiology

Modern neuroscience uses optical tools for neuronal activity recording and perturbation. This represents a fundamental advance in throughput and parallelism compared to classical electrophysiology using electrodes for point measurements. During my PhD I further developed optogenetic protocols for all-optical neurophysiology. Here I introduce relevant biophysical and molecular principles, and review recent advances in this area.

1.2.1 Optical recording of neuronal activity

1.2.1.1 Neurophysiology

Lipidic cell membranes are impermeable to charged solutes, enabling sustained differences in concentration of molecules and ions between cellular compartments to create specialized biochemical environments. The aggregate concentration gradients of charged species establish an electrical po-

tential across membranes, which act as an electrical insulator analogous to a parallel plate capacitor. Thus membrane voltage interacts with concentration gradients and is determinant to the flow of charged solutes, further regulated by channel and transporter proteins embedded across lipid membranes. The electrical potential across a membrane is related to each species, concentration gradient and charge by the Nernst equation.

$$E_{\text{ion}} = \frac{RT}{zF} \ln \frac{[\text{Ion}]_{\text{in}}}{[\text{Ion}]_{\text{out}}} \approx \frac{62.5}{z} \log_{10} \frac{[\text{Ion}]_{\text{in}}}{[\text{Ion}]_{\text{out}}} \qquad \text{(mV)}$$

Where E_{ion} is the equilibrium potential, $[\text{Ion}]_{\text{in}}$ and $[\text{Ion}]_{\text{out}}$ are the respective ionic concentrations, R is the ideal gas constant, T is temperature in Kelvin, and F is the Faraday constant.

Accounting for multiple ionic species, the Goldman equation relates them to the potential of a physiological membrane in equilibrium. Many cells are generally not in equilibrium, including cardiomyocytes and neurons. Voltage-dependent ion-specific channels that dynamically regulate ionic flow give rise to excitable membrane properties, in which the flow of Sodium (Na^+), Potassium (K^+), Calcium (Ca^{2+}), Chloride (Cl^-), and other charged species perform a coupled oscillation governed by nonlinear dynamics, described by Hodgkin and Huxley[59]:

$$I = C_m \frac{\mathrm{d}V_m}{\mathrm{d}t} + \sum g_i (V_m - V_i)$$

Where I is the total current across the membrane, C_m is the membrane capacitance, V_m is the membrane potential, g_i is the conductance for a particular ionic species (more generally $g_i(t, V_m)$, a nonlinear function of time and membrane potential), and V_i is the respective reversal potential.

These nonlinear oscillations give rise to action potentials, discrete excitation events that further compartmentalize cellular biochemical environments in time. The cardiac action potential synchronizes cardiomyocytes and drives its muscular contraction, one heartbeat after another throughout the whole life. Neuronal action potentials encode millisecond timescale information in the nervous system and drive intracellular Ca^{2+} increase that mediates the release of neurotransmitters at synaptic terminals. Postsynaptic neurotransmitter receptors activate ionic currents, further triggering downstream action potentials and computation.

The traditional method for electrophysiologic measurements –patch clamp– consists of controlled breaking of the cellular membrane using a glass micropipette to access its intracellular space with an electrode, enabling probing the membrane with electric perturbations, and yielding high bandwidth amplified recordings of the current and voltage across the membrane[60]. Patch clamp recordings can demonstrate the stochastic gating of single ion channel currents[61], the quantal nature of granule fusion[62] and synaptic vesicles release[63], and mechanisms of short- and long-term synaptic plasticity[64].

1.2.1.2 Genetically encoded Calcium indicators

Genetic targeting and expression of exogenous proteins is a fundamental tool that has advanced biomedical research. These techniques insert a genetic sequence into the genome of a cell, and then native cellular processes translate and transcribe this code into a protein executing some biological function. Adaptation of a natural green fluorescent protein (GFP) from jellyfish for expression in other organisms allowed specific detection of genetically encoded effector signals using

fluorescence microscopes[65]. The Ca^{2+} concentration indicator protein GCaMP was created by fusing GFP to calmodulin, a Ca^{2+}-binding protein native to eukaryotic cells[66]. Further genetic engineering by mutating the genetic code of these proteins has allowed optimization, thus giving rise to variants with increased quantum efficiency, brightness, multiple colors, and Ca^{2+}-binding affinity[67–70].

The Ca^{2+} concentration is a fundamental signal in cell biology[71], but importantly in neurons it mediates the signal transduction of action potentials and the release of neurotransmitters. Neuronal firing of action potentials increases the intracellular Ca^{2+} concentration, that accumulates and plateaus with sustained firing. Recent advances have optimized the brightness, sensitivity and contrast of Ca^{2+} reporters, and have created red-shifted variants that enable their spectral combinations with other colors.

GECIs have proved useful and are extensively used in neuroscience, however using a Ca^{2+} reporter as a marker of neuronal activity has limitations[72]. Subthreshold changes in membrane potential and inhibitory inputs are not reflected by Ca^{2+} concentration. Ca^{2+} concentration can change as result of cellular signaling or Ca^{2+} buffering not related to neuronal activity. The intensity of a Ca^{2+} reporter doesn't change linearly with neuronal activity, saturating upon sustained firing. Finally, the response time of Ca^{2+} concentration is not sufficient to register individual action potentials in most neuronal firing conditions. Thus spike timing or number of spikes cannot be straightforwardly inferred from fluorescence[73].

Currently, Ca^{2+} imaging has been highly optimized for *in vivo* behavioral experiments in multiple animal models. Using 1P excitation, new microscopy techniques have recorded the whole

animal neural activity in the worm *Caenorhabditis elegans*, and the whole brain in zebrafish[74,75]. To image the mammalian brain at depth, tissue scattering prevents 1P imaging, which has led to optimization of 2P and 3P excitation strategies for large scale and deep Ca^{2+} imaging of mice. Currently, implementations exist for random access over large fields of view[76] and for massively parallel volumetric imaging[77]. Multiple optical and computational alternatives are each best suited for particular biological questions[78].

1.2.1.3 Genetically encoded voltage indicators

Precise neuronal activity information is encoded in the membrane voltage, and the effort towards its optical recording has been long-standing[79] but hindered by multiple challenges, the main one being that action potentials can be as short as a millisecond. Thus recording strategies need to keep a high sampling rate (typically 1 kHz) against limited availability of optical signals and their inherent detection noise. Initial efforts focused on intrinsic sources of membrane potential contrast, including mechanical deformations, and changes in refractive index or birefringence. Intrinsic contrast mechanisms however cannot be targeted to record from specific neuronal subpopulations within tissue. Some small dye molecules provide bright exogenous voltage-dependent contrast[80], but are also phototoxic in addition to being non-specific. To enable genetic targeting of voltage reporters, three mechanisms of protein voltage sensing have been studied: 1) ion channels and 2) voltage sensitive phosphatases that have potential-dependent conformational changes, and 3) rhodopsin chromophores with potential-dependent protonation. Rhodopsin-based GEVIs have been applied to report action potentials and subthreshold transients in vivo in combination with

optogenetic actuators[81–83]. Nonetheless, GEVI activity recording is fundamentally more challenging than GECI activity recording because 1) voltage transients are 2-3 orders of magnitude faster than Ca^{2+} transients, 2) membrane-localized signals are sparsely and irregularly distributed in volume, and are difficult to distinguish among neurons since 95% of their membrane is optically unresolvable neuropil[84]. Presently, GEVIs are not as fast, as sensitive, or as bright as one would desire. In particular, fast and sensitive Arch-based sensors are ~50 times dimmer than EGFP, and bright VSD-based sensors are either ~10 times slower or ~10-fold less sensitive than Arch-based reporters[85].

1.2.1.4 Continued development of physiology reporters

The development of functional fluorescent indicators has expanded their applicability to many other physiological parameters beyond Ca^{2+} and voltage, including pH and vesicle release[86], cAMP[87], ADP/ATP[88], neurotransmitter concentration[89–92], and membrane tension[93]. Recent advances also enable specific subcellular localization including to organelles, the neuron soma, dendrites, and spines. Nonlinear optical photoactivation allows intersectional expression or functionalization of reporters. Protein engineering and directed evolution are being extensively used to optimize all these desired functional properties. Ongoing work advances towards activity integrators to report past neuronal activity and for replay of neuronal activity[94].

1.2.2 Optogenetic neural manipulation

Another transformative advance in contemporary neuroscience is to deliver genetically targeted, light-triggered perturbations of neuronal activity. Channelrhodopsin is a light-sensitive ion channel originally found in algae to control light driven locomotion, in which photon absorption by the endogenous chromophore retinal inside channelrhodopsin triggers a conformational change opening a conductance to ionic flow and leading to membrane depolarization[95]. Its expression in other organisms allows optical control of neural activity by triggering action potentials upon light-triggered neuronal depolarization in genetically targeted neuronal subpopulations. A number of channelrhodopsin variants have been optimized for functional properties including photocurrent, sensitivity, kinetics, and expression patterns, and complementary strategies have been developed to stimulate neuronal inhibition and ion-specific conductances[96].

This genetic specificity of optogenetic perturbations enables causal investigation of neurobiological mechanisms and animal behaviors. The classic behavioral optogenetic stimulation experiment defines a behavior-associated neuronal subpopulation by expression of a genetic marker. Optogenetic actuator expression driven by the marker is then used in separate experiments to specifically trigger artificial 1) stimulation and 2) silencing of the behavior, thereby verifying the neuronal subpopulation is 1) sufficient and 2) necessary for the behavior[97]. Alternatively, optogenetic perturbation is performed in an array of areas to causally map behavioral perturbations[98].

The revolutionary advances enabled during the first decade of optogenetics used 1P excitation and were largely devoid of precise spatial localization; their significance rested on the genetic tar-

geting of neuronal subpopulations. Only recently, high spatiotemporal precision was added to the toolbox of optogenetic stimulation. Compared to 2P Ca^{2+} imaging, 2P channelrhodopsin activation is fundamentally more difficult, owing to the sparse localization of the membrane proteins in tissue. Scanning of a 2P excitation beam can open channels along a contour or spiral, but then the low duty cycle of excitation on each point demands higher photocurrents per channel protein to achieve threshold levels of neuronal activation. Single cell targeting is challenged by the dense vicinity of neurons in tissue.

Optimization of optical techniques and molecular tools have advanced temporally precise single cell stimulation[99], holographic excitation[100], optogenetic inhibition[101], and spectral compatibility[102]. The library of opsins for precise stimulation is rapidly expanding[103].

Present strategies that optimize targeted optogenetic stimulation incorporate subcellular localization of the channelrhodopsin to the neuronal soma, mutations to enhance channelrhodopsin photocurrents, and lower repetiton rate lasers that allow a higher peak intensity at a set power level.

1.2.3 Simultaneous optical stimulation and recording

Activity recordings and optogenetic stimulation have both been independently valuable and fullfil complementary roles[98,104]. However, neurophysiology* can be further explored by simultaneously combining optical perturbation and measurement of activity, more than by using either

*Neurophysiology refers generally to neuronal biology, whereas electrophysiology refers more specifically to the membrane potential biology. In the context of optical neural activity recordings, the distinction applies to using Ca^{2+} or voltage indicators: while both probe cell biology, Ca^{2+} does not directly probe membrane potential.

approach separately. Simultaneous manipulation of inputs and measurement of outputs allow characterization of systems to build simplified models through experimental testing of responses to controlled inputs. All-optical manipulation allows electrophysiological characterization of neural circuits under different neuronal depolarization conditions. Finally, closed loop all-optical neural interfaces enable study under dynamic control conditions.

1.2.3.1 All-optical neurophysiology

The fundamental difficulty to implement simultaneous all-optical neurophysiology is the spectral overlap of broad-peaked optogenetic actuators and reporters. The common sensitivity to wavelengths of light hinders the ability to measure activity without inducing optogenetic stimulation, and also can introduce stimulation-induced artifacts in activity recordings. Other important aspects are 1) the design of question-optimized optical and computation systems with technical capability for precise localization in space and in time of both stimulation and recording, which can be especially challenging for *in vivo* studies, 2) the dynamics of actuator and reporter activation and deactivation times need to be fast enough to probe stimulation or activity regimes of interest, 3) joint packaging of constructs for actuator and reporter in a single virus restricts their coding sequence length, 4) expression of actuator and reporter in specific neuronal populations requires custom targeting strategies, and 4) large-scale optical parallelism requires special strategies for individual cell perturbation and recording[105].

Recent progress has installed all-optical neurophysiology as an available tool for live mice behavioral studies. Using 1P excitation, lightweight microscopes allow studies on freely moving an-

imals[106]. In head fixed animals, single-cell targeted 2P-excitation of stimulation and Ca^{2+} recording has been applied[107–109] and further optimized for parallel 3D precise localization[110–113]. In these implementations, spectral separation and crosstalk with Ca^{2+} reporters remains a challenge: channelrhodopsin is efficiently activated by GCaMP excitation wavelengths. Thus strategies use either red-shifted opsins, or red-shifted Ca^{2+} reporters. In either case, imaging excitation intensities operate close to the limit of channelrhodopsin activation. The high excitation power required for parallel 2P excitation limits these methods to < 100 cells concurrently to avoid excessive brain heating[114,115].

For all-optical electrophysiology, Optopatch[81,82] combines an infrared rhodopsin-based voltage reporter with blue-excited channelrhodopsins, achieving good spectral separation, and enabling *in vitro*[116] and *in vivo*[83,117] crosstalk-free temporally precise studies of subthreshold membrane potential in single neurons using 1P excitation.

A further technical advance is the ability to close the loop of all optical stimulation and recording[118,119], which enables on-line feedback of signals into the system under study.

All-optical neurophysiology has been highly optimized for behavioral sudies in awake mice. However, *ex vivo* experiments in acute brain slices continue to be an essential tool to access any brain region and probe neuronal microcircuits in their native tissue environment.

Expanding the scale of all-optical neurophysiology for large tissue areas holds the promise to parallelize slice neurophysiology and enable new, area-based applications, e.g. to find rare cell populations, to characterize subtle gradients undetectable in small areas, and to measure many cells or areas of the brain in parallel matched conditions.

Chapters **2** and **3** describe a new strategy to stimulate (with a common stimulus) and record (with single cell resolution) thousands of cells in parallel from large areas of brain tissue in acute brain slices.

1.2.4 Systems modeling of all-optical neurophysiology

As in the analysis of electrical systems, a natural characterization of neurobiological model systems –and of experiments to test them– is according to how many inputs and outputs do they have. Single or Multiple Input and Output give rise to four categories: SISO, SIMO, MISO, MIMO. Many classical electrophysiology experiments fit appropriately into these categories depending on how many patch electrodes are used, most commonly using one perturbation electrode and one (SISO) or multiple readouts (SIMO).

In systems neuroscience, classical engineering modeling is an essential tool to study neural circuits[120,118]. In the context of all-optical neurophysiology tools, several factors merit revisiting this model-building classification: 1) even small neurobiological models are fundamentally complex because they are highly nonlinear and with memory, 2) understanding the brain and behavioral functions will likely require complex models, 3) the ability to probe genetically labeled neuronal subpopulations allows independent input/output experiments to build complex unified models, 4) varied optogenetic expression strategies give rise to different vistas to probe a common system.

All-optical neurophysiology experiments probe neuronal subpopulations, independently defined for stimulation and recording. Neuron groups under study are defined by intersectional combination of A1) neurons expressing a genetic marker, A2) neurons defined by spatial prop-

erties, A3) neurons defined by functional properties (such as a synaptic connection), A4) sparse inclusion of neurons. Spatial properties are notably flexible and can even be defined in transient developmental stages, they include A2.1) localization of the neuron soma, A2.2) projection target, A2.3) dendrite innervation area, A2.4) migration origin. Similarly, functional definition includes neurons having a monosynaptic common population A3.1) downstream, and A3.2) upstream, or A3.3) a particular firing pattern. Within those defined populations, perturbations can target B1) a single cell or B2) multiple cells. If multiple cells are stimulated, this can be further classified as B2.1) a targeted region lacking single-cell resolution, B2.2) sparsely defined neuronal ensembles, B2.3) all cells in the population.

Analogous classification can be applied to the target population whose activity is being recorded, resulting in C1 single cell, C2.1 regional, C2.2 ensemble, C2.3 universal. Furthermore, B2 can be specified to be one perturbation acting on a group of cells, individually addressed concurrent perturbations to multiple cells, or spatially patterned perturbation lacking single cell resolution; The entire C classification can separate in parallel multiple distinct recordings, or in mixed or bucket recordings that can be unmixed in post-processing.

Broad classes of applications stand out by the definition of their target populations under study. Targeting the same population with optogenetic stimulation and readout allows probing the intrinsic excitability of neurons, and allows driving neurons to different states to probe their differential modulation by sensory inputs. Targeting actuator and reporter to defined and mutually exclusive populations for allows testing the functional connectivty between these neuronal subpopulations.

Finally, systems neuroscience is concerned with understanding neurological mechanisms that translate sensory input to behavioral output. For behavioral experiments, a similar and independent classification of models can be followed, considering that a general model for an organism will include as a subset a neurophysiological model under study. Thus the organism model can have zero, single, or multiple sensory inputs, and zero, single, or multiple behavioral outputs (SISO/MIMO). The neurophysiological model could interface with inputs, outputs or internal states of the organism model.

For example, an experimental model of cortical neural network organization in mice[113] uses visual stimulation, optically perturbs activity in multiple singly targeted cells, and optically records activity from multiple cells of the same cell population concurrently. There is no monitoring of behavioral output. The organism model interface is SIZO (single input, zero outputs), interacting with a MIMO neurobiologic model. The all-optical interface could be classified as A1, B1 sequential, C1 parallel.

In another example, an experimental model of attention in mice[117] incorporates mechanical whisker stimulation and air puffs to the face, optically perturbs multiple regional sites of optogenetic stimulation to L1 interneurons, optically records from multiple L1 interneurons under study individually at different times, and monitors pupillary diameter and licking frequency, modeling an organismic MIMO system, including a neurophysiological MIMO system, further classified as A1/A2.1, B2.1 concurrent, C1 sequential.

Whereas in regular and optogenetic-assisted classical electrophysiology SISO, SIMO and MISO probing has resulted in the bulk of advances due to the individual nature of patch-clamp

probing, optical approaches started from bulk nonspecific probing, transitioning to single cell resolution after further technology advances. The all-optical SISO case is technically challenging and implementations so far provide complementary information, but do not replace SISO patch-clamp experiments. The broad opportunity of all-optical approaches is the fundamental parallelism that can be achieved, and one of challenge is to design experiments that appropriately exploit these advantages for particular biological questions.

The brain is a tissue. It is a complicated, intricately woven tissue, like nothing else we know of in the universe.

David H. Hubel[121]

2

Wide-area all-optical neurophysiology in acute brain slices

Optical tools for simultaneous perturbation and measurement of neural activity open the possibility of mapping neural function over wide areas of brain tissue. However, spectral overlap of actuators and reporters presents a challenge for their simultaneous use, and optical scattering and out-of-focus fluorescence in tissue degrade resolution. To minimize optical crosstalk, we combined an optimized variant (eTsChR) of the most blue-shifted channelrhod-

opsin reported to-date with a nuclear-localized red-shifted Ca^{2+} indicator, H2B-jRGECO1a. To perform wide-area optically sectioned imaging in tissue, we designed a structured illumination technique that uses Hadamard matrices to encode spatial information. By combining these molecular and optical approaches we made wide-area functional maps in acute brain slices from mice of both sexes. The maps spanned cortex and striatum and probed the effects of antiepileptic drugs on neural excitability and on the effects of AMPA and NMDA receptor blockers on functional connectivity. Together, these tools provide a powerful capability for wide-area mapping of neuronal excitability and functional connectivity in acute brain slices.

Significance Statement

A new technique for simultaneous optogenetic stimulation and calcium imaging across wide areas of brain slice enables high-throughput mapping of neuronal excitability and synaptic transmission.

2.1 Introduction

All-optical neurophysiology (AON)—simultaneous optical stimulation and optical readout of neural activity—provides a promising approach to mapping neural excitability and functional connectivity across wide regions of brain tissue[122,100]. Recent advances in two-photon (2P) calcium imaging AON *in vivo* have enabled measurement of neuronal population activity while stimulating or inhibiting up to ~100 near-surface neurons in small cortical regions[99,100,112]. However,

most of the intact rodent brain remains inaccessible to optical microscopy, and one would ideally like to perform AON simultaneously on many thousands of neurons across multiple brain regions to map spatial variations in function or to detect rare sub-populations.

Acute brain slices in principle enable wide-area optical mapping across any brain region. While slicing cuts many long-range connections, the procedure is commonly used to investigate the molecular makeup, electrophysiological properties, and local microcircuitry of the component neurons[123]. Wide-area AON in acute slices would enable several types of new applications. Pharmacological studies with tool compounds could probe the distribution and functional roles of receptors or channels in the tissue, e.g. to characterize the nature of synaptic connections between specific brain regions; or to discover cell populations that expresses a receptor for an orphan ligand[124–127]. Tests with candidate drugs could probe the distribution and functional consequences of drug action. Further potential applications include probing the response of brain tissue to physical or chemical perturbations, e.g. to map responses to changes in nutrients, hormones, oxygen, or temperature. In all these applications, a large field of view (FOV) for simultaneous large-area imaging is essential because the sample response might adapt or degrade, and physiology may vary as a function of time post perturbation.

Brain slices typically show little spontaneous activity and obviously lack sensory inputs, so optical mapping in brain slices requires a means to evoke activity. Optogenetic stimulation can directly evoke activity in the measured neurons, or can activate axon terminals—even when the axons have been severed from the cell bodies—and evoke postsynaptic responses[128]. Optical readouts of evoked response could reveal the spatial structure of intrinsic neuronal excitability, of functional

connectivity, or of local microcircuit dynamics, and molecular or physical influences thereon.

The optical requirements of wide-area AON in brain slice differ from *in vivo*, suggesting that a distinct approach could be warranted. In brain slice there is a benefit to having a very wide field of view to probe many neurons and brain regions simultaneously. Optical sectioning is important to distinguish in-focus cells from background, but imaging deep ($> 100\ \mu$m) into the preparation is less important than *in vivo* because the plane of the slice can expose any brain structure of interest. One may wish to stimulate many thousands of cells simultaneously, a task beyond the capabilities of current 2P stimulation techniques. If one treats cells as units, the spatial resolution must be sufficient to resolve single cells, but need not resolve fine sub-cellular structures. Time resolution must be sufficient to resolve dynamics slice wide, typically < 200 ms for Ca^{2+} imaging. These factors, discussed in detail below, suggest that 1P stimulation and imaging may be preferable over the 2P approaches which have been optimized for *in vivo* use. To achieve 1P AON in brain slice one must (a) identify an actuator/reporter pair with good photostability and minimal optical crosstalk under 1P illumination, and (b) implement a 1P optically sectioned wide-area imaging scheme. Here we combine molecular and optical engineering to address these challenges.

Red-shifted channelrhodopsins have been combined with a GCaMP Ca^{2+} indicator for 2P AON *in vivo*[107–109], but 1P GCaMP excitation causes spurious channelrhodopsin excitation. Lower optical crosstalk is achieved by pairing a blue-shifted channelrhodopsin with a red-shifted reporter[82]. Red genetically encoded Ca^{2+} indicators (RGECIs) now offer good sensitivity, but their combination with optogenetic stimulation has been hampered by blue-light induced photoswitching of the mApple-based chromophores used in the most sensitive RGECIs[69,129,70].

Furthermore, blue channelrhodopsins such as ChR2(H134R) retained some excitation at the yellow (561 nm) wavelengths used to excite RGECIs, introducing crosstalk of the imaging light into the stimulation channel. A truly orthogonal 1P actuator/RGECI reporter pair has not previously been reported.

TsChR, derived from Tetraselmis striata[130], is the most blue-shifted channelrhodopsin reported to-date, but its initial characterization yielded a poor photocurrent. To our knowledge, TsChR has not previously been used in any optogenetic experiments. Here we show that a version with improved trafficking, éTsChR, drives robust spiking in cultured neurons and in tissue. Combination of éTsChR with a nuclear-localized red-shifted Ca^{2+} reporter, H2B-jRGECO1a, achieved 1-photon AON in cultured neurons and in slice. The blue light used to activate the éTsChR was dim enough to avoid jRGECO1a photoswitching, and the yellow light used to excite jRGECO1a did not spuriously activate the éTsChR.

On the imaging front, 1P structured illumination microscopy (SIM) techniques can achieve optical sectioning in tissue[58]. We developed a generalized SIM technique based on Hadamard-Walsh encoding and implemented it in a mesoscope imaging system. Hadamard microscopy provides better rejection of out-of-plane fluorescence than do other SIM techniques and offers the ability to make systematic tradeoffs between background rejection and time resolution.

By applying 1P optogenetic stimulation and Hadamard microscopy to acute slices expressing éTsChR and H2B-jRGECO1a, we obtained simultaneous functional characterization of > 6,000 neurons, spread over a region 2.3 x 2.3 mm with 5.6 Hz time resolution. Maps of optically induced activity highlighted distinct cortical layers, which otherwise appeared homogeneous in their flu-

orescence. We used the AON system to map with cellular resolution the effects of anti-epileptic drugs on neural excitability, and to study cortico-cortico and cortico-striatal functional connectivity. Finally, we show that with an improvement to the algorithm based on compressed sensing, the imaging speed can be increased to 33 Hz as described in **Chapter 3**. The combined molecular and optical tools provide a powerful system for wide-area investigations of neural function in brain tissue.

2.2 Materials and methods

2.2.1 DNA constructs

R-CaMP2 was a gift from Haruhiko Bito. TsChR was a gift from Ed Boyden. jRGECO1a and jRCAMP1a were obtained from Addgene (Plasmids #61563 and #61562). All RGECIs were cloned between the BamHI and EcoRI sites of the backbone from FCK-Arch-GFP (Addgene Plasmid #22217) for expression in cultured neurons and for lentiviral production. For photophysical characterization, RGECIs were also cloned into an analog of the FCK vector replacing the CaMKIIα promoter with a CAG promoter, a configuration we refer to as FCAG. The jR-CaMP1a and jRGECO1a constructs included the nuclear export sequences found in the original publication[70]. For nuclear localization, the nuclear export sequence of jRGECO1a was replaced with an H2B tag, and cloned into an AAV-hSyn-DO Cre-off vector. TsChR, including an N-terminal Kir2.1 trafficking sequence followed by a GFP fluorescent tag, was cloned into FCK and into an AAV expression vector under control of the human synapsin promoter (AAV-hSyn).

CheRiff-TS-GFP (Addgene Plasmid # 51693) was cloned into an AAV-CAG-DIO expression vector. FCK-ChR2(H134R)-GFP was used as a reference for eTsChR characterization. FCK-VSV-G (Addgene Plasmid #8454) and psPAX2 (Addgene Plasmid #12260) were used in lentiviral production. pUC19 (NEB #N3041) was used as a diluent in calcium phosphate transfections.

2.2.2 Cell culture and gene expression

2.2.2.1 HEK cell culture and gene expression

Photophysical measurements of RGECIs were performed in HEK293T cells (ATCC CRL-11268) cultured as previously described[82]. Cells were grown at 37 ˚C, 5% CO_2 in DMEM containing 10% FBS (Life Technologies 10082-147) and 50 U/mL penicillin-streptomycin (Life Technologies 15060-063). Cells were split with trypsin-EDTA (Life Technologies 25300054) every 2-3 days and used before passage 25. For gene delivery, cells were grown to 70% confluence in 24 well plates or 35 mm plastic dishes. 200 ng (for 24 well plates) or 400 ng (for 35 mm plastic dishes) of FCAG-RGECI DNA was transfected using TransIT-293 (Mirus 2705) following manufacturer instructions. After 24 hours, cells were split onto Matrigel (Fisher Scientific 356234) coated glass bottom plates (In Vitro Scientific D35-14-1.5-N) and imaged 24 hours later.

2.2.2.2 Low titer lentivirus production

HEK293T cells were cultured as in the previous section, except that cells were split daily and the cell density was always maintained between 30 and 70%. Prior to P11, cells were split onto gelatin

coated plates, prepared by incubating 15 cm plastic dishes (Nunc) for 20 minutes at room temperature with 10 mL EmbryoMax 0.1% Gelatin solution (Millipore FS-006-B) and aspirating to dryness. 10 cm dishes were also used, and all amounts were scaled to the smaller surface area. After cells reached 80% confluency, cells were switched to 16 mL pre-warmed DMEM without FBS for 1-2 hours. For each dish, the following were added, in order, to 1.2 mL DMEM: 14 μg of FCK-RGECI plasmid, 9 μg psPAX2, and 4 μg VsVg were combined with 36 μL of 1 mg/mL PEI in water (Aldrich #408727). The tube was vortexed and incubated at room temperature for 10 minutes. The mixture was then pipetted dropwise over the surface area of the dish and the cells were returned to the incubator for 4 hours. After the incubation, the medium was replaced with 16 mL DMEM + 10% FBS without antibiotics. 36-48 hours later, the medium was collected and centrifuged for 5 min at 500 × g. The supernatant was filtered through a 0.45 μm filter blocked with DMEM + 10% FBS and aliquoted in 1-5 mL fractions. Aliquots were kept at -80˚C until use.

2.2.2.3 Primary neuron culture and gene expression

Cultured rat hippocampal neurons on astrocyte monolayers were prepared as previously described[82], with two modifications: (1) In Vitro Scientific dishes model D35-14-1.5-N were used instead of D35-20-1.5-N, while keeping the cell densities the same, and (2) neurons were cultured in Neurobasal-A (Life Technologies 10888-022) supplemented with B27 (Life Technologies 17504044) instead of Brainbits' NbActiv4. For electrophysiological and AON measurements, neurons were transfected via calcium phosphate, as previously described[82] on DIV7 and used on

DIV14-16. For comparison of RGECI performance by field stimulation (**Figure 2.1b,c**), cultured neurons were lentivirally transduced. On DIV 7, half of the media from each dish (1 mL) was reserved and replaced with 250 μL of low titer FCK-RGECI lentivirus. After two days, all of the media was removed and replaced with the reserved media supplemented with an additional 1 mL of Neurobasal-A + B27 supplement.

2.2.3 Imaging and electrophysiology in culture

2.2.3.1 Microscope

A custom-built epifluorescence microscope was used for measurements in HEK293T cells and in cultured neurons. Illumination was provided by a 561 nm 100 mW laser (Cobolt Jive 0561-04-01-0100-500) or a 488 nm 100 mW laser (Coherent Obis 1226419). The laser lines were combined and focused in the back focal plane of the objective (Olympus Fluor 4x 0.24 *NA* for single action potential measurements of RGECIs; Olympus LCPlanFL 20x 0.40 *NA* for RGECI photobleaching measurements; Olympus UPlanSApo 10x 0.40 *NA* for RGECI photoswitching characterization; Olympus ApoN 60x 1.49 *NA* Oil for éTsChR characterization). Fast modulation of the 488 nm laser was achieved with an acousto-optic tunable filter (Gooch&Housego TF525-250-6-4-GH18A). Both laser lines were additionally modulated by neutral density filters as necessary. Fluorescence light was separated from illumination light using a quadband dichroic (Semrock Di01-R405/488/561/635). HQ550/50m or ET595/50 bandpass emission filters (Chroma) were used to isolate GFP or RGECI fluorescence, respectively, before capturing on a scientific CMOS camera

(Hamamatsu Orca Flash 4.0). For photobleaching measurements, an additional 1 OD filter was inserted in the imaging path to avoid saturating the camera. Illumination profiles were acquired on bead samples before experiments each day and spot size was determined using a 1/e2 cutoff. Laser powers were measured at the sample plane. A digital acquisition (DAQ) card (National Instruments PCIe 6259) was used to synchronize command and recording waveforms. Imaging frame rates and illumination powers are indicated in figure captions for each experiment.

2.2.3.2 Imaging and electrical recordings

In all imaging measurements, culture medium was replaced with imaging buffer containing, in mM, 125 NaCl, 2.5 KCl, 2.5 HEPES, 30 glucose, 1 MgCl2, 3 CaCl2. The buffer pH was adjusted to 7.3 and osmolarity was 310 mOsm. Measurements were carried out at room temperature. 10 μm CNQX, 20 μm gabazine, and 25 μm APV (all Tocris) were included in cultured neuron experiments to block synaptic transmission. Channelrhodopsin characterization measurements were performed in synaptic blockers with the addition of 1 μm tetrodotoxin (Tocris). No additional all-trans retinal was added.

Field stimulation (**Figure 2.1b,c**) was performed by inserting two chlorided silver wire loops 2 cm apart into the glass-bottomed imaging dish, touching the plastic on either side of the coverslip. A high voltage amplifier (Krohn-hite 7600M) was used to amplify 1 ms pulses generated by the DAQ card to 60-120 V. 3-4 FOVs were acquired for each construct, using a fresh dish each time.

For patch clamp electrophysiology measurements (**Figure 2.1e-g**, **Figure 2.9d**), 3-5 MΩ borosilicate glass pipettes (WPI) were filled with internal solution containing, in mM, 125 potas-

sium gluconate, 8 NaCl, 0.6 MgCl2, 0.1 CaCl2, 1 EGTA, 10 HEPES, 4 Mg-ATP, 0.4 Na-GTP, adjusted to pH 7.5 and 295 mOsm with sucrose. Voltage- and current-clamp recordings were obtained with a Multiclamp 700B amplifier (Molecular Devices) while illuminating with 1 s 488 nm pulses or 2s 561 nm pulses of intensities indicated in figure captions. In voltage clamp measurements, cells were held at -65 mV. In current-clamp measurements, an offset current was injected to maintain the resting membrane potential at -65 mV. Signals were filtered at 5 kHz with the amplifier's internal Bessel filter and digitized at 10 kHz.

2.2.3.3 Data analysis

All values are expressed as mean ± standard error of the mean (s.e.m.). P values were obtained from Student's t-tests unless otherwise indicated.

Whole FOV RGECI single action potential responses (**Figure 2.1b,c**, **Table 2.1**) were extracted as previously described[131]. Activation time constants were extracted from monoexponential fits between stimulation onset and maximum ΔF/F. For inactivation time constants, the fluorescence trace after the maximum ΔF/F was fit to a sum of two exponential decays, and the τ_{off} was taken as the time for the fit to decay to half its maximum value. Photobleaching traces (**Table 2.1**) were extracted from separate cells and fit to a monoexponential to obtain time constant τ_{bleach}.

Movies of blue light photoswitching (**Figure 2.2d,e**) were preprocessed to reject saturated pixels and a threshold equal to half the average of movie was used to separate foreground from background. Background intensity was subtracted from the original movies and the averages of

the resulting foreground traces (combining 10-20 cells each) were used in downstream analysis. Traces were converted to ΔF/F using the fluorescence value before blue light stimulation as F0. "Photoswitching ΔF/F" was defined as the ΔF/F immediately after blue light illumination ends (**Figure 2.2d**, inset).

For comparison of channelrhodopsins (**Figure 2.1e-g**, **Figure 2.9d**), cells were rejected if they required >100 pA holding current to maintain -65 mV in current clamp or if their baselines drifted by more than the smallest steady state photocurrent amplitude in voltage clamp mode. Steady-state 488 nm photocurrents were extracted as the average photocurrent over the last 100 ms of blue light illumination. Steady state 561 nm photocurrents and depolarizations were extracted from 1 s of data. On time constants were obtained from single exponential fits to the first 1.5 ms of 488 nm illumination. Off time constants were obtained from single exponential fits to the 99.5 ms following blue light 488 illumination.

Recordings of jRGECO1a fluorescence in **Figure 2.1h** were corrected for photobleaching with a bi-exponential fit to the initial period in each movie, before stimulation, while recordings of BeRST1 fluorescence were corrected for photobleaching by a sliding, 1000 point, median filter. Both traces were converted to ΔF/F based on the fluorescence before blue light stimulation. Frames acquired during blue light stimulation were dropped to avoid optical crosstalk.

2.2.4 Hadamard imaging

2.2.4.1 Microscope

In the ultra-widefield microscope (**Figure 2.3a**), a 561 nm laser beam (MPB Communications F-04306-02) was transmitted through a rotating diffuser, and merged with a 470 nm LED beam (Thorlabs M470L3). Both were expanded, focused, and coupled through free space to fill with high *NA* illumination a digital micromirror device (DMD) module (Vialux V-7001; 1024x768 pixels, 13.7 μm pitch). Multiple diffraction orders emitted from the DMD pattern were transmitted by a 100 mm projection tube lens (Zeiss Makro-Planar 100 mm, L1 in **Figure 2.3a**), reflected off a custom dichroic mirror (Semrock Di01-R405/488/561/635-t3-60x85), and imaged onto the sample by a 50 mm objective lens (Olympus MVPLAPO 2XC, *NA* 0.5, L2 in **Figure 2.3a**). The 3 mm substrate thickness of the dichroic mirror minimized warping-induced projection aberrations. Fluorescence emission was collected through the same objective and dichroic, a large diameter (60mm) emission filter (Semrock FF01-520/35-60-D or Chroma ET600/50m, F in **Figure 2.3a**), and a 135 mm imaging tube lens (Zeiss Apo-Sonnar 135 mm, L3 in **Figure 2.3a**) onto a scientific CMOS camera (Hamamatsu Orca Flash 4.0, 2048x2048 pixels). The FOV was 4.6x4.6 mm2 in the sample plane, corresponding to a magnification of 2.89x onto the camera, and 2.17x onto the DMD. Camera and DMD pixels were 2.25 μm and 6.3 μm wide in the sample, respectively. Hardware and triggers were programmed in LabView, with pattern generation and data analysis performed in MATLAB.

2.2.4.2 Illumination patterns

To reject light scattered within the sample, pattern sequences were designed such that in the projected series of 2D images, neighboring locations of the sample were illuminated with orthogonal functions of intensity vs. time. A Hadamard matrix, H, of size m is a binary square matrix with elements $\{-1, 1\}$ that fulfills $H^T H = mI_m$, where I_m is the identity matrix of size m; its normalized form has value 1 in the first column and first row. Illumination intensities could not be negative, so the projected intensity patterns were defined as $P = (H' + 1)/2$ where $H' = H[1, \ldots, m; m - n + 1, \ldots, m]$ was an incomplete orthogonal basis given by the last n columns of a normalized Hadamard matrix, with $n < m$.

The illumination patterns P thus had binary values $\{0, 1\}$ corresponding to DMD mirror positions OFF and ON respectively. Each location was illuminated with a positive temporal function orthogonal to all other designed Hadamard codes, as verified by $P^T H' = I_n m/2$. For a given number of locations, a Hadamard matrix provided a set of shortest possible binary orthogonal functions. To arrange the n codes in P into illumination patterns, $m = n + 1$ images were defined assigning code $k_{i,j} \in \{1 \ldots n\}$ to DMD pixel (i, j), as $k_{i,j} = \mathrm{mod}(iq + j, n) + 1$, where q was an offset parameter that maximized spatial separation of repeated codes. (n, q) was set to $(11, 3)$ for functional imaging, and to $(63, 14)$ or $(59, 8)$ for structural imaging. To further reduce spurious scattering cross-talk, a random binary mask R was generated to flip the sign of 50% of DMD pixels, applied as an exclusive OR operation on all DMD patterns against the same mask R. In the compressed sensing experiment (**Figure 2.10**) the sequence of Hadamard patterns was

interleaved with its complement (interchanging bright and dark pixels).

2.2.4.3 Calibration

To prepare the system for each imaging session, a calibration data-set C was obtained by placing a thin fluorescent sample at the focal plane, and acquiring an image with each illumination pattern. The sample consisted of green or orange neon Sharpie (Newell Brands, NJ) ink painted on (or sandwiched between) glass coverslips, to match imaging conditions of subsequent acute (fixed) tissue experiments. For each camera pixel, the time series of its photon counts was cross-correlated against each Hadamard sequence as $C^T H'$. The resulting cross-correlation images displayed sharp peaks indicating the projected DMD locations for each code, with positive or negative correlation given by R. A synthetic approximation to the cross-correlation maps was calculated by finding the code with maximum absolute correlation for each pixel, yielding homogeneous, noise-free cross-correlation maps.

2.2.4.4 Reconstruction

A Hadamard sequence data-set D was acquired after replacing the calibration sample with a tissue sample. Photon counts at each camera pixel were cross-correlated against each Hadamard sequence as $D^T H'$. Cross-correlation images displayed a set of peaks modulated by the local fluorophore density, and broadened by off-focus fluorescence and light scattering in the sample. Each peak characterized the scattering function of the corresponding tissue location, i.e. its absolute value represents the image one would record with an illumination spot focused solely at that

location in the tissue. The next step was to apply a set of computational 'pinholes' to select the unscattered in-focus photons, and to reject all others. The spatial filter was implemented through the element-wise product of calibration correlation maps and tissue correlation maps, resulting in the positive filtered maps $F = C^T H' \odot D^T H'$, where $\odot$ denotes element-wise multiplication. This computational process was akin to sifting emitted light through an array of pinholes as happens physically in spinning disk confocal microscopy. The final computation step was to aggregate the unscattered light by direct sum of the filtered images over all code maps, defining an optical section image $\phi_i = \sum_{k=1}^{n} F_{i,k}$.

All static Hadamard image computations in this work were accelerated by computing $\phi_i = \sum_{k=1}^{m} G_{i,k}$, with $G = C^T \odot D^T$. This approach is numerically equivalent to the more involved process described above, as proved by:

$$
\begin{aligned}
\phi_i &= \sum_{k=1}^{n} F_{i,k} \\
&= \sum_{k=1}^{n} \sum_{p=1}^{m} C_{i,p}\, H_{k,p} \sum_{q=1}^{m} D_{i,q}\, H_{k,q} \\
&= \sum_{p=1}^{m} \sum_{q=1}^{m} C_{i,p}\, D_{i,q} \sum_{k=1}^{n} H_{k,p}\, H_{k,q} \\
&= \sum_{p=1}^{m} \sum_{q=1}^{m} C_{i,p}\, D_{i,q}\, \delta_{p,q} \\
&= \sum_{q=1}^{m} C_{i,q}\, D_{i,q} \\
&= \sum_{k=1}^{m} G_{i,k}\ ,
\end{aligned}
$$

where $\delta_{p,q}$ is a Kronecker delta. The resulting optical section preserved unscattered light emitted from the focal plane, while rejecting scattered light and background emissions. Standard wide-

field epifluorescence images were also computed from each Hadamard dataset by computing a direct sum of all frames in the raw images, $W_i = \sum_{k=1}^{m} D_{i,k}$.

To correct for slight motion artifacts due to sample drift, all datasets from one brain slice were registered to a reference image using a b-splines transform maximizing mutual information[132].

2.2.4.5 Compressed Hadamard Imaging

While this manuscript was in review, we developed a compressed sensing measurement method to increase the time resolution from m camera frames (where m is the length of the Hadamard sequence) to 2 camera frames per optical section. This approach and its trade-offs are characterized in **Chapter 3**. For application of compressed Hadamard imaging to AON (**Figure 2.10**), procedures, optogenetic methods, and imaging protocol were as in other experiments, except an Olympus XLPLN10XSVMP ($NA = 0.6$) objective was used to map DMD and camera pixel size to 2.52 and 0.9 μm at the sample respectively. Illumination comprised 24 patterns, interleaved with their complements, repeated in 36 cycles. Camera and DMD frames were updated at 66 Hz. Reconstruction was performed in 64x64 pixel blocks with 40 principal components per block.

2.2.4.6 Hadamard image formation

To understand the optical sectioning process, Hadamard microscopy was modeled as an incoherent illumination, intensity-linear space-invariant optical system, in which the intensity after propagation is given by a convolution between intensity before propagation and an intensity impulse response function. In a discrete representation, the circulant convolution matrix S_1^T

represented three-dimensional excitation intensity at the object, in response to an impulse function reflectance at the DMD plane (turning on one DMD pixel). Similarly, S_2 was defined as the intensity collected by an impulse detector at the camera plane from emitted fluorescence in a three-dimensional object (analogous to detection from one camera pixel). The data collected from tissue with fluorophore distribution G upon illumination with a structured illumination pattern P was represented as $D = S_2 \,\mathrm{diag}(G) S_1^T P$, where diag denoted rearrangement between vector and diagonal matrix. Calibration with a thin uniform fluorescent object and no scattering was represented as $C = P$. After assuming that P contains an orthonormal Hadamard code with no spatial repetition, it followed that $C^T H' = I_n$, and $D^T H' = S_2 \,\mathrm{diag}(G)\, S_1^T I_n$. Then $\phi = \sum_k C^T H' \odot D^T H' = \mathrm{diag}(S_2 \,\mathrm{diag}(G)\, S_1^T)$, or $\phi = (S_1 \odot S_2)\, G$. The reconstructed optical section ϕ was proportional to the object G convolved with the confocal scattering function $S = S_1 \odot S_2$ that resulted from the element-wise product of the projection and collection scattering functions. This analysis is extended to the continuous domain in **Appendix A**.

To simulate the effects of lateral sub-pixel offset between the DMD pixels and the smaller camera pixels, we used a continuous space version of the model described above, defining the diffraction-limited excitation and emission PSFs as Gaussian functions and convolving these PSFs by square apertures representing the DMD and camera pixels, respectively. The system PSF was calculated from the product of the excitation and emission PSFs.

2.2.4.7 Image processing and filtering

The lines between DMD pixels led to a periodic grid artifact in Hadamard optical sections. A Gaussian stopband filter was used to attenuate these artifacts. The filter parameters were not changed after initial set-up.

The size of the computational pinholes could be adjusted in software to trade optical signal level for z-resolution. Tuning of pinhole sizes was achieved by applying a spatial Gaussian filter to the calibration patterns, with $\sigma = 5.6$ μm for functional images, and $\sigma = 3.4$ μm for structural images. Further increases in σ to sizes larger than the spacing of pinholes resulted in a continuous transition to wide-field epifluorescence imaging.

An additional source of systematic error came from local inhomogeneity of illumination patterns. While the projected patterns have 50% duty cycle on average, variations in local illumination can change the relative contributions of in-plane signal and background, resulting in imperfect background cancellation manifested as regions with periodic background artifacts. This effect was minimized for Hadamard images in **Figure 2.5b,c** by dividing raw tissue data by its low spatial frequency component, calculated with a Gaussian filter with $\sigma = 22.5$ μm.

Images in all figures were linearly mapped to grayscale setting 0 to black and saturating to white the 0.01 percentile of highest intensity values unless otherwise indicated.

2.2.4.8 Characterization

We quantified the performance of Hadamard, stripe SIM, and HiLo optical sectioning methods by three measurements. First, we measured the point spread functions by imaging 200 nm fluorescent beads (Invitrogen F8763) embedded in 1.5% agarose gel. Second, we tested the in-plane uniformity of optical sections by measuring a thin fluorescent plane of orange neon Sharpie (Newell Brands, NJ) ink painted on a glass coverslip. Third, we acquired multi-plane images of an acute brain slice expressing H2B-jRGECO1a to evaluate the imaging quality of each method in turbid tissue.

For the beads and plane experiments, illumination patterns for Hadamard codes of length 12, together with striped illumination with period 4 pixels and 4 phases, were interleaved and repeat-averaged to match total photons and photobleaching conditions across datasets. HiLo optical sections were computed from the same patterns used for Hadamard imaging, using a photon-matched uniform illumination image and a repeat-averaged structured image corresponding to one Hadamard pattern. HiLo uses only a single random illumination pattern, and thus necessarily uses a non-uniform total photon count across the sample. We used more total photons in HiLo optical sections to avoid penalizing this method in the comparison. A series of images taken at $\Delta z = 2.24$ μm were acquired to map the three dimensional PSF.

Hadamard images were calculated as $\phi_i = \sum_{k=1}^{m} G_{i,k}$, with $G = C^T \odot D^T$. Stripe SIM optical sections were calculated as $\phi = |\sum_{k=0}^{m-1} I_k \exp(-i2\pi k/m)|$, with $m = 4$. HiLo optical sections were calculated setting the wavelet filter $\sigma = 0.75$. DMD modulation grid artifacts

were present in all datasets and were not corrected. Widefield reference images were obtained by summing all patterns in the Hadamard sequence.

Images of the homogeneous fluorescent plane were acquired following the same protocol as for the beads. The same flat field correction was applied to all datasets by subtracting the offset and dividing by the blurred intensity distribution of a focused widefield image. All datasets were filtered equally to reduce DMD grid artifacts. Within a region of interest, the standard deviation of values was normalized by their mean to obtain coefficients of variation.

To estimate the degree of cell-to-cell fluorescence crosstalk in nuclear-labeled acute brain slices, we first computed a mean Hadamard 'nucleus spread function', i.e. the mean fluorescence distribution measured from multi-plane structural Hadamard images of fluorescent nuclei in acute brain slices. We then used high-resolution confocal microscopy to estimate the center locations of all neuronal nuclei in a fixed brain slice up to a depth of 100 μm. We computationally positioned the nucleus spread functions at the nuclear locations, adjusted signal levels to account for the measured attenuation with depth, and estimated the crosstalk, i.e. the amount of signal ascribed to each nucleus that originated from other nuclei.

2.2.5 Software accessibility

The Hadamard control and analysis software and an example data-set are available at

https://github.com/adamcohenlab/Hadamard-Code

The compressed Hadamard analysis software is available at

https://github.com/adamcohenlab/Compressed-Hadamard-Code

2.2.6 Animals and acute slice measurements

2.2.6.1 Animals

All procedures involving animals were in accordance with the National Institutes of Health Guide for the care and use of laboratory animals and were approved by the Institutional Animal Care and Use Committee (IACUC) at Harvard University. Excitability measurements and characterization of functional Hadamard imaging were performed in wild type C57Bl6 (Charles River Labs #027) mice. Functional connectivity assays were performed in Rbp4-Cre$^{+/-}$ mice donated by Bernardo Sabatini's lab and originally generated in the GenSat project (#KL100). For structural imaging of membrane bound mCitrine, FLOXed Optopatch-3 mice (Jackson Labs #029679) were crossed with Rbp4-Cre$^{+/-}$ mice or with CaMK2a-Cre$^{+/-}$ mice (Jackson Labs, #005359).

2.2.6.2 AAV injection

AAV2/9-hSyn-DO-H2B-jRGECO1a (1.60×10^{13} GC/mL) and AAV2/9-hSyn-eTsChR (2.22×10^{13} GC/mL) were produced at Massachusetts Eye and Ear Infirmary Vector Core. AAV2/9-CAG-DIO-CheRiff-TS-GFP (5.80×10^{13} GC/mL) was produced by the Stanford Vector Core. AAV1-hSyn-NES-jRGECO1a (2.44×10^{13} GC/mL) was purchased from the University of Pennsylvania Vector Core. When two viruses were coinjected, they were mixed in a one-to-one volume ratio. The final mixture was mixed in a 7:1 ratio with 0.4% Trypan Blue to aid in visualization during injection. For viral injections, neonatal (P0-2) animals were cold-anesthetized and taped to an aluminum heatsink submerged in an ice bath, with their heads resting on a modeling clay sup-

port. A stereotaxic injector (WPI #UMC4) mounted on a stereotaxic frame (Stoelting) was used to inject virus 1.6 mm anterior and 1.6 mm lateral to lambda every 0.4 mm starting from 3 mm beneath the surface of the skull. 40 nL of virus was delivered at each depth at a rate of 5 nL/s. If only one virus was used, only 20 nL were injected per depth. Expression levels were sufficiently high for Hadamard imaging from 12 days until at least 9 weeks after injection.

2.2.6.3 Preparation of fixed slices

Fresh 300 μm brain sections were incubated in 4% paraformaldehyde overnight at 4 $^{\circ}$C, then mounted on a glass slide in Fluoromount and stored at 4 $^{\circ}$C.

2.2.6.4 Acute slice preparation and imaging

Acute slices were prepared from P21-28 animals. Animals were deeply anesthetized via isoflurane inhalation and transcardially perfused with ice-cold choline cutting solution, containing, in mM, 110 choline chloride, 25 $NaHCO_3$, 2.5 KCl, 7 $MgCl_2$, 0.5 $CaCl_2$, 1.25 NaH_2PO_4, 25 glucose, 11.6 ascorbic acid, and 3.1 pyruvic acid (310 mOsm/kg). The brain was blocked with one coronal cut just anterior to the tectum and mounted with Krazy glue on the specimen disk of a Leica VT1200s vibratome. After mounting, hemispheres were separated with a sagittal cut down the midline of the brain. The brain was covered with more ice-cold choline solution and then sliced in 300 μm steps. Slices containing the striatum were recovered for 45 minutes in a 34 $^{\circ}$C artificial-cerebrospinal fluid (ACSF) bath containing, in mM, 125 NaCl, 2.5 KCl, 25 $NaHCO_3$, 2 $CaCl_2$, 1 $MgCl_2$, 1.25 NaH_2PO_4, 25 glucose (295 mOsm/kg). Slices were kept in room temperature ACSF

until ready to measure and were used within 8 hours. All solutions were bubbled with carbogen (95% O_2, 5% CO_2) for the duration of the preparation and subsequent experiment.

For imaging, slices were mounted on Poly-L-Lysine (PLL) coated coverslips. Coverslips (Fisher #12-545-80) were plasma cleaned for 3 minutes, covered with 50-100 μL 0.1% (w/v) PLL (150-300 kD) solution (Sigma #P8920) and allowed to dry under vacuum. Coverslips were thoroughly washed with nanopore water and dried before use. To mount the tissue, a slice was transferred to the PLL-coated face of the coverslip with a Pasteur pipette. Excess ACSF was pipetted or wicked away with filter paper, in the process flattening out the brain slice and adhering it to the glass. We found that this method worked reliably for coronal slices from one hemisphere but not for coronal slices from the entire brain. Coverslips were placed in a custom-built flow chamber with a microscope slide bottom and #1.5 coverslip lid. ACSF was perfused at a rate of 1 mL/min with a VWR peristaltic pump.

The imaging protocol consisted of a 2 s imaging epoch followed by a 400 ms stimulation period and another 2 s imaging epoch. Each imaging epoch comprised 11 frames of functional Hadamard acquired with a 180 ms period under 100 mW/cm^2 561 nm illumination. Blue light stimulation protocols are described in figure captions. The slice was allowed 6 s to recover before starting another imaging epoch. One run consisted of 6 imaging and stimulation rounds over one minute. Runs were repeated several times, spaced out by at least five minutes. NBQX and CPP, or TTX (Tocris) or retigabine, phenytoin, or carbamazepine (Sigma) were added to the ACSF from 1000x stock solutions after several baseline runs. In figure 4, brain slices were randomly selected from a pooled set of slices for different drug treatments.

2.2.7 Analysis of slice data

2.2.7.1 Registration

After reconstruction of Hadamard images as detailed in **Section 2.2.4.4**, frames for each epoch were averaged together. Small movements and deformations in the slice over the course of multiple runs were corrected by automatic non-rigid registration[132]. Functional Hadamard recording and structural Hadamard images were manually registered using a 2D affine transformation.

2.2.7.2 Cell selection

ΔF images were calculated for each registered run by subtracting images acquired before blue light stimulation from images acquired immediately after blue light stimulation. Peaks in ΔF images corresponded to individual cells, but noise in ΔF varied as a result of brightness inhomogeneities in the slice, making it difficult to extract peaks directly. To correct for this noise, a widefield image for each slice was blurred with a 2D Gaussian with an 8 pixel (19.2 μm) standard deviation, to remove nucleus sized objects. The square root of this image was used to normalize the ΔF image of the slice. High spatial frequency noise was removed with a 2d Gaussian filter with a 0.5 pixel (1.2 μm) standard deviation. Regions without expression were manually selected and standard deviations in these regions were chosen as a noise floor. Cells were identified as peaks in the normalized ΔF image which had an amplitude larger than the noise floor by a user-defined factor, typically 7 – 10. Cells were required to have a minimum distance in space of 4 pixels (9.6 μm) to avoid double counting cells. Once cell locations were identified, single-cell fluorescence traces were ex-

tracted from corresponding locations in movies of unnormalized data blurred with 2d Gaussian filter with 1 pixel standard deviation.

2.2.7.3 Exclusion of spontaneously active and dying cells

While measuring a large number of cells in an acute slice, a portion of cells showed spontaneous activity, characterized by transient fluorescent increases uncorrelated with blue light stimulation; and cell death, characterized by a large and irreversible increase in fluorescence. For Figs. 6-9, slices were imaged nine times, five times before AED application and four times after. Imaging epochs were averaged to generate movies with 108 frames (12 epochs per run x 9 runs). After extracting cell traces from these movies for all slices in the experiment, each cell's mean and standard deviation per run were calculated. Least squares fits on the mean and standard deviation were performed on 3-pre drug runs and projected to the full nine runs. Cells were excluded from further analysis if any projected mean or standard deviation was less than 1/15 of the cell's mean value or if the root mean square error of the fit was larger than 1/15 of the cell's mean value. This procedure rejected $< 17\%$ of cells.

2.2.7.4 Generation of excitability maps

To generate the maps in **Figure 2.7** the fluorescence trace for each included cell was normalized by subtracting its mean fluorescence values for each run and normalizing by the standard deviation for each run. For each cell, 3 pre-drug runs were averaged together to yield a 12 element vector corresponding to normalized F in each epoch. Principal component analysis yielded 3 main prin-

cipal components which were then back-projected into pixel space for each slice, yielding the black and white images in **Figure 2.7c**. Color images (**Figure 2.7d,e**) were generated using L*a*b colorspace, by projecting PC1 into lightness, L, and PC2 and PC3 into the red-green and blue-yellow axes, a and b.

To generate maps of changes in drug response in **Figure 2.8a**, ΔF images from four runs before and after drug addition were averaged together, median filtered with a 3 pixel kernel, saturated at their 99.5th percentile, and displayed in the green and red channels, respectively. The blue channel is the average of the red and green images. Color saturation was adjusted in L*a*b space to aid in visualization. In **Figure 2.9** ΔF images are scaled to the same absolute counts and shown in separate color channels.

2.2.7.5 Cortical layer analysis

All striatal cells were pooled and treated separately. For cortical cells, cortex boundaries were manually defined in structural images as the surface of the brain and the bottom of Layer 6. Boundaries were registered to functional images (above) and cells were assigned a normalized depth coordinate based on these boundaries. Drug response, defined as ΔFdrug/ΔF0, could then be related to normalized cortical depth. For each slice, cells were binned by cortical depth and the drug response per cell averaged over cells. Extreme cell responses were excluded from each bin using the generalized extreme Studentized deviate test. Layer boundary locations were taken from the primary somatosensory cortex in the matched coronal slices of the Allen Brain Reference Atlas. KCNQ3 expression levels were acquired from Allen Brain Institute experiment #100041071. The

somatosensory cortex was manually defined in 11 sagittal slices from a P28 male mouse. The available expression image was used to mask the raw data, but expression values were obtained directly from the raw ISH data. The edges of the cortex and cortical depth bins were defined as above and expression values were averaged together across slices from the same experiment.

2.3 Results

2.3.1 A spectrally orthogonal Calcium sensor and channelrhodopsin for one-photon AON

AON requires a spectrally orthogonal optogenetic actuator and activity reporter (**Figure 2.1a**). Examination of channelrhodopsin action spectra and Ca^{2+} reporter excitation spectra suggested that the best approach for 1-photon AON was to use a blue-shifted channelrhodopsin and a red-shifted genetically encoded Ca^{2+} indicator (RGECI) (**Figure 2.1a**). We thus set out to identify protein pairs suitable for this purpose.

We began by comparing the single action potential responses of RGECIs in cultured neurons. jRGECO1a was the most sensitive ($\Delta F/F = 54 \pm 10\%$, n = ~120 neurons. Unless otherwise indicated, all uncertainties are standard errors of the mean), followed by R-CaMP2 and jRCaMP1a, consistent with previous reports (**Figure 2.1b**, **Table 2.1**)[129]. R-CaMP2 had the fastest kinetics (τ_{on} = 26 ± 10 ms, τ_{off} = 270 ± 20 ms, n = ~120 neurons), followed by jRGECO1a (τ_{on} = 47 ± 1 ms, τ_{off} = 440 ± 40 ms, n = ~120 neurons) and jRCAMP1a (**Figure 2.1c**, **Table 2.1**). In HEK293T cells, under basal Ca^{2+} conditions, jRGECO1a had the longest photobleaching time

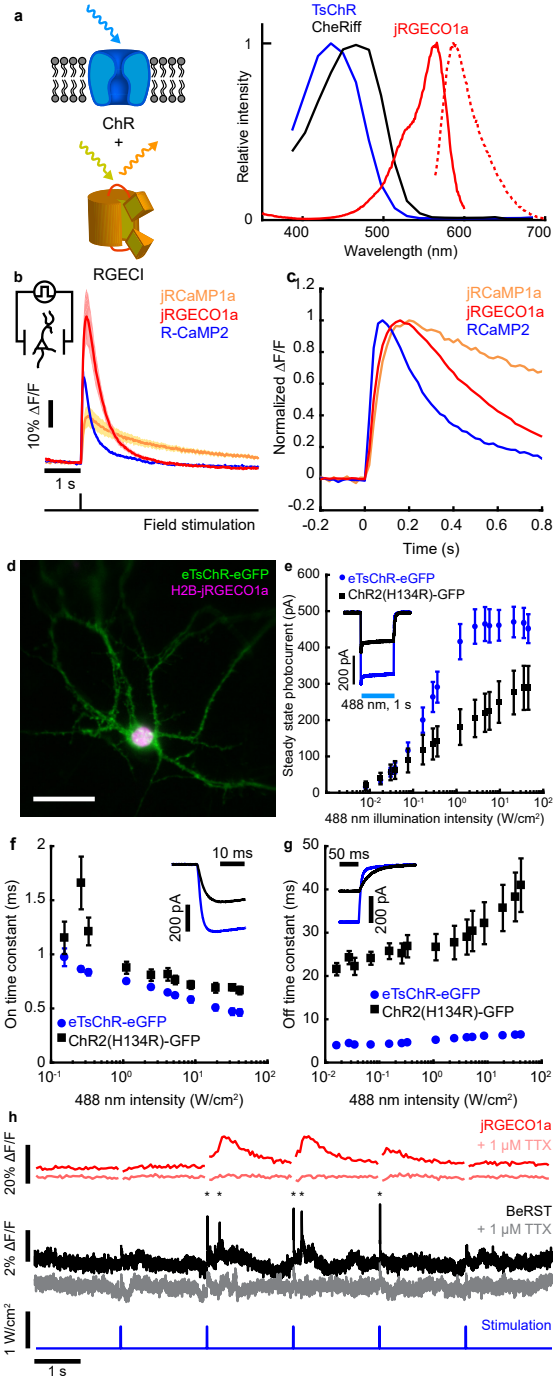

Figure 2.1: All-optical neurophysiology with a blue-shifted channelrhodopsin and a red-shifted Ca^{2+} indicator. **a)** Left: Schematic of a spectrally orthogonal channelrhodopsin and RGECI. Right: action spectra of proteins used in this work. Spectra are reproduced with permission for jRGECO1a [70], TsChR [130], and CheRiff [82]. **b)** Single action potential responses of RGECIs in cultured rat hippocampal neurons. Dark lines indicate the average of 3 FOVs, ~30 cells/FOV, for R-CaMP2 and 4 FOVs for jRGECO1a and jRCaMP1a. Colored bands indicate ± s.e.m.. Dishes were stimulated with 1 ms field stimulation pulses. RGECI fluorescence was recorded at 50 Hz. **c)** Kinetics of the RGECIs, shown by plotting data in (b) normalized to peak ΔF/F. **(d)** Cultured hippocampal neuron coexpressing H2B-jRGECO1a (magenta) and eTsChR (green). Scale bar 10 μm. **e)** Steady state photocurrents of eTsChR and ChR2(H134R) in cultured neurons held at -65 mV (1 s pulses, 488 nm, n = 6 cells for each construct). Inset: photocurrent response to 2 W/cm^2 488 nm illumination. **f)** Channelrhodopsin activation time constant as a function of 488 nm illumination intensity. Inset: photocurrents during illumination start. **g)** Closing time constants. Inset: photocurrents during illumination stop. **h)** Optogenetic stimulation induced action potentials and corresponding fluorescence transients in a cultured neuron expressing jRGECO1a and eTsChR. Pulses of blue light (488 nm, 10 ms, 680 mW/cm^2) drove action potentials (*), which were identified via fluorescence of a far-red voltage-sensitive dye, BeRST1 [133] (1 μm, black). Fluorescence transients of jRGECO1a accompanied action potentials (red). TTX (1 μm) silenced activity in both the voltage (pink) and Ca^{2+} (grey) channels, confirming that signals arose from neural activity and not optical crosstalk. Voltage imaging was performed at 500 Hz with 0.7 W/cm^2 640 nm light and calcium imaging was performed at 20 Hz with 1.1 W/cm^2 561 nm light. All error bars indicate mean ± s.e.m..

Construct	Single AP max ΔF/F (%)	τ_{on} (ms)	τ_{off} (ms)	τ_{bleach} (s)
jRGECO1a	54 ± 10, n = 4 FOV, ~30 cells/FOV	47.2 ± 1.0	443 ± 38	80.5 ± 5.1, n = 9 cells
R-CaMP2	31 ± 3, n = 3 FOV, ~30 cells/FOV	26.3 ± 1.0	271 ± 20	61.9 ± 2.8, n = 8 cells
jRCaMP1a	17 ± 4, n = 4 FOV, ~30 cells/FOV	61.2 ± 2.1	1600 ±160	37.8 ± 2.1, n = 8 cells

Table 2.1: *In vitro* characterization of RGECIs. Quantification of action potential responses in cultured neurons in **Figure 2.1**, and photobleaching kinetics in HEK293T cells. Action potential magnitudes and sensor kinetics are from 3 FOVs for R-CaMP2 and 4 FOVs for jRGECO1a and jRCaMP1a in separate dishes. Dishes were stimulated with 1 ms field stimulation pulses while imaging RGECI fluorescence at 50 Hz with 2.45 W/cm^2 561 nm illumination. Photobleaching measurements were performed in HEK293T cells under 44 W/cm^2 561 nm illumination (compared to 0.1 W/cm^2 used in slice imaging). All values are reported as mean ± s.e.m..

constant (τ_{bleach} = 81 ± 5 s, I_{561} = 44 W/cm^2, n = 9 cells), followed by R-CaMP2 and jRCaMP1a (**Table 2.1**). Under typical imaging conditions (I_{561} = 0.1 W/cm^2), photobleaching of jRGECO1a was thus < 10% during 1 hr of continuous imaging. While photobleaching is often a concern for 1P imaging, these results established that this effect was minor for wide-area imaging of jRGECO1a. We selected jRGECO1a for its superior sensitivity and photostability.

mApple-based fluorescent sensors, including jRGECO1a, are known to undergo photoswitching under blue light illumination[69,70]. We thus sought a blue-shifted channelrhodopsin that could drive spikes in jRGECO1a-expressing neurons at blue intensities low enough to avoid optical crosstalk. TsChR is the most blue-shifted published ChR (**Figure 2.1a**), but was initially reported to produce only ~40% as much photocurrent as ChR2(H134R)[130] and so has not previ-

ously been used in optogenetic applications. Addition of a Kir2.1 trafficking sequence (TS) and a GFP expression tag to TsChR led to excellent trafficking in cultured neurons (**Figure 2.1d**). We called this construct ėTsChR-eGFP. Compared to ChR2(H134R), ėTsChR had higher steady state photocurrents (470 ± 42 vs. 288 ± 60 pA, $p = 0.034$, Student's t-test, $n = 6$ neurons each, **Figure 2.1e**). At the highest blue light intensity tested (33 W/cm^2), ChR2(H134R) passed a steady state photocurrent of 288 ± 60 pA; ėTsChR passed the same steady state photocurrent at 100-fold lower intensity (0.33 W/cm^2). Compared to ChR2(H134R), ėTsChR also had higher maximum steady state photocurrent densities (13.2 ± 1.2 pA/pF vs. 7.8 ± 2.0 pA/pF, $p = 0.044$, Student's t-test, $n = 6$) and faster on- and off- kinetics (**Figure 2.1f,g**).

We co-expressed jRGECO1a and ėTsChR in cultured rat hippocampal neurons, and used the far-red voltage-sensitive dye BeRST1[133] as a ground-truth reporter of neural spiking. Flashes of blue light (0.7 W/cm^2, 10 ms) induced action potentials, reported by BeRST1 fluorescence, and Ca^{2+} transients, reported simultaneously by jRGECO1a fluorescence (**Figure 2.1h**). The sodium channel blocker TTX (1 μM) eliminated the light-evoked transients in both the BeRST1 and jRGECO1a fluorescence channels, confirming that the jRGECO1a response reflected spiking-dependent Ca^{2+} influx and that the optogenetic stimulation did not induce detectable photo-artifacts in the jRGECO1a fluorescence.

Cytoplasmic expression of jRGECO1a in brain slices led to a high level of fluorescence background from reporter present in neuropil, even with the optically sectioned imaging approaches described below (**Figure 2.2a**). To facilitate imaging in tissue, we fused jRGECO1a to a Histone-2B (H2B) tag to localize expression to the nucleus (**Figure 2.1d** and **Figure 2.2b**), as previously

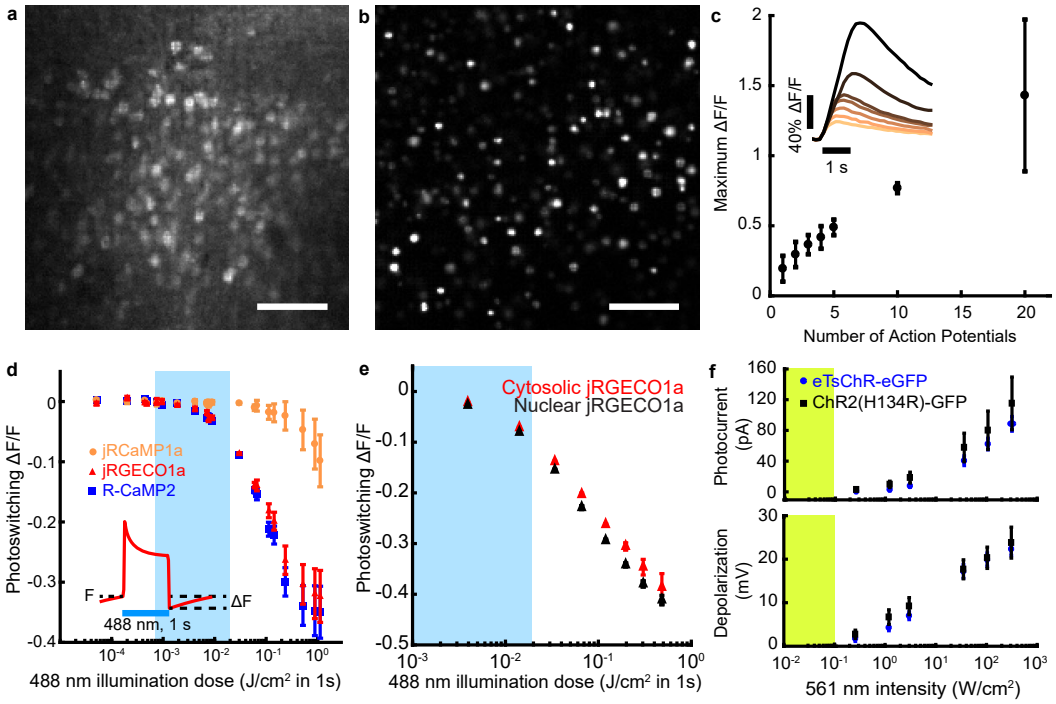

Figure 2.2: Characterization of soma-localized RGECIs and eTsChR. (a,b) Maximum intensity projections of Hadamard z-stacks from acute cortical slices prepared from mice injected with (a) cytosolic AAV1-syn-NES-jRGECO1a or (b) nuclear-targeted AAV9-syn-DO-H2B-jRGECO1a. Scale bars 100 μm. **(c)** Maximum ΔF/F of H2B-jRGECO1a fluorescence vs. number of evoked action potentials in cultured neurons, stimulated via current injection (n = 3 cells). Inset: example responses to increasing numbers of action potentials. **(d)** Blue-light induced photoswitching of cytosolic RGECIs in HEK293T cells under basal Ca^{2+} levels. RGECI fluorescence was recorded at 50 Hz with illumination at 561 nm, 80 mW/cm^2. Blue illumination (1 s pulses, 488 nm) was added to the yellow illumination. Photoswitching was quantified as the decrease in fluorescence following blue light illumination compared to the initial fluorescence (inset), n = 3 FOV, ~50 cells/FOV, for each construct. **(e)** Comparison of photoswitching in cytosolic and nuclear-localized jRGECO1a. Blue bar represents range of illumination doses used for optogenetic stimulation in this study. **(f)** Activation of channelrhodopsins as a function of 561 nm illumination intensity. Top: Steady state photocurrents in cultured neurons voltage clamped at -65 mV. Bottom: Voltage depolarization under current-clamp with an initial potential of -65 mV. Yellow bar indicates typical jRGECO1a imaging intensities. Acquired from cultured rat hippocampal neurons, n = 6 for each construct. All error bars indicate mean ± s.e.m..

	éTsChR	ChR2(H134R)-GFP	p-value, Student's t-test
Access resistance (MΩ)	12.3 ± 1.5	12.4 ± 1.3	0.96
Membrane resistance (MΩ)	633 ± 84	467 ± 88	0.20
Membrane capacitance (pF)	36.5 ± 4.8	44.9 ± 9.7	0.45
Resting potential (mV)	-36.5 ± 4.8	-44.3 ± 2.9	0.13

Table 2.2: *In vitro* characterization of eTsChR. Patch parameters of cells in **Figure 2.1**. All values are reported as mean ± s.e.m., n = 6 cells throughout.

done for zebrafish[134] and rat[135] brain imaging. The nuclear-localized H2B-jRGECO1a showed clearly resolved nuclei with little background between the cells. In cultured neurons, H2B-jRGECO1a responded to single action potentials with good sensitivity ($\Delta F/F$ = 19.4 ± 5.3%, n = 3 cells), but with slower kinetics than the cytosolic reporter, (τ_{on} = 167 ± 27 ms, τ_{off} = 1,400 ± 270 ms) consistent with previous measurements of nuclear Ca^{2+} dynamics (**Figure 2.2c**)[136,137].

We tested for optical crosstalk between actuator and reporter channels in cells co-expressing the optimized AON constructs. Due to the high sensitivity of éTsChR, the blue light doses needed to elicit spikes (0.7 W/cm^2 for 10 ms, λ = 488 nm) induced minimal photoartifact in either cytoplasmic or nuclear jRGECO1a compared to a single-spike Ca^{2+} signal (-2% photoartifact in **Figure 2.2d** vs. 19% spike response in **Figure 2.1h**, **Figure 2.2e**). Crosstalk from direct blue light excitation of jRGECO1a fluorescence was avoided in the experiments below by interleaved optogenetic stimulation and fluorescence imaging.

The yellow light used for Ca^{2+} imaging (561 nm, 0.1 W/cm^2) induced in éTsChR a steady-state photocurrent less than 0.5 pA (**Figure 2.2f**), far too small to trigger spurious action potentials. Expression of éTsChR did not significantly affect neurons' membrane resistance, membrane ca-

pacitance, or resting potential compared to controls (**Table 2.2**). eTsChR and H2B-jRGECO1a formed a suitable actuator/reporter pair for crosstalk-free 1P AON.

2.3.2 Hadamard microscopy enables optical sectioning in ultra-widefield images of acute brain slices

We next sought to perform wide-area optically sectioned imaging of the AON constructs in acute brain slices. To achieve high light collection efficiency over a wide FOV, we designed a microscope system around a low magnification high numerical aperture objective (Olympus MVPLAPO 2 XC, $NA = 0.5$). In wide-field epifluorescence mode, this microscope imaged a 4.6 mm FOV, large enough to capture most of a hemisphere of a coronal brain slice, with nominal 2.25 μm lateral resolution set by the pixel size on the sCMOS detector. Apart from the optical filters and the mechanical mounts, all elements of the microscope were off-the-shelf components (**Section 2.2.4.1**).

To achieve optical sectioning over a wide FOV, we developed a structured illumination approach based on Hadamard encoding. We placed a digital micromirror device (DMD) in the illumination path to enable arbitrary spatiotemporal patterning of the fluorescence excitation. Each DMD pixel mapped to 6.3 μm in the sample plane. The DMD modulated the excitation light with a series of binary illumination patterns such that neighboring sample locations were illuminated with orthogonal intensity sequences ($P_1, P_2, \ldots, P_n$ in **Figure 2.3a**). Raw data consisted of a series of images ($F(t_1), F(t_2), \ldots, F(t_m)$ in **Figure 2.3b-1**) acquired with each illumination pattern, which were then demodulated to yield images of the scattered light for each illumination location (**Figure 2.3b-2**). Software binary masks then rejected scattered light (**Figure 2.3b-3**), akin

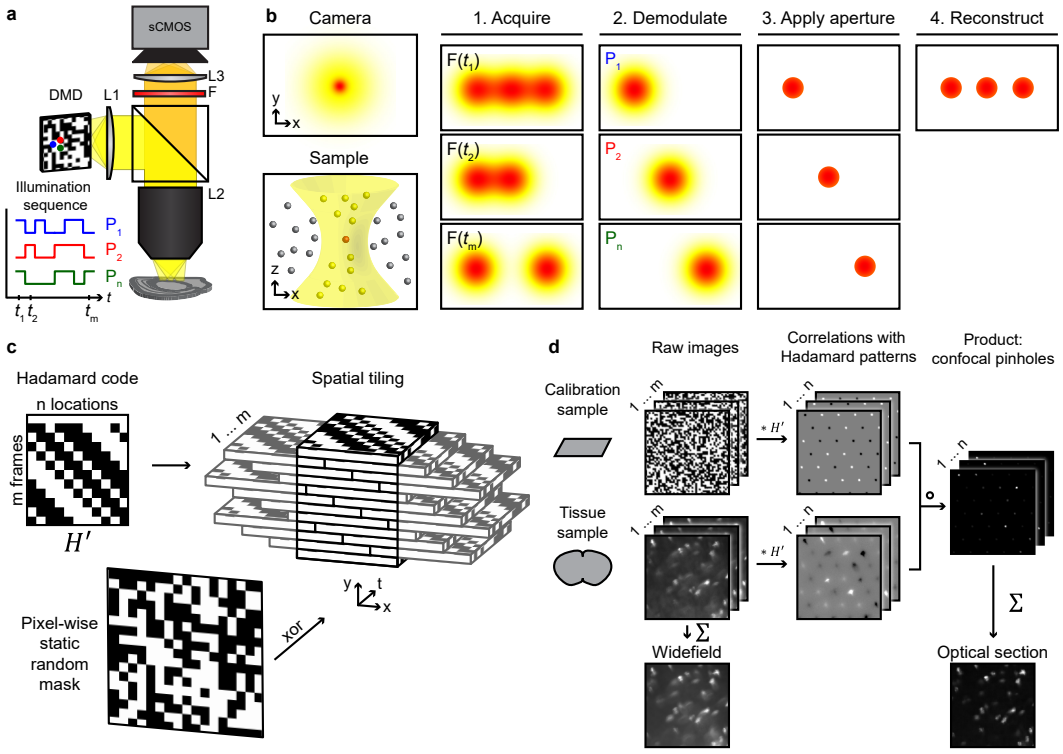

Figure 2.3: Optical sectioning by Hadamard microscopy. (a) Schematic of ultra-widefield microscope, showing orthogonal illumination sequences in neighboring DMD pixels $(P_1, P_2, \ldots, P_n)$. The full sequences have a 50% duty cycle. **(b)** Left: In a thick, scattering sample, the in-focus light (red) is dispersed by scattering and mixed with out-of-focus light (yellow). Right: Hadamard microscopy protocol. (1) The sample is illuminated with orthogonal functions of time at adjacent points in space. (2) The images are demodulated by matched filtering with the illumination sequence. (3) Scattered light is rejected by a software aperture. (4) The optically sectioned image is reconstructed from a sum of the demodulated images. **(c)** Codes from a Hadamard matrix were tiled to fill image space. The number of elements in the Hadamard code determined the number of frames in the pattern sequence. A random mask was applied to invert the code in 50% of illumination pixels, yielding pseudorandom patterns with flat spatial and temporal power spectra. **(d)** Raw images were acquired in a calibration sample (a thin homogeneous fluorescent film) and a tissue sample, one frame per Hadamard pattern. Cross-correlation maps between microscope data and Hadamard codes produced arrays of peaks corresponding to signals from distinct sample regions. Negative peaks corresponded to pixels whose Hadamard sequence was inverted. Pixel-wise multiplication of the demodulated images from the calibration sample and from the tissue sample led to multi-point confocal images. These images were summed to produce an image reconstruction. Detailed description in **Section 2.2.4.4**.

to physical pinholes used in confocal microscopy. The sum of images over all illumination locations yielded an optical section (**Figure 2.3b-4** and **Section 2.2.4.4**). The Hadamard algorithm is linear and local, i.e. the image resulting from two distinct sources is the sum of the images of the individual sources; and the final intensity value at each pixel depends only on signals acquired at that pixel. Thus the results are independent of the sample and do not require any specialized post-processing.

To make all projected DMD pixels mutually orthogonal would require prohibitively long digital codes (~10^6 samples), but because light scatter is mostly local, repeating the codes periodically at separations larger than the scattering point-spread function resulted in minimal crosstalk (**Figure 2.3c**). Residual crosstalk between repeated codes was scrambled by inverting the sequence of a randomly selected 50% subset of the pixels (**Figure 2.3c** and **Section 2.2.4.2**). This procedure resulted in series of patterns with 50% duty cycle, uniform mean illumination across the sample, and uniform spatial and temporal spectral density. By varying the number of frames in the Hadamard sequence, one can systematically trade time resolution vs. background rejection. The workflow for acquiring and analyzing Hadamard images is summarized in **Figure 2.3d**. A link to the software is given in **Section 2.2.5**. Application of compressed sensing algorithms to Hadamard microscopy enabled signal extraction at half the frame rate of the camera (**Figure 2.10** and **Chapter 3**), though this improved time resolution was not required for the applications described in this Chapter.

We compared Hadamard microscopy to two other SIM techniques, stripe SIM [51] and HiLo [139], all implemented using the same DMD and optics. Images of 200 nm fluorescent beads in agarose

were used to estimate the point-spread functions (PSFs) of the three techniques in a non-scattering medium. As, expected, line sections through the three PSFs gave identical lateral (FWHM 2.7 μm) and axial (FWHM 14.0 μm) resolution near the focus (**Figure 2.4**). For the low-magnification, wide-area implementation described here, the resolution in all three cases was determined by the intersection of the pixel-size-limited DMD illumination spots and the camera collection PSFs. We performed optical simulations to explore whether lateral shifts between DMD pixels and the smaller camera pixels would lead to spatially varying spatial resolution. For the parameters of our experimental setup, the changes in spatial resolution were < 5% in lateral resolution and < 10% in axial resolution, so these effects were subsequently neglected.

The three imaging techniques differed critically in imaging parameters not captured by the FWHM of the PSFs, however. Stripe SIM and HiLo PSFs had out-of-focus conical lobes, a consequence of out-of-focus points emitting along the same rays as in-focus and laterally offset points. These lobes did not lie along either the lateral or axial line sections through the PSF, so they did not contribute to the PSF dimensions as usually characterized, but they contributed to substantial out-of-plane total fluorescence (**Figure 2.4b**). Hadamard images lacked this artifact because use of multiple illumination patterns resolved ambiguities in assignment of out-of-focus fluorescence. For Hadamard microscopy, the integrated the PSF in the transverse (x-y) plane decayed to 15% of its peak at a defocus of -30 μm, whereas by the same measure HiLo retained 38% of peak fluorescence and stripe SIM retained 62% of peak fluorescence (**Figure 2.4b**). Thus HiLo and stripe SIM suffered ~2.5-fold and ~4-fold higher background than Hadamard, respectively.

For the purpose of rejecting out-of-focus background fluorescence in tissue, the integrated

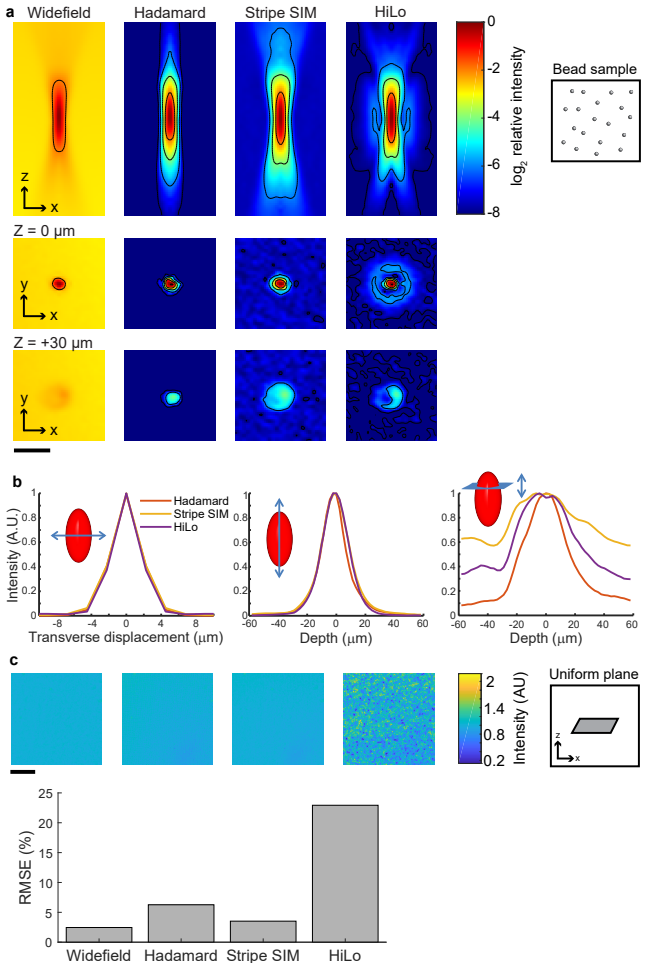

Figure 2.4: Characterization of Hadamard microscopy. ***(continues)***

(Figure 2.4 continued) **Characterization of Hadamard microscopy.** (a,b) Comparison of structured illumination microcopy (SIM) optical sectioning methods using sub-diffraction beads. **(a)** Images show (left to right): Wide-field epifluorescence, Hadamard microscopy using 12 patterns, stripe SIM with period 4 pixels and four phases, and HiLo microscopy using DMD-projected pseudorandom patterns. Top row: Radially averaged meridional cross-section of the point-spread function (PSF). Second row: transverse cross-section at the focal plane. Third row: transverse cross-section at 30 μm defocus. For all (a) the color scale is logarithmic, and contours were drawn on every 4-fold change in intensity. Scale bar is 20 μm, isotropic. **(b)** (Left and center) Lateral and axial line profiles through the PSF show equivalent resolution for the three sectioning methods. (Right) Integrated intensity in transverse cross-sections reveals off-axis spurious side lobes in stripe SIM and HiLo which contribute to out-of-focus crosstalk. **(c)** A uniform fluorescent plane at the focal plane resulted in larger inhomogeneities when imaged using HiLo in comparison with the other methods, a consequence of inhomogeneities in HiLo illumination [138]. The fractional noise in HiLo did not decrease with increasing photon counts. Top: Optical section images of the uniform plane, all shown at the same linear color scale. Bottom: Deviations from uniformity in the images on top. Hadamard and stripe SIM microscopies avoided this artifact by providing illumination whose time-average intensity was precisely the same at all sample points. Scale bar 200 μm. For all panels, each sample was imaged in matched conditions for all methods (number of images, illumination intensity, acquisition time). Detailed description in **Section 2.2.4.8**.

transverse fluorescence, not the more commonly used axial line section, is the critical parameter. Thus we expected that Hadamard microscopy would perform better than stripe SIM or HiLo in resolving single-cell signals in densely expressing tissues. **Figure 2.4c** and the Discussion compare the technical noise and shot noise properties of Hadamard and other SIM techniques. Hadamard performed as well as or better than the other techniques by these parameters.

We compared the performance of the three structured illumination techniques in brain tissue (**Figure 2.5**). The sample comprised an acute 300 μm-thick coronal brain slice, expressing nuclear-targeted jRGECO1a throughout cortex and striatum, and membrane-targeted CheRiff-GFP restricted by an Rbp4-Cre driver to a subset of Layer 5 (L5) pyramidal cells (**Figure 2.5a**). Hadamard images clearly resolved individual cells, whereas wide-field epifluorescence did not (**Figure 2.5b**). In the stripe SIM and HiLo images, out of focus nuclei appeared as bright rings, a consequence of the conical lobes on the PSF, which prevented clear separation of single-cell images (**Figure 2.5c**). Light scattering caused the Hadamard signal to decay as a function of image depth with a length constant of 27 μm in acute brain slices (**Figure 2.5d,e**) and 113 μm in fixed slices. The difference in signal attenuation was attributed to decreased light scattering after the fixation process.

To quantify the ability of Hadamard microscopy to resolve single-cell signals, we used high-resolution confocal microscopy to make ground-truth maps of the spatial distribution of nuclei in fixed slices densely expressing nuclear jRGECO1a. We then simulated Hadamard images of these cells in scattering tissue and estimated the crosstalk, i.e. the spurious contribution from all other cells to the fluorescence signal ascribed to each nucleus (**Section 2.2.4.8**). In cortical layer 2/3,

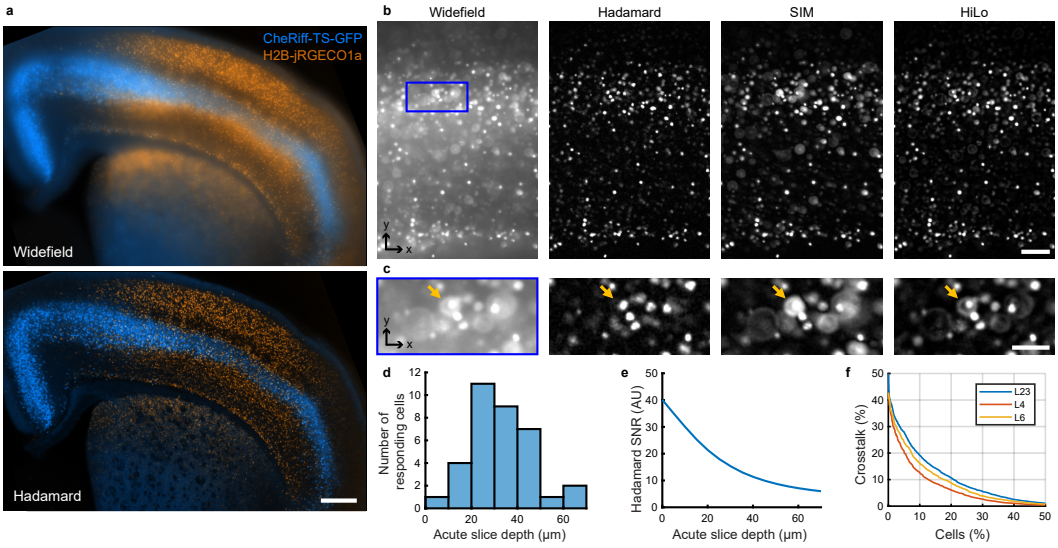

Figure 2.5: Hadamard microscopy resolves individual H2B-jRGECO1a labeled neurons in acute brain slices. **(a)** Two-color fluorescence maximum-intensity projections acquired from an acute brain slice expressing H2B-jRGECO1a broadly in cortex and striatum and membrane targeted CheRiff-TS-GFP in L5 pyramidal cells. Top: wide-field epifluorescence. Bottom: Hadamard image. Scale bar 500 μm. **(b)** Images acquired with different 1P computational optical sectioning methods. Images were acquired in the same sample with matched conditions (number of images, illumination intensity, acquisition time). The sample comprised an acute brain slice expressing H2B-jRGECO1a. Images show (left to right): Wide-field epifluorescence, Hadamard microscopy using 12 patterns, SIM with period 4 pixels and four phases, and HiLo microscopy using DMD-projected speckle patterns. Scale bar 100 μm. The blue box region is expanded in (c). **(c)** Hadamard microscopy avoids defocus lobes present using other methods. The orange arrows indicate a defocused cell that is rejected by Hadamard microscopy but appears in the other techniques. All images use the same linear scale of normalized grey values. Scale bar 50 μm. **(d)** Depth distribution of responsive cells during Hadamard functional recording, measured by high resolution confocal microscopy acquired after the functional measurement and registered to the Hadamard images. The depth was 32.2 ± 12.7 μm (mean ± std. dev., n = 35 neurons). **(e)** Depth-dependent decay in SNR for Hadamard microscopy in acute slices. Decay length was σ_z = 27 μm. **(f)** Estimated distribution of crosstalk in neuronal recordings using Hadamard microscopy. Only 10% of cells had more than 20% crosstalk (fluorescence attributable to other cells) in L2/3 (**Section 2.2.4.8**).

only 10% of the cells received more than 20% crosstalk from other cells. The crosstalk was lower in other brain regions (**Figure 2.5f**). Cell nuclei had a stereotyped round and localized shape. The degree of crosstalk could be estimated on a cell-by-cell basis via shape deviations. If desired, cells with crosstalk beyond a threshold value could be discarded from the analysis, though this procedure was not used here. Hadamard microscopy thus enabled optically sectioned imaging with single-cell resolution over wide fields of view in acute brain slices.

2.3.3 Mapping excitability in acute slices

To map neural excitability, we applied Hadamard microscopy with simultaneous optogenetic stimulation in acute mouse brain slices expressing the actuator-reporter pair. We co-injected AAV9-hSyn-DO-H2B-jRGECO1a and AAV9-hSyn-ĕTsChR in cortex and striatum of wild-type P0-2 mouse neonates (**Figure 2.6a**). Both proteins expressed well and were readily visualized via Hadamard imaging in 300 μm acute brain slices from 3-week-old animals (**Figure 2.6b,c**). We performed Hadamard AON measurements in a region 2.3×2.3 mm, set by the size of the expressing region. Cell signals were acquired from a depth of 32±13 μm (**Figure 2.5d**).

To probe excitability, we exposed the slice to a series of wide-field blue stimuli of increasing strength, interleaved with Hadamard imaging of H2B-jRGECO1a with yellow light (561 nm, 100 mW/cm^2, **Figure 2.6d**). Hadamard images were first acquired for 2 s to establish baseline fluorescence. Then a brief burst of blue light pulses (470 nm, 8 pulses, 15 mW/cm^2, 5 ms duration, 20 Hz) evoked neural activity, followed by another 2 s of Hadamard imaging to record the response. This image-stimulate-image procedure was repeated at 10 s intervals, six times, with the

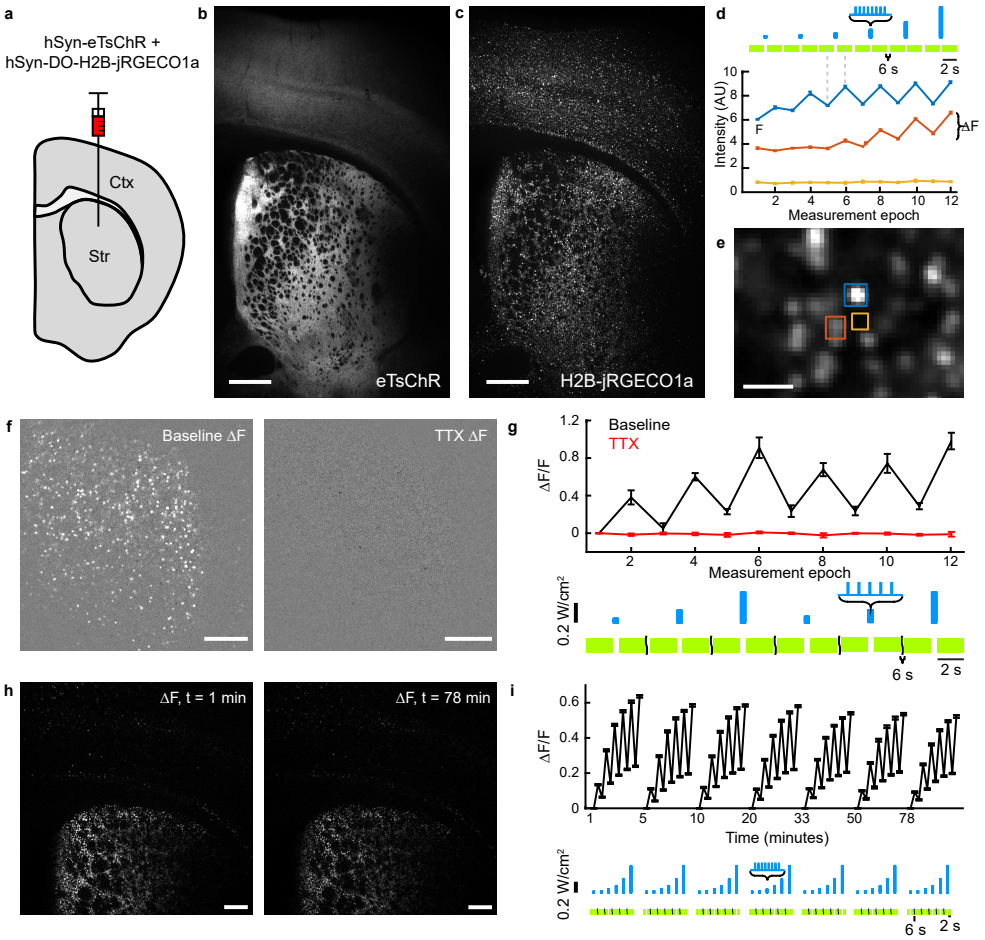

Figure 2.6: Robust AON in acute brain slices. **(a)** AAV9 viruses coding for hSyn-eTsChR and hSyn-DO-H2B-jRGECO1a were co-injected in neonatal mouse cortex and striatum. **(b)** Maximum intensity projection of a Hadamard z-stack of eTsChR expression in a coronal corticostriatal slice from a P21 mouse. **(c)** Same as (b) in the H2B-jRGECO1a channel. **(d)** Fluorescence traces from regions indicated in (e). Two cells showed optogenetically induced fluorescence transients, while a region between the cells showed no signal. Here the sets of 11 images acquired before and after each optogenetic stimulus were averaged to form single pre- and post-stimulus fluorescence values. Error bars represent s.e.m. over n = 11 Hadamard images. Scale bar 25 μm. F is defined as the average intensity of the first imaging epoch and ΔF is the signal increase following blue light stimulation. **(e)** Magnified view of (c) showing single-cell resolution. **(f)** Mean ΔF images from striatum before (left) and after (right) addition of TTX (1 μM). Images are scaled identically. **(g)** Mean ΔF/F per measurement epoch from n = 360 cells in (f) before TTX addition (black) and after TTX addition (red). Blue light stimulation consisted of 5 pulses at 12.5 Hz of 488 nm light at 60, 120, and 300 mW/cm^2, repeated twice. **(h)** One slice was repeatedly stimulated and imaged over 78 minutes with protocol in Fig. 3. Mean ΔF images from first run (left) and last run (right), scaled identically. **(i)** Average ΔF/F per measurement epoch for n = 3,195 cells in each run in slice shown in (h). Unless otherwise stated, all scale bars 250 μm. Error bars indicate ± s.e.m.

intensity of the blue light doubling upon each repetition to a maximum of 480 mW/cm^2. This measurement protocol reported the changes in intracellular Ca^{2+} concentration as a function of optogenetic stimulus strength.

Neighboring cells often showed distinct patterns of Ca^{2+} dynamics, while interstitial regions showed undetectable fluorescence (**Figure 2.6d,e**), confirming that Hadamard microscopy effectively rejected scatter and out-of-focus background. The yellow light used for Ca^{2+} imaging induced spurious activity in only 0.46 ± 0.03% of cells (n = 38,835 cells, 9 slices), establishing that the imaging light only weakly activated eTsChR. The sodium channel blocker tetrodotoxin (TTX, 1 μm) abolished blue light evoked responses slice wide, confirming that Ca^{2+} responses were due to action potential firing (**Figure 2.6f,g**) and, furthermore, that blue light-induced photoswitching was minimal.

We tested the long-term stability of the preparation. The optogenetically induced Ca^{2+} signal was stable over a 78 minute session comprising 7 repeated imaging cycles (**Figure 2.6h,i**). During this period the population-average optically evoked ΔF/F at the strongest stimulus decreased modestly from 64 ± 0.7% to 52 ± 0.7%, n = 3,195 cells. These results demonstrate the capability for repeated measurements over > 1 h in a single sample.

We used a 2D peak-finding algorithm to identify n = 6,102 responding cells in the Hadamard images of a single brain slice (**Figure 2.7a**). Cells showed different patterns of response in the striatum vs. cortex, but we also observed cell-to-cell variability within the cortex. To characterize this variability, we applied principal components analysis (PCA) to a set of single-cell recordings. First, we repeated the excitability measurement on 9 slices from 2 animals, recording from a to-

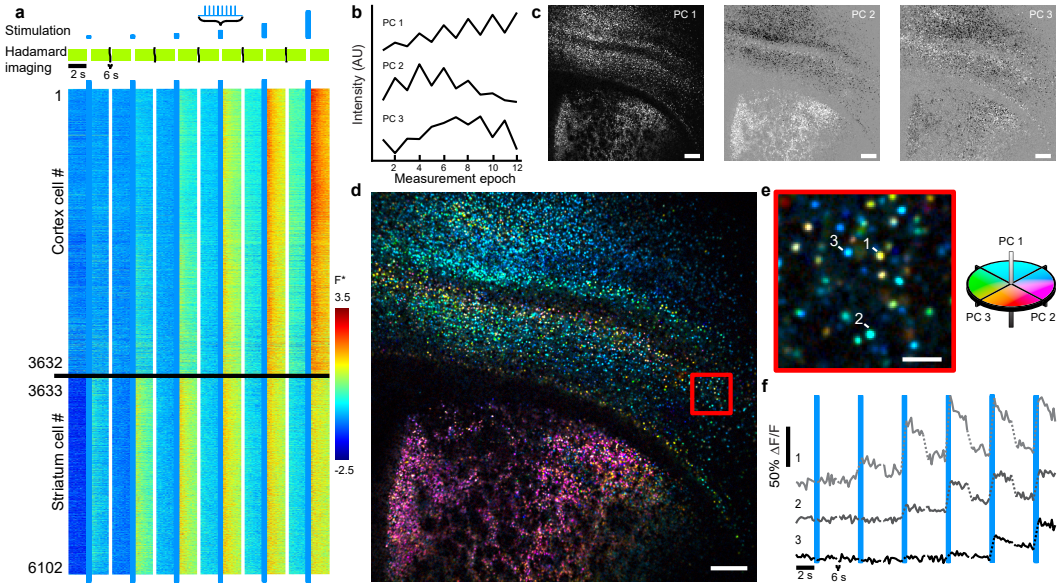

Figure 2.7: Ultra-widefield AON mapping of acute brain slices. (a) Top: Stimulation and imaging protocol. An FOV spanning cortex and striatum was stimulated with eight 5 ms pulses of 488 nm light at 20 Hz with intensities of 15, 30, 60, 120, 240, and 480 mW/cm^2. Bottom: heat map of 6,102 single-cell fluorescence traces acquired simultaneously. Individual fluorescence intensities traces were normalized as F* = (F - mean(F))/std(F). White breaks separate measurements at different optogenetic stimulus intensities. Imaging was performed at 5.6 Hz with 100 mW/cm^2 561 nm light. **(b)** Waveforms of main principal components from n = 31,754 cells. See **Section 2.2.7.4** for additional details. **(c)** Principal components from (a) projected into pixel space. **(d)** Image of the slice recorded in (a) with cells colored by the principal component amplitudes of the functional responses. **(e)** Close-up of the red boxed region of (d). **(f)** Three example single-cell fluorescence traces. Dotted lines indicate pauses in Hadamard imaging (400 ms during optogenetic stimulation, 6 s between stimuli). ΔF/F is defined relative to the intensity in the first imaging epoch. Scale bars 250 μm in (c, d) and 50 μm in (e).

tal of n = 32,103 cells across cortex and striatum. Measurement runs (comprising six measure-stimulate-measure sequences) were repeated at 5-minute intervals, 3 times per slice. PCA identified 3 main temporal components in the single-cell fluorescence responses (**Figure 2.7b,c** and **Section 2.2.7.4**). Examination of the PC temporal waveforms showed that PC1 measured overall fluorescence response amplitude, PC2 captured a left-right shift in the sigmoidal excitability profile, and PC3 largely captured a stimulus-dependent increase in baseline fluorescence.

We then decomposed the fluorescence waveform at each pixel into its principal components (PCs), and color-coded each pixel by its PC amplitudes (**Figure 2.7d,e** and **Section 2.2.7.4**). Despite coloring each pixel independently, individual cells appeared homogeneously colored in the resulting image (**Figure 2.7e**), consistent with the low cell-to-cell fluorescence crosstalk. These maps revealed striking colored bands running along the cortical layers, demonstrating different functional responses in different brain regions. Intriguingly, some layers appeared relatively homogeneous (L2/3, L4, L6), while cells in L5 had larger cell-to-cell variations in response. These results demonstrate that Hadamard AON can map excitability over thousands of individual neurons across large areas of acute brain slice.

2.3.4 Mapping pharmacological responses with Hadamard AON

Wide-area AON offers a means to map the cell type and region-specific effects of pharmacological or other perturbations on neural excitability. We performed excitability measurements on acute slices before and after applying the antiepileptic drugs (AEDs) retigabine (25 μM), carbamazepine (100 μM), and phenytoin (100 μM). To quantify the drug effect, we measured the pixel-by-pixel

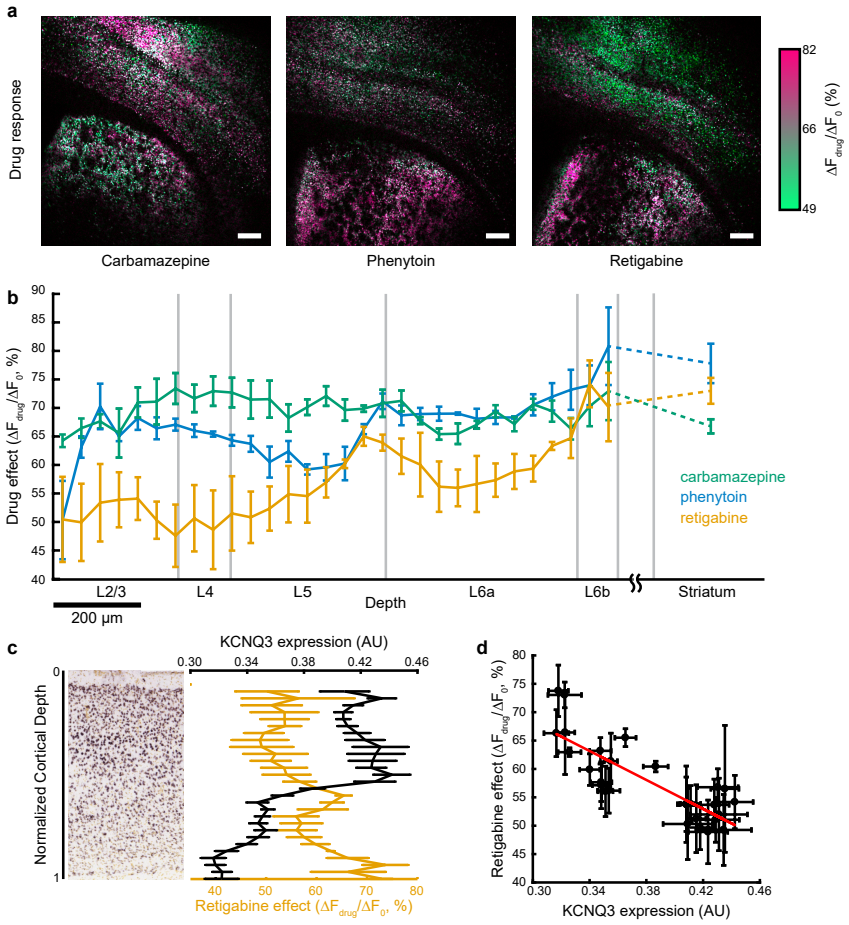

Figure 2.8: Mapping effects of anti-epileptic drugs (AEDs) on excitability. (a) Maps of AED effects on excitability. Slices were measured using the excitability protocol as in **Figure 2.7**. The protocol was repeated five times before drug addition and four times after addition of carbamazepine (100 μm), phenytoin (100 μm), or retigabine (25 μm). The ratio of mean optogenetically induced change in fluorescence for each cell before (ΔF0) and after drug addition (ΔFdrug) is encoded as color in a green to pink axis. Scale bars 250 μm. **(b)** Average drug response (ΔFdrug/ΔF0) as a function of cortical depth for n = 3 slices for each drug. All striatal cells in a slice were pooled into a single bin. Data represents n = 9,793 cells for carbamazepine, 11,858 cells for phenytoin, and 10,103 cells for retigabine. Error bars represent s.e.m. over n = 3 slices for each drug. **(c)** Left: in situ hybridization image from Allen Brain Atlas experiment #100041071 showing KCNQ3 expression in somatosensory cortex of a P28 mouse. Right: cortical depth dependence of retigabine drug effect (same as **Figure 2.4b**) and KCNQ3 expression level determined from in situ hybridization images of n = 11 slices from the Allen Brain Atlas. **(d)** Data from (c) showing effect of retigabine on excitability vs. KCNQ3 expression. Best fit line is indicated in red. Error bars indicate s.e.m., treating each slice as an independent measurement.

change in mean amplitude, ΔF, of the optogenetically induced response—a parameter close to the first principal component that emerged from the unsupervised analysis above. Each drug had different effects in striatum and cortex, and attenuated cortical excitability in a distinctive spatial pattern (**Figure 2.8a**).

We sorted cells into bins based on their cortical depth and visualized mean AED response as a function of cortical depth, averaged over $n = 3$ slices per drug (**Figure 2.8b**). Carbamazepine and phenytoin, both sodium channel blockers, showed relatively uniform suppression of excitability as a function of cortical depth, but retigabine showed a graded response, weakest in L6b and strongest in L4.

Retigabine is a specific positive allosteric modulator of Kv7 channels, and its primary target is thought to be the Kv7.2/7.3 heteromer[140], coded for by the genes KCNQ2 and KCNQ3. We examined the Allen Brain Atlas map of the expression level of KCNQ3[141], as determined by RNA in situ hybridization (ISH), and found statistically significant correlation between KCNQ3 expression level and effect of retigabine (Pearson's $r = -0.40$, 95% confidence interval between -0.022 and -0.69 obtained by bootstrapping, **Figure 2.8c-d**). Higher expression of KCNQ3 correlated with greater inhibition of excitability by retigabine, as one would expect for a potassium channel activator. An independent ISH study in adult animals reported a similar distribution of KCNQ2 and KCNQ3[142]. These results establish a connection between the Hadamard AON measurements and the underlying pattern of ion channels.

2.3.5 Probing functional connectivity with ultra-widefield AON

We next sought to extend the Hadamard AON platform to measurements of functional connectivity. Although slicing interrupts many long-range projections, optogenetic stimulation of axon terminals can nonetheless evoke local neurotransmitter release and postsynaptic responses[128]. We reasoned that sufficiently strong presynaptic stimulation would drive postsynaptic spikes, which could be detected via H2B-jRGECO1a.

To achieve this goal, the channelrhodopsin must traffic efficiently to axon terminals. We found that expression of éTsChR was predominantly localized to the soma and dendrites (**Figure 2.9a**). We thus explored CheRiff-TS-GFP (CheRiff), a blue-light sensitive, high photocurrent channelrhodopsin[82]. CheRiff trafficked well in axons (**Figure 2.9b,c**) and was 2.3-fold more sensitive to blue light than éTsChR. CheRiff was also more sensitive to yellow light, raising the possibility of spurious activation by the 561 nm imaging laser. Under typical imaging conditions (561 nm, 100 mW/cm^2) CheRiff photocurrent was 0.9% of the maximum photocurrent (95% confidence interval 0.8 to 1%, $n = 7$ cells, **Figure 2.9d**), whereas éTsChR photocurrent was < 0.1% of its maximum photocurrent (**Figure 2.2f**).

We designed an experiment to express CheRiff in L5 cortico-striatal neurons following a previously described protocol[143,144], and to test the postsynaptic response via Ca^{2+} imaging in the striatum. The CheRiff vector comprised CAG-DIO-CheRiff-TS-GFP (Cre-on CheRiff), which we injected into neonatal Rbp4-$Cre^{+/-}$ mice to target expression to a population of excitatory L5 neurons. We concurrently injected hSyn-DO-H2B-jRGECO1a (Cre-off nuclear Ca^{2+} indicator)

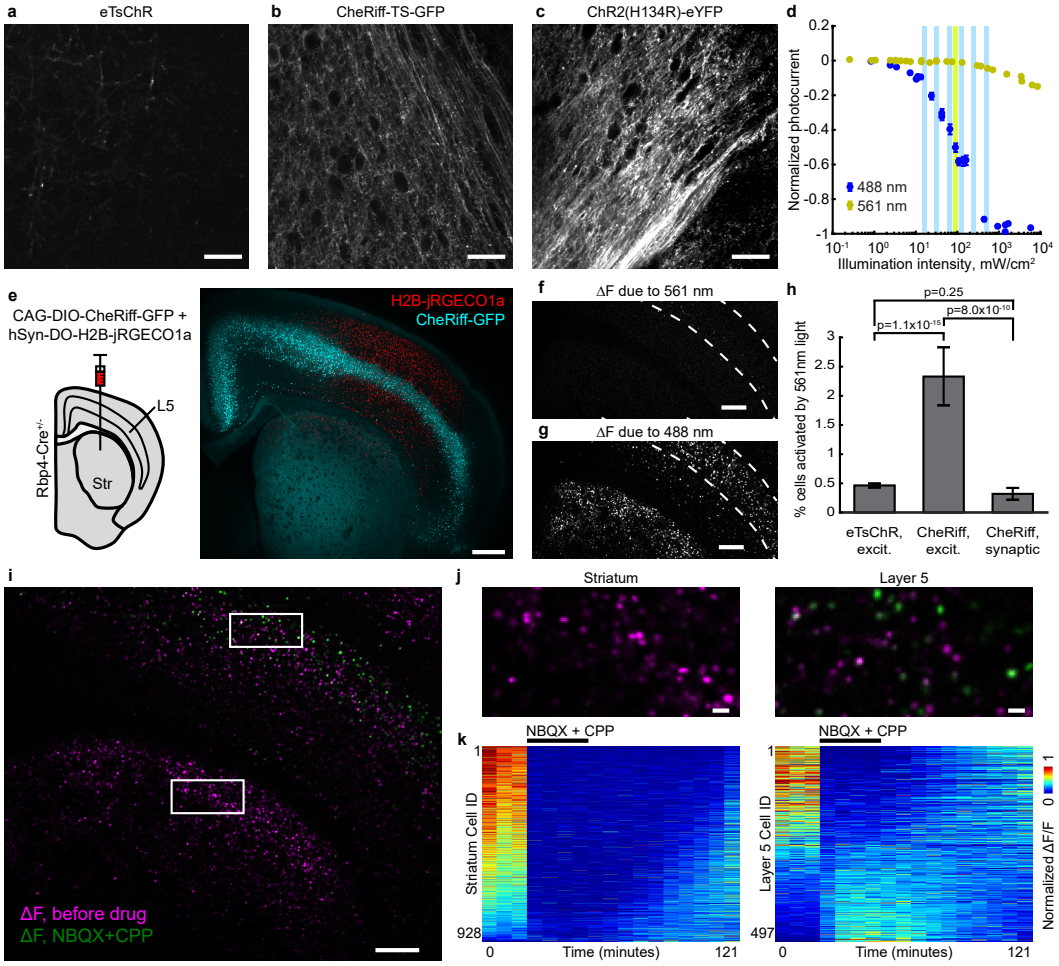

Figure 2.9: Mapping functional connections between neuronal subpopulations. *(continues)*

***(Figure 2.9 continued)* Mapping functional connections between neuronal subpopulations.** **(a-c)** Images of axonal trafficking of eTsChR, CheRiff-TS-GFP, and ChR2(H134R)-YFP, scaled to the same counts. Equal volumes of AAV2/9-hSyn-ChR2(H134R)-eYFP, AAV2/9-hSyn-CheRiff-TS-GFP, and AAV2/9-hSyn-eTsChR were injected in the left hemisphere in separate mice and coronal slices of the contralateral hemisphere were prepared after > 4 weeks. Images were acquired near the corpus callosum with 2-photon microscopy. Scale bars 50 μm in (a-c). **(d)** Comparison of CheRiff photocurrents in HEK293T cells induced by yellow (561 nm) and blue (488 nm) light. Vertical bars indicate intensities used in acute slice experiments. The blue illumination intensity to achieve 50% activation was 94 mW/cm^2 (88, 99 mW/cm^2 95% confidence interval, n = 7 HEK cells). **(e)** Left: viral constructs for mapping functional connections. Cre-dependent AAV9-CAG-DIO-CheRiff-GFP and AAV9-hSyn-DO-H2B-jRGECO1a were co-injected in Rbp4-Cre$^{+/-}$ neonatal mice. Right: at P21, CheRiff-GFP expressed in Cre+ L5 pyramidal cells, including corticostriatal projection neurons. H2B-jRGECO1a expressed broadly in cortex and striatum. Image represents a maximum intensity projection of a Hadamard z-stack. Scale bar 500 μm. **(f)** CheRiff activation by yellow (561 nm, 100 mW/cm^2) light. The image shows the difference between mean fluorescence of H2B-jRGECO1a in the 2nd and 1st second after onset of yellow light for Ca^{2+} imaging. Image represents a mean of n = 3 repetitions of the measurement. Spurious CheRiff activation would cause neural firing, which would lead to an increase in H2B-jRGECO1a fluorescence. **(g)** Mean ΔF induced by blue light stimulation, averaged over three runs. (f) and (g) are scaled identically, have 250 μm scale bars, and have dashed lines indicating Layer 5 of the cortex. **(h)** Comparison of optical crosstalk for different optogenetic actuators and protocols, as measured by percent of cells showing Ca^{2+} transients in response to onset of illumination with 561 nm light for fluorescence imaging. The three conditions corresponded to eTsChR in the excitability assay (co-expression of actuator and reporter in the same neurons), CheRiff in the excitability assay, and CheRiff in the functional connectivity assay (mutually exclusive expression of actuator and reporter). Error bars are calculated assuming a Poisson distribution with s.e.m. = $\sqrt{n_{\text{active}}}/n_{\text{total}}$. **(i)** Mean optogenetically induced fluorescence transients, ΔF, before (magenta) and after (green) addition of excitatory blockers, NBQX (10 μm) and CPP (10 μm). Stimulation and imaging were performed as in **Figure 2.7**. Images are the median of 3 runs before and 4 runs after adding excitatory blockers. Scale bar 250 μm. **(j)** Magnified views of indicated regions in striatum and Layer 5 in (i). Scale bar 25 μm. **(k)** Mean optogenetically induced fluorescence response, ΔF, for each cell before, in the presence of, and during washout of excitatory blockers. Left: striatum. Right: Layer 5. Each column represents the mean optogenetically induced ΔF of an experimental protocol as in **Figure 2.7a**. The slice was measured over 121 minutes (5-10 minutes between measurements, 22 minutes before last measurement). For visualization, each cell trace was normalized by its mean.

to drive reporter expression throughout striatum and cortex (**Figure 2.9e**).

First, we tested the slices for spurious activity elicited by the yellow imaging light. Very few striatal neurons showed a detectable increase in H2B-jRGECO1a signal caused by 561 nm imaging illumination (0.32 ± 0.001%, n = 3137 cells, 2 slices, **Figure 2.9f,g**), confirming that the yellow light did not excite axon terminals enough to drive postsynaptic spikes in most cases. This crosstalk performance is not significantly different from that in the éTsChR-based excitability measurements described above (0.46 ± 0.03%, n = 38,835 cells, 9 slices, p = 0.25, two-proportion z-test, **Figure 2.9h**). In excitability-style measurements with CheRiff, a significantly larger proportion of neurons showed imaging light-induced activation (2.3 ± 0.5%, n = 944 cells, 2 slices, $p = 8\times10^{-10}$). Thus, the superior axonal trafficking of CheRiff made it the preferred actuator for functional connectivity measurements, while the lower yellow-light crosstalk of éTsChR made it the preferred actuator for excitability measurements.

We then repeated the blue-light stimulation and imaging protocol previously used for excitability measurements while monitoring downstream responses in the striatum. Blue light induced nuclear Ca^{2+} transients across the cortex and striatum (**Figure 2.9i**). Blockers of excitatory transmission, NBQX and CPP, reversibly eliminated the responses in the striatum, Layer 6, and Layer 2/3, confirming that these responses were synaptically evoked (**Figure 2.9i**) and that there was negligible blue light crosstalk into the fluorescence signals.

To our surprise, addition of NBQX and CPP reversibly increased the optogenetically induced activity in a population of cells in L5 (**Figure 2.9j,k**). These cells showed little or no response to stimulation prior to addition of synaptic blockers (**Figure 2.9k**). The location of these cells

amidst the Rbp4 population suggested that these cells expressed both the actuator and reporter (likely a consequence of imperfect silencing of DO-H2B-jRGECO1a in Rbp4-Cre+ neurons[145]). The increase in excitability upon excitatory blockade then implies a disinhibitory mechanism, i.e. that these L5 cells received disynaptic inhibition from Rbp4-Cre labeled L5 pyramidal cells, which was relieved under excitatory blockade. The remaining cells in L5 showed a reversible decrease of activity in the presence of excitatory synaptic blockers, similar to the phenotypes in striatum and other cortical layers. These intermixed responses highlight the importance of performing single cell resolution measurements with Hadamard microscopy. Further, although Hadamard microscopy of jRGECO1a can only study supra-threshold responses, these results shown that judicious pharmacological applications can dissect a system's functional connectivity.

2.3.6 High-speed Hadamard AON with compressed sensing

Finally, we illustrate that Hadamard AON can be performed at high speed by using recently a complementary technique using compressed sensing, detailed in **Chapter 3**. The core idea is to take advantage of the low-rank dynamics of fluorescence fluctuations in neuronal samples. Since each neuron covers multiple camera pixels, every image has redundant information. In the context of a sufficiently long recording, a pair of images comprising a single Hadamard pattern and its complement contain enough information to infer the images that would have been recorded under illumination with any other Hadamard pattern. By inferring the complete set of Hadamard images for every pair of camera frames, this approach enables optically sectioned reconstructions at half of the camera frame-rate. **Figure 2.10** illustrates this approach. The sample comprised a

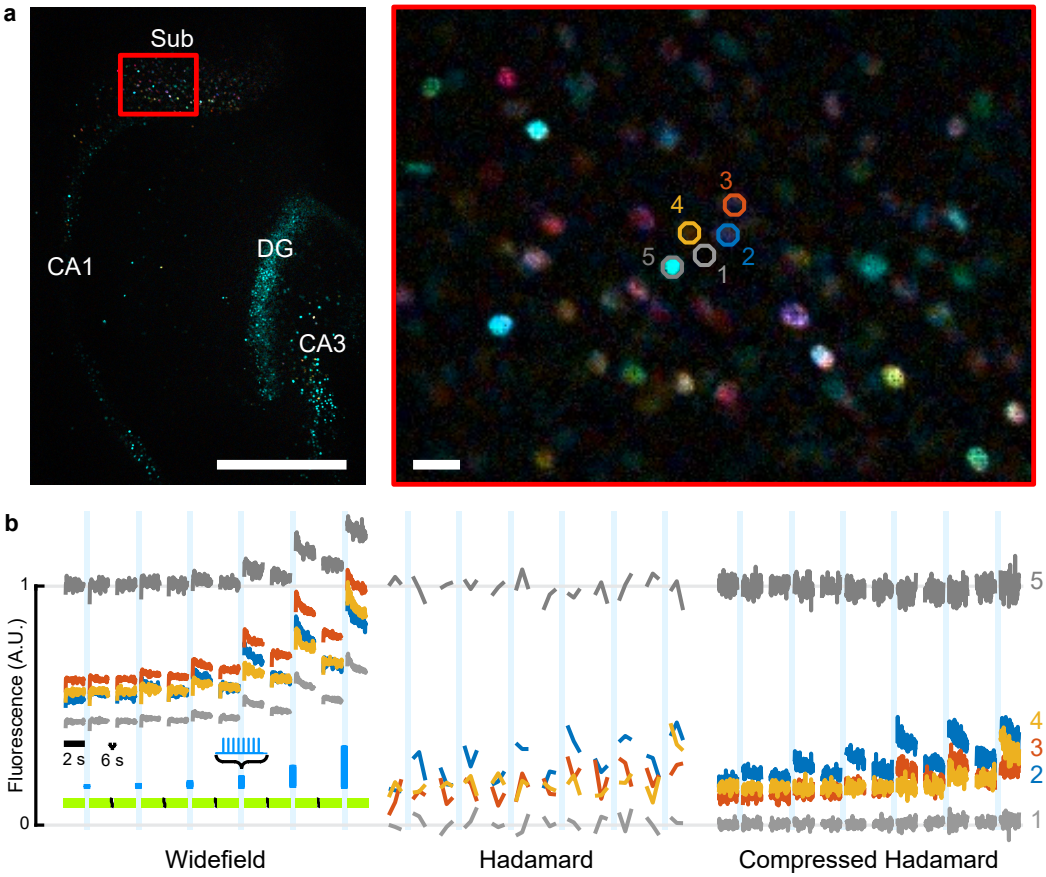

Figure 2.10: High-speed wide-area AON using Compressed Hadamard Imaging. **(a)** Left: PCA-colored map showing response of nuclear jRGECO1a to stepped optogenetic stimulation across the hippocampal formation. Sub: Subiculum, DG: Dentate gyrus, CA1/CA3: Cornu ammonis. Scale bar 0.5 mm. Right: Magnified view of the cyan rectangle shows the location of a background region (1, gray), three responding cells (2-4, colored), and a bright, non-responding cell (5, gray). Scale bar 20 μm. Color saturation was increased by 100% for display. **(b)** Comparison of fluorescence traces extracted from ROIs in (a) from the same recording, using three different analyses. Amplitude was scaled to normalize the baseline intensity of the brightest ROI. Left: Widefield data calculated as the sum of paired complementary patterns. Signals had a time resolution of 33 Hz, but included out-of-focus background. Camera framerate was 66 Hz. Middle: Conventional Hadamard analysis produced one optical section every 48 frames, possibly with errors due to changing cell intensities during the pattern period. Right: Compressed Hadamard analysis obtained high-speed optically sectioned movies with 33 Hz framerate. Both Hadamard optical sections show a zero-centered value for the background ROI (1) and flat brightness for a non-responding cell (5), but distinct optogenetic activation thresholds for each responding cell (2-4).

hippocampal slice co-expressing eTsChR and nuclear-localized jRGECO1a. To ensure that each nucleus was illuminated by multiple DMD pixels, we used a 10x objective (**Section 2.2.4.5**). The optogenetic stimulation was as in Figures **2.6** and **2.7**. The camera and DMD-patterned illumination were synchronized to run at 66 Hz.

Figure 2.10a shows a Hadamard image of the whole field of view, in which nuclei have been color-coded by the principal component amplitudes of their dynamic response, as in **Figure 2.7d**. A close-up image (**Figure 2.10b**) shows the individually resolved nuclei. A wide-field image sequence was calculated by averaging together pairs of frames with complementary illumination patterns. Hadamard reconstructions were calculated via the standard approach outlined above, and via the compressed sensing approach.

Regions 1 and 5 in **Figure 2.10a** corresponded to a cell-free interstitial region and a non-responsive (presumably dead) very bright cell, respectively, whereas regions 2 – 4 corresponded to optogenetically responsive cells. **Figure 2.10b** shows that the wide-field images had high time resolution, but suffered from out-of-focus crosstalk: the gray traces from regions 1 and 5 showed spurious optogenetically induced responses. In the conventional Hadamard movie, the intensity traces from regions 1 and 5 showed constant fluorescence, confirming effective background rejection. But these extracted traces had low time resolution. In the compressed sensing Hadamard movie, the intensity traces from regions 1 and 5 had the same time resolution as in the wide-field movie (33 Hz), but lacked background crosstalk as in the conventional Hadamard movie. Thus compressed Hadamard imaging provides a means to achieve simultaneously optical sectioning and high time resolution.

2.4 Discussion

Through detailed photophysical characterization of optogenetic actuators and reporters, we identified pairs that can be used in tandem with minimal 1P crosstalk. A pairing of CheRiff and jR-CaMP1b was recently demonstrated in cultured neurons, but crosstalk was not measured quantitatively and the genetic constructs were not tested in tissue[146]. Despite the well reported photophysical blue light artifacts in jRGECO1a, we found that sufficiently sensitive optogenetic actuators could induce neuronal responses at blue light intensities where these artifacts were minimal. The far blue-shifted channelrhodopsin, éTsChR, enabled measurements of intrinsic excitability, and the highly sensitive channelrhodopsin, CheRiff, enabled measurements of functional connectivity, in both cases with minimal crosstalk from the yellow imaging laser. Finally, nuclear localization of the reporter, combined with Hadamard structured illumination microscopy enabled resolution of single-cell signals across wide areas of brain slice. The resulting toolbox is well suited for studying suprathreshold phenotypes in acute brain slice, such as excitability of single neurons and functional connectivity of strong excitatory connections. These tools enable wide-area mapping of these properties in brain tissue, and studies on the effects of perturbations thereon.

Questions of where and how neuroactive compounds affect neuronal function are difficult to answer with conventional techniques. Typically, compound distribution is investigated by radiographic labeling experiments. Such results are convolved with possible nonspecific binding of the molecule and with expression of the target in the neuropil, preventing single cell identification. The 1P AON technique provides a high spatial resolution functional alternative to radiographic

mapping. We show differential response profiles for three AEDs—one molecularly specific drug, retigabine, whose response profile matched its known target distribution, and two non-specific drugs, carbamazepine and phenytoin. Measurements on other drugs may provide insights into their specific cellular and regional targets. Hadamard AON could also be used to probe the effects of neuropeptides, neuromodulators, hormones, genetic mutations, or environmental perturbations (e.g. temperature, oxygen, metabolites) on brain-wide patterns of neural excitability.

By extending these assays to measurements of functional connectivity, we show that this 1P AON toolbox can be also be used for circuit dissection. The all-optical connectivity assay of **Figure 2.9** shows that Rbp4-Cre positive neurons have a strong excitatory drive across striatum, consistent with previous results[147]. The net effect of layer 5 stimulation on other cortical layers was not previously well established—most L5 neurons are excitatory but also recruit strong inhibition via parvalbumin and somatostatin neurons across the cortical column[124,148]. We found a clear net excitatory effect of Rbp4-Cre neuron activation in many cells of L2/3 and L6a of the cortex. Within L5 we found a heterogeneous response, where inhibition outweighed excitation in Rbp4-cre positive neurons (and possibly others which remained nonresponsive during the entire experiment) but excitation outweighed inhibition in other neurons in L5. While this paper was in review, another study interrogated the same circuit with optogenetic stimulation and simultaneous triple whole cell patch clamp, with broadly similar conclusions[149], though the difficulty of patch clamp limited the measurements to a few tens of neurons overall.

Both 1P AON and Hadamard microscopy can be used independently and neither technique is limited to neuroscience applications. The far blue spectrum and excellent sensitivity of eTSChR

open the possibility to pair it with red-shifted fluorescent sensors of many other modalities, such as pH, cyclic AMP, or neurotransmitters. The broad spectral range of Hadamard microscopy opens possibilities for high-speed optically sectioned imaging of many different fluorescent reporters, including simultaneous imaging of multiple modalities.

There are many microscopy techniques which could in principle be used for AON in brain slices. Here we briefly outline the factors which led us to develop Hadamard microscopy rather than using an established technique. Spinning disk confocal microscopy (Toomre et al.,) in principle provides high temporal resolution and good optical sectioning, but existing spinning disk optics lack sufficient etendue to capture the FOV and NA of the wide-area objective. One could mimic the function of a spinning disk system by activating individual DMD pixels sequentially in a tiled array, acquiring one image per illumination pattern, and then using software spatial filtering to keep only the in-focus component of each point illumination pattern. This approach would yield the same PSF as Hadamard microscopy.

Unmixing techniques such as Hadamard microscopy cannot unmix shot noise. Here we compare the shot noise properties of the Hadamard images relative to DMD-based multi-focal confocal. Let S be the mean number of signal photons acquired in one camera pixel in one frame when the corresponding DMD pixel is turned on. Let α be the mean number of background photons acquired in camera pixel i in one frame when DMD pixel $j \neq i$ is turned on, averaged over all j within a block of N pixels. A simple analysis of the shot noise implies that in multi-focal confocal (i.e. one DMD pixel turned on at a time) the shot noise-limited signal-to-noise ratio is $\text{SNR} = \sqrt{S}$. A short calculation shows that in Hadamard microscopy, the shot noise-limited

SNR is approximately: SNR $= S/\sqrt{2\alpha}$.

If $\alpha < S/2$, then Hadamard is better; otherwise multi-focal confocal is better. We found experimentally that for $N = 12$, $\alpha/S = 0.51$, indicating comparable shot noise for the multi-focal and Hadamard approaches. For $N = 64$, we measured $\alpha/S = 0.26$, indicating superior performance of Hadamard over multi-focal confocal. In these comparisons, the total optical dose into the sample is greater for Hadamard than for multifocal. The duty cycle of illumination is $1/N$ for multifocal confocal, and $1/2$ for Hadamard, so for $N = 12$, Hadamard exposes the sample to 6-fold more light, and for $N = 64$, Hadamard uses 32-fold more light. While photobleaching and phototoxicity were not significant factors in the present experiments, the presence of these effects may favor multifocal confocal.

As discussed above, stripe SIM and HiLo techniques are alternatives which could be implemented with the same DMD optics as Hadamard microscopy. The improved PSF shape (relative to stripe SIM and HiLo) and the absence of static illumination noise (relative to HiLo) favored Hadamard microscopy. The contributions of background photons to the shot noise are identical in all three techniques. The lower temporal resolution of Hadamard relative to the other SIM techniques did not constrain the ability to map nuclear Ca^{2+} dynamics, though better time resolution may be needed for other fluorescent reporters. Improvement in the time resolution of Hadamard microscopy are possible via compressed sensing techniques, as shown in **Chapter 3**.

2P mesoscopes currently hold the record for most single neurons (~3000) recorded simultaneously in tissue[76]. 2P-mesoscopes have greater depth penetration than SIM techniques, making them more suitable for *in vivo* studies at present. Point-scanning based mesoscopes have achieved

pixel rates of ~ 2×10^7/s over 0.6 × 0.6 mm FOVs but the requirement to translate the beam long distances limits pixel rates over large FOVs (4.4 × 4.2 mm) to 5.6×10^6/s. Acousto-optical steering allows fast 2P random-access imaging[150], but this technique has only been demonstrated in a FOV of 0.5 mm, limited by the etendue of the acousto-optical deflectors. With 12-pattern Hadamard, we achieved comparable data rates of 1.2×10^7/s over a 4.6 × 2.3 mm FOV, with optically sectioned single-cell resolution. With improved control software to synchronize Hadamard patterns to the rolling shutter of the camera, pixel rates of 3.3×10^7 pixels/s over the entire 4.6 × 4.6 mm FOV would be possible with current camera technology. Finally, in contrast to 2P-mesoscopes, Hadamard microscopy is readily implemented with inexpensive LED or diode laser illumination across a broad range of excitation wavelengths.

Even when imaging in acute slices, one must achieve sufficient depth penetration to avoid damaged cells near the surface. Due to the great effort and low throughput of manual patch clamp measurements, it is typical to record at a depth of 50 μm or greater to minimize the risk of patching an unhealthy cell, though recent protocols suggest 30 μm is sufficient[123]. Our approach includes procedures to identify and exclude dead (non-responsive) cells. Hadamard AON measures large enough numbers of cells that one can afford to discard a few unhealthy cells, while still maintaining excellent statistics. The stable excitability and anticipated responses to tool pharmacology (**Figure 2.6**) establish that the cells assayed in our methods are adequately healthy from a functional perspective, despite being only ~30 μm below the surface.

For precisely targeted single-cell stimulation, 2P optics are essential, but for wide-area optogenetic stimulation, 1P optics are preferable, as follows: 2P optogenetic stimulation requires time-

average optical powers of 20 – 80 mW/cell[99,100,112]. Maximal safe steady-state 2P optical power into intact brain tissue is ~200 mW[114], limiting simultaneous 2P stimulation to at most a few tens of neurons at a time. 1P optogenetic stimulation requires approximately 10^6-fold lower time-average power (~50 nW/cell)[82], and thus is readily applied over wide areas of tissue to many thousands of cells simultaneously.

If a microscope can measure N cells in parallel, a measurement protocol takes time τ, and an acute slice is viable for time T, then the total number of cells that can be measured is NT/τ. A typical excitability measurement (including focusing and saving data) takes $\tau \sim 2$ min. In the present work, the field of view was limited by the range of viral gene expression, but in transgenic animals or with recently developed systemic gene delivery techniques[151], functional measurements could be made across an entire brain slice. With the current FOV, Hadamard microscopy could tile a complete sagittal slice in 7 acquisitions, or ~14 min. Brain slices typically remain viable for $T \approx 5$ hrs. Thus one could record from ~20 slices, enough to create a brain-wide functional map. Such a mapping technique could provide an unbiased approach to studying neuronal excitability, functional connectivity, and pharmacology across an entire brain.

Data and code availability

Constructs will be made available on Addgene. Code for Hadamard pattern generation and image reconstruction, as well as raw data examples are linked in **Section 2.2.5**.

2.5 Manuscript Information

Previously published as

A version of this chapter appeared in[152]:

S. L. Farhi*, V. J. Parot*, A. Grama, M. Yamagata, A. S. Abdelfattah, Y. Adam, S. Lou, J. J. Kim, R. E. Campbell, D. D. Cox, and A. E. Cohen, "Wide-area all-optical neurophysiology in acute brain slices," *Journal of Neuroscience*, pp. 0168–19, Apr. 2019.

Acknowledgements

We thank Vaibhav Joshi, Katherine Williams, and Melinda Lee for technical assistance. We thank Bernardo Sabatini for Rbp4-Cre mice, and Christopher Werley for assistance with the microscope design. We thank Daryl Lim for providing HiLo reconstruction code. Joshua Sanes provided support for the cloning of H2B-jRGECO1a. This work was supported by the Howard Hughes Medical Institute. Samouil L. Farhi was supported by an NSF Graduate Research Fellowship. Vicente J. Parot was supported by a Becas Chile scholarship. Work in David Cox's lab was supported by IARPA (contract #D16PC00002) and the Mind Brain Behavior Faculty Award of Harvard.

The author's contribution

Samouil L. Farhi designed, created, and calibrated the optogenetic constructs. Vicente J. Parot designed and built the Hadamard microscope with early assistance from Jeong Jun Kim. Abhinav

*These authors contributed equally.

Grama and Masahito Yamagata cloned H2B-jRGECO1a and characterized its response via patch clamp electrophysiology. Ahmed S. Abdelfattah cloned eTsChR. Yoav Adam helped with brain slice work. Shan Lou provided brain slices broadly expressing fluorescent proteins. Robert E. Campbell supervised the contribution from Ahmed S. Abdelfattah. David D. Cox supervised the contribution from Abhinav Grama. Adam E. Cohen conceived the Hadamard microscopy concept and supervised the research. Samouil L. Farhi and Vicente J. Parot acquired data. Samouil L. Farhi, Vicente J. Parot, and Adam E. Cohen analyzed data. Samouil L. Farhi, Vicente J. Parot, and Adam E. Cohen wrote the paper.

You should call it entropy, ... no one really knows what entropy is, so in a debate you will always have the advantage.

John von Neumann to Claude Shannon[153]

3

Compressed Hadamard microscopy

Structured illumination microscopy achieves optical sectioning via differential modulation of in-focus and out-of-focus contributions to an image. Multiple wide-field camera images are analyzed to recreate an optical section. The requirement for multiple camera frames per image entails a loss of temporal resolution compared to conventional wide-field imaging. Here we describe a computational structured illumination imaging scheme, Compressed Hadamard Imaging (CHI), that achieves simultaneously high spatial and temporal resolution for optical sectioning of three-dimensional samples with low-rank dynamics (e.g. neurons labeled with fluorescent activity reporters). We validate the technique with numerical simulations, and then illustrate

with wide-area optically sectioned recordings of membrane voltage dynamics in mouse neurons in an acute brain slice and of calcium dynamics in zebrafish brain *in vivo*.

3.1 Introduction

Fluorescence microscopy of dynamic biological samples is a powerful tool for studying physiology in its native context. An ever growing repertoire of fluorescent indicators reports on physiological variables, such as pH, calcium, glutamate, and membrane voltage[154,155]. One would like to measure these signals with simultaneously high spatial resolution, high temporal resolution, optical sectioning and wide field of view. However, this task is challenging in turbid tissues such as the brain, because background fluorescence and light scattering mix in-focus and out-of-focus signals.

Optical sectioning techniques often entail tradeoffs between imaging parameters. For instance, one- and two-photon point scanning techniques provide high spatial resolution and good background rejection, but are limited in imaging speed by their point-scanning nature, and ultimately by the electronic excited state lifetime of the fluorophores which sets the minimum time between pixels to ~10 ns for high-brightness fluorophores whose lifetimes are typically 2-4 ns. Camera-based systems offer intrinsically high data rates, good sensitivity and are readily coupled with wide-area optics, but do not natively provide optical sectioning. Spinning disk confocal microscopy provides high frame rates and optical sectioning, but the microlens array used in this technique does not provide adequate etendue for high light collection efficiency over a wide field of view.

Camera based optical sectioning using structured illumination has been used for decades to

reject background signals[48]. In structured illumination microscopy (SIM) one projects a series of spatially patterned beams onto the image plane and uses a camera to acquire wide-field fluorescence images[156]. In-focus and out-of-focus contributions to the images are modulated differently between illumination patterns, enabling computation of an optical section. SIM was first implemented with multiple phases of sinusoidal illumination patterns, together with a simple demodulation algorithm ("stripe SIM")[51]. Interest in physiological signals such as neuronal activity has motivated approaches to increase time resolution by acquiring fewer frames to calculate an optical section. A fast SIM technique (HiLo) used only two illumination patterns: one (pseudo)-random speckle pattern and one homogeneous pattern[139,58,55].

We recently introduced a SIM technique called Hadamard microscopy, where adjacent regions of the focal plane were illuminated with a set of temporally orthogonal patterns, and optically sectioned images were computed via matched filtering of the corresponding images, as detailed in **Chapter 2**. Hadamard microscopy was slower than the other SIM techniques because it required many camera frames (typically 12) to yield a single optical section. The maximum frame rate was 5.6 Hz in our recent implementation. This speed was fast enough to image a nuclear-localized Ca^{2+} indicator, but led to artifacts for signal sources whose intensity changed substantially during the time to acquire an optical section.

All three SIM techniques (stripe, HiLo, and Hadamard) yielded point-spread functions (PSFs) with identical full-width at half maximum (FWHM) along the axial and lateral line-sections, but Hadamard microscopy outperformed the other SIM techniques by other measures. The stripe SIM and HiLo PSFs had substantial out-of-focus conical lobes (lying neither along the axial nor

lateral directions), while Hadamard did not. These lobes are an unavoidable consequence of the use of a small number of structured illumination patterns: a fluorescent source that is simultaneously axially and laterally displaced from a given in-focus pixel will emit some light along the same rays as the source at the targeted pixel. There is no way, even in principle, to distinguish these rays. By using many illumination patterns, Hadamard microscopy resolves this ambiguity in signal assignment.

In images of acute brain slices, the conical lobes in stripe SIM and HiLo caused out-of-focus cells to have a 'halo' structure, which prevented clear resolution of single cells. Further, the (pseudo)-random illumination in HiLo imprinted static random noise, beyond the unavoidable photon shot-noise. This technical noise has been analyzed previously[138].

Ideally, one would like to combine the compact and low-noise PSF of Hadamard microscopy and the high time resolution of HiLo. Here we introduce a variant of Hadamard microscopy, termed Compressed Hadamard Imaging (CHI), which produces an optically sectioned movie at half the frame rate of the camera, matching the time resolution of HiLo. To achieve this dramatic speedup, we use our foreknowledge of the statistical structure of neural recordings. Namely, movies of neuronal dynamics tend to have a low-rank decomposition. The complete set of pixel intensities as a function of space and time can be approximately decomposed into a sum of images of individual neurons, each modulated with its own time-trace. Each neuron covers multiple pixels, so while a complete image of the neuron is not acquired in each camera frame, enough information is recorded to obtain an estimate of its fluorescence. Recent advances in microscopy signal processing have exploited the spatiotemporal structure of neuronal signals for unmixing,

parallel detection, and computational volume reconstruction[157–159].

We validate the technique of CHI by applying it to simulated movies of three-dimensional samples where the ground-truths of the source shapes and source dynamics are known. Then we apply this method to neuronal recordings using a genetically-encoded membrane voltage indicator in acute mouse brain slices, and to a genetically encoded cytosolic Ca^{2+} indicator in live zebrafish brain. These demonstrations achieve a ~100-fold improvement in the time resolution of Hadamard microscopy compared to the implementation described in **Chapter 2**, and match the speed of HiLo imaging.

3.2 Methods

3.2.1 Computational modeling

We validated Compressed Hadamard Imaging using numerical simulations of the optical system and of a dynamic brain-like three-dimensional sample.

3.2.1.1 Simulating the sample.

We simulated a 25 × 25 × 24 μm volume comprised of dynamically fluctuating cells in a foreground volume, plus static intensity cells in a background plane. The foreground volume was discretized into 4 parallel planes at depths $z = 0$, 4, 8, and 12 μm. 24 cells were arranged among these planes, 14 of which changed intensity over time. Each cell was represented by a 2D ellipse with a major axis that was selected uniformly at random between 1.35 μm and 1.65 μm, and a minor axis

selected similarly between 0.9 μm and 1.1 μm, and random in-plane orientation. Cells in the same foreground plane were not allowed to overlap. The background plane was located at $z = 24$ μm, and included 100 static cells, determined as in the foreground planes except that overlaps were allowed. For all cells, the position, intensity, and orientation were randomly determined within predefined ranges. Each plane was sampled on a 64×64 equispaced grid ($\Delta x = \Delta y = 0.40$ μm). Camera images were simulated with the same dimensions and spacing.

Each active cell was assigned a firing pattern, drawn from a shifted exponential distribution of inter-spike intervals with a decay parameter of 2 s and minimum interval of 50 ms. The mean firing rate per cell was thus once per 2.05 s. Each spike drove a uniform increase in cell brightness. The fluorescence timecourse of cell i was computed by convolving the firing times with an exponential response function, of the form $a_i t\, e^{-t/\tau}$ for $t > 0$ with $\tau = 500$ ms. The response amplitude a_i of cell i was selected from a uniform distribution on [0.75,1]. These parameters resulted in dynamic cells with an expected time-averaged intensity of approximately 1/2 of their maximum amplitude.

3.2.1.2 Simulating the optical system.

The microscope was modeled as a space-invariant intensity-linear system comprising an illumination component, which projected patterned illumination onto the sample, and a collection component, which received light and formed an image in the camera. In experiments, the patterns of illumination were created by a digital micromirror device (DMD) which modulated a laser beam. The plane of the DMD was re-imaged onto the focal plane of the microscope.

Illumination and coding patterns: The illumination patterns comprised binary arrays on a rectangular grid with spacing corresponding to the pixel size of the DMD when projected into the focal plane at $z = 0$. In our simulations, which were matched to an experimental apparatus, each DMD pixel projected onto an area of $\approx 0.8\ \mu$m$\times 0.8\ \mu$m. Thus each DMD pixel mapped to 2×2 pixels on the camera plane.

The illumination pattern on each source plane was calculated by performing a discrete convolution between the binary code at $z = 0$ and a 3-dimensional illumination PSF, p_I, corresponding to a Gaussian beam focused at $z = 0$ given by

$$p_I(\vec{r}, z) = I_0 \left(\frac{w_0}{w(z)} \right)^2 \exp\left(\frac{-2|\vec{r}|^2}{w(z)^2} \right), \tag{3.1}$$

where $\vec{r}$ represents a position on the sampled xy-plane, I_0 is the intensity at the center of the beam, set to $2/\pi w_0^2$ to normalize the transversal integral, and

$$w(z) = w_0 \sqrt{1 + \left(\frac{z}{z_R} \right)^2}$$

with $\lambda = 488$ nm and $w_0 = 0.75\ \mu$m. The Rayleigh range is defined as $z_R = \pi\, w_0^2 / \lambda$. For the present example, $z_R = 3.62\ \mu$m.

The fluorescence emitted in each source plane was obtained by a point-wise multiplication between the illumination and the brightness of the cells.

Collection: Images were formed by convolving the emitted fluorescence across all source planes with a 3-dimensional PSF focused at $z = 0$, assumed to be the same as the illumination PSF (**Equation 3.1**).

Confocal simulation: To characterize performance of different dynamic estimation methods, simulated results were compared with a simulated confocal movie. This movie consisted of an instantaneously acquired optical section of the simulated sample at each timepoint, resulting from z-integrating the sample convolved with a 3-dimensional PSF focused at $z = 0$, assumed to be the product of illumination and collection PSFs. The PSFs were assumed to be Gaussian (**Equation 3.1**) with widths set by the combination of diffraction and DMD or camera pixel size, respectively. The calculation in **Appendix B** gives $w_0 = 1.13$ μm for excitation PSF width and 0.77 μm for collection PSF width. This collection PSF is equivalent to setting the confocal pinhole diameter to 1 Airy Unit = $1.21\pi w_0$, corresponding to 2.92 μm at the sample. Confocal simulations were scaled to match the amplitude of reconstructed CHI sections at long code lengths. With this scaling, the mean intensity of raw camera frames in CHI was 11.36 fold larger than the mean intensity of confocal signals, reflecting the fact that CHI removes background computationally while confocal microscopy does so physically.

3.2.1.3 Sampling.

A sequence of N_t camera images was simulated, each with a distinct illumination pattern, from $t = 0$ s to $t = 30$ s. Cell firing patterns were simulated from $t = -8$ s to achieve a steady activity

by $t = 0$ s. The simulations assumed ideal behavior for the DMD (instantaneous switching of patterns) and for the camera (instantaneous acquisition of images). In some simulations we added Poisson shot noise to each pixel, with variance equal to the counts.

3.2.2 Microscope

Imaging experiments used a custom epi-fluorescence microscope equipped with a 488 nm laser (Coherent OBIS) under intensity control by an acousto-optic tunable filter (Gooch and Housego 48058-2.5-.55) and a 640 nm laser (DILAS MB-638.3-8C-T25-SS4.3). Both colors were patterned by a digital micromirror device (VIALUX V-7000), where half of the chip was used to pattern each wavelength, permitting simultaneous independent patterning of both colors. The two patterned beams were focused independently to correct for chromatic aberrations, and then combined via a dichroic beam splitter. The beams were then reflected by a dichroic mirror (Semrock Di01-R405/488/561/635). An astigmatic aberration due to reflection off a warped dichroic was compensated by a cylindrical pair tube lens. Excitation light was focused on the sample from the top by a 20x water-immersion objective (Olympus XLUMPLFLN, NA 1.0), then imaged onto a sCMOS camera (Hamamatsu Orca Flash 4.0). The imaging magnification was 20x, and projection magnification was 28x, resulting in camera and DMD pixel linear dimensions of 325 nm and 493 nm in the sample plane, respectively.

To synchronize illumination and imaging, the DMD was triggered to expose the sample only during the full camera exposure of a limited field of view (FOV), thus avoiding rolling shutter artifacts. For voltage imaging, the camera was set to record a FOV comprising 48 rows at 1 kHz

framerate, allowing 760 μs of full exposure in each frame, over a FOV 15.6 μm along the camera rows. This configuration constrained the illumination time to 76% of the total time. As patterns turned 50% of the pixels on, there was overall 38% time-averaged use of the available laser power. For Ca^{2+} imaging, a FOV with 1264 camera rows was acquired at 100 Hz, with 3.7 ms of illumination exposure time, and illumination efficiency 18%. In both cases, the FOV along the camera columns was not limited by framerate. The camera was configured to run in synchronous acquisition mode and to output a 100 kHz master clock signal which synchronized the rest of the apparatus.

3.2.3 Animal experiments

All animal procedures were conducted following the National Institutes of Health (NIH) guide for the care and use of laboratory animals and approved by the Institutional Animal Care and Use Committee (IACUC) at Harvard University.

3.2.3.1 Brain slice preparation.

A mouse (C57BL/6, Charles River Labs #027) of age P1 was anesthetized in ice for 5 minutes and then transcranially injected with AAV2/9 that codes for a Cre-dependent soma-localized transmembrane Archaerhodopsin-derived voltage indicator and a soma-localized channelrhodopsin (1.1×10^{12} GC/mL). The animal was simultaneously injected with AAV2/9 encoding hSynapsin-Cre to regulate the density of expression of the Cre-dependent construct (8.4×10^{9} GC/mL, Massachusetts Eye and Ear Infirmary Virus Core).

At age P40 the animal was anesthetized by isoflurane inhalation, then transcardially perfused with ice-cold slicing solution containing (in mM): 110 choline chloride, 25 $NaHCO_3$, 2.5 KCl, 7 $MgCl_2$, 0.5 $CaCl_2$, 1.25 NaH_2PO_4, 25 glucose, 11.6 ascorbic acid, and 3.1 pyruvic acid (310 mOsm/kg). The brain was cut into 300 μm thickness slices using a vibratome (Leica VT1200S) and transferred to an artificial cerebrospinal fluid (aCSF) bath containing (in mM): 125 NaCl, 2.5 KCl, 25 $NaHCO_3$, 2 $CaCl_2$, 1 $MgCl_2$, 1.25 NaH_2PO_4, 25 glucose (295 mOsm/kg), initially warmed for 45 min at 34 $^\circ$C, then at room temperature, and perfused at 1 mL/min during imaging experiments. Solutions were continuously bubbled with carbogen (95% O_2 and 5% CO_2).

3.2.3.2 Zebrafish preparation.

Zebrafish expressing cytosolic GCaMP6f under a neuronal promoter were used (a gift from Florian Engert, Tg(elavl3:GCaMP6f)^{jf1} [160]). At day 4 post fertilization a fish was immersed for 10 min in a 1 mg/mL solution of α-bungarotoxin (Life technologies B1601) to paralyze it, then embedded in 1.5% low melting point agarose in the 10 mm well of a glass-bottom 35 mm cell culture dish. The animal was incubated for 45 min in 75 mM pentylenetetrazole (PTZ, Sigma P6500) to induce seizure-like brain activity immediately prior to imaging.

3.2.4 Illumination patterns

Series of Hadamard-coded patterns were designed to illuminate neighboring sample locations with orthogonal time-sequences of intensity. Let $\boldsymbol{H}$ denote a Hadamard matrix of size m with elements in $\{-1, 1\}$ satisfying $\boldsymbol{H}^T \boldsymbol{H} = m \boldsymbol{I}_m$, where $\boldsymbol{I}_m$ is the identity of size m, and having

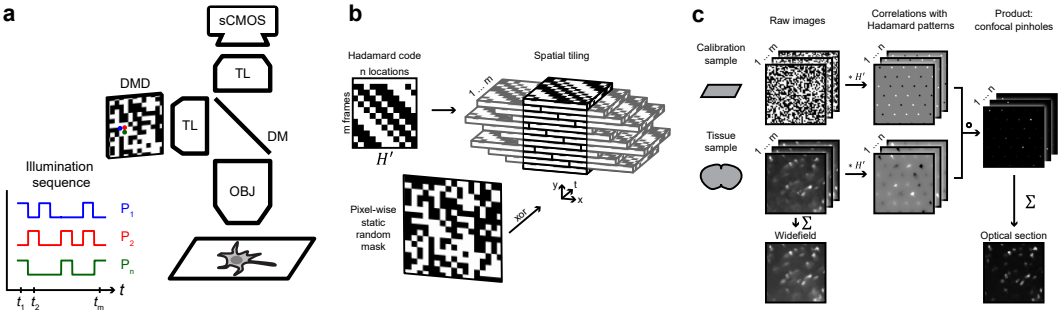

Figure 3.1: Hadamard optical sectioning microscopy. (a) A microscope projects orthogonal functions of illumination vs. time in neighboring regions of the sample. Light is modulated by a DMD and measured with a Camera. **(b)** Hadamard codes are tiled to fill the image FOV, and a random binary mask inverts 50% of pixels to reduce crosstalk between repeated code locations. **(c)** Raw images from a tissue sample are demodulated by matched filtering with raw data from a calibration sample. Filtered correlation maps are summed to form an optical section. Raw tissue data are summed to obtain a widefield image.

ones in the first column and first row. The illumination P_{ij} of sequence i at time-step j was defined as $P_{ij} = (H'_{ij} + 1)/2$, where $\boldsymbol{H}'$ is the matrix formed by the last $m - 1$ columns of $\boldsymbol{H}$. Orthogonality between illumination codes is verified by $\boldsymbol{P}^T \boldsymbol{H}' = (m/2)\, \boldsymbol{I}_{m-1}$. These codes were tiled spatially, assigning code $k_{ij} \in \{1, ..., m-1\}$ to the projector pixel (i, j) with $k_{ij} = \mathrm{mod}(i \cdot q + j, m-1) + 1$, where q was an offset parameter to maximize the spatial separation of repeating codes. To further reduce spurious crosstalk between repeating codes, a random binary mask B inverted the polarity of 50% of projected pixels. Ca^{2+} activity was measured setting $m = 36$ and $q = 10$, while voltage recordings used $m = 20$ and $q = 5$. This process is depicted in **Figure 3.1b**.

3.2.5 Hadamard demodulation

Hadamard microscopy typically entails a tradeoff between quality of optical sectioning (requiring more illumination patterns) and temporal resolution (requiring fewer illumination patterns). First we review briefly the image reconstruction algorithm for Hadamard microscopy, then we show how to relax this tradeoff by taking advantage of the low-rank statistical structure of the underlying signals.

In Hadamard microscopy, one first acquires a set of calibration images $\boldsymbol{C}$ by projecting the illumination patterns onto a flat and homogeneous fluorescent film (often a coverslip with a stripe of fluorescent highlighter ink). Throughout this document, a video sequence of L frames will be represented as a matrix in which each column is a vectorized video frame, as $\boldsymbol{C} = [\boldsymbol{c}^1 \dots \boldsymbol{c}^L]$. In this case, $\boldsymbol{c}^p$ denotes the video frame corresponding to the p-th Hadamard calibration pattern. One then repeats the acquisition procedure on the real sample. Let $\boldsymbol{X} = [\boldsymbol{x}^1 \dots \boldsymbol{x}^L]$ denote the resulting raw camera video. For the moment, we assume that both $\boldsymbol{C}$ and $\boldsymbol{X}$ have length L, equal to one repetition of the Hadamard code. The algorithm to compute a Hadamard optical section is:

$$\boldsymbol{x}^S := \sum_{p=1}^{L} \delta \boldsymbol{c}^p \odot \boldsymbol{x}^p$$

where $\delta \boldsymbol{c}^p = \boldsymbol{c}^p - \langle \boldsymbol{C} \rangle_L$ represents the deviation of each pixel from its average over all frames, and $\odot$ represents the entry-wise product between two arrays. This process is depicted in **Figure 3.1c**.

Multiple sets of L images can be concatenated to construct an optically sectioned movie, albeit with a frame rate L-fold slower than the raw video.

3.2.6 Theory of dynamic optical sectioning

Our objective is to devise a practical optical sectioning procedure that matches the performance of an idealized procedure that we now describe. Suppose we had access through an oracle to a set of coded video sequences $\boldsymbol{X}^p$ for all p, i.e. at each time t we had access to images of the sample illuminated by all L different Hadamard patterns. In this case we could perform optical sectioning at the full frame rate by using the Hadamard image reconstruction algorithm described above for each time t.

This idealized method suggests an approach to attaining similar performance with physically attainable data. From a given recording $\boldsymbol{X}$, we seek to estimate all video sequences $\boldsymbol{X}^p$ where the sample has been illuminated with a fixed pattern across all frames. If we can perform this estimate for each p then we can reconstruct the high time-resolution optically sectioned movie.

Let $\boldsymbol{X}^w$ be the movie that would have been acquired with homogeneous wide-field illumination, i.e. conventional epifluorescence. The key assumption is that if $\boldsymbol{X}^w$ is approximately low-rank, then the temporal components of the factorized $\boldsymbol{X}^w$ are good approximations of the temporal components of each $\boldsymbol{X}^p$. In the following two sections we discuss: (i) how to estimate the constant-pattern data $\boldsymbol{X}^p$ from the wide-field data $\boldsymbol{X}^w$; and (ii) how to estimate the wide-field video $\boldsymbol{X}^w$ from data acquired with patterned illumination.

3.2.7 The relation between widefield and constant-pattern data.

We can always decompose the wide-field data $\boldsymbol{X}^w$ as a superposition of rank-1 video sequences by SVD:

$$\boldsymbol{X}^w = \boldsymbol{U}^w \boldsymbol{V}^{wT} = \sum_i \boldsymbol{u}_i^w \otimes \boldsymbol{v}_i^w \tag{3.2}$$

Here $\otimes$ represents the outer product, and ^{T} denotes transpose. For our simulated data $\boldsymbol{u}_i^w$ is a vector representation of a 64 × 64 image and $\boldsymbol{v}_i^w$ is a T × 1 time modulation vector, where T is the number of frames. We assume the set $\{\boldsymbol{u}_i^w\}$ is orthonormal. We can consider the same decomposition for each hypothetical movie $\boldsymbol{X}^p$ where all frames are illuminated with the same single pattern $\boldsymbol{p}$:

$$\boldsymbol{X}^p = \boldsymbol{U}^p \boldsymbol{V}^{pT} = \sum_i \boldsymbol{u}_i^p \otimes \boldsymbol{v}_i^p.$$

We propose the following model for the relation between the spatial and temporal components of each decomposition. If there is only one term in **Equation 3.2** then it must be the case that the decomposition for each $\boldsymbol{X}^p$ has only one term: the effect of projecting a constant pattern onto a sample can certainly reduce the rank, but not increase it. In this case, it is reasonable that the temporal dynamics will be the same under either homogeneous or patterned illumination, i.e. that $\boldsymbol{v}_1^p = \boldsymbol{v}_1^w$, provided that a representative portion of the dynamic object is still illuminated.

Our key assumption is that this relation holds even when the video sequences have more than one component, and thus $\boldsymbol{v}_i^p = \boldsymbol{v}_i^w$ for every component i of the movie and illumination pattern

p. Under this assumption,

$$\boldsymbol{X}^p = \boldsymbol{U}^p \boldsymbol{V}^{wT} = \sum_i \boldsymbol{u}_i^p \otimes \boldsymbol{v}_i^w, \tag{3.3}$$

and if $\boldsymbol{V}^w$ is known, estimating $\boldsymbol{X}^p$ reduces to estimating $\boldsymbol{U}^p$.

3.2.8 Dynamic optical sectioning from widefield data and coded illumination patterns

Let $\boldsymbol{Y}$ be a video sequence where L coded illumination patterns have been used and repeated R times, and suppose first we also have access through an oracle to the wide-field data $\boldsymbol{X}^w$. Since each p-th coding pattern is repeated R times, we have observed exactly R frames of the sequence $\boldsymbol{X}^p$. Therefore, the coded illumination data provides us with *incomplete* information about each $\boldsymbol{X}^p$. In **Figure 3.2**, $\boldsymbol{Y}$ is represented as the structured illumination measured data, $\boldsymbol{X}^w$ is represented as paired frame widefield, and $\boldsymbol{X}^p$ is represented as estimated constant pattern data.

By our key assumption, if we have access to the wide-field sequence $\boldsymbol{X}^w$ we also know the dynamic components of each $\boldsymbol{X}^p$. This leads us to an estimation problem. Let T_p be the set of sampled times at which the p-th pattern has been projected; each one of such sets has exactly R elements. To simplify the notation, let $\boldsymbol{m}_t^w$ be the t-th *row* of the matrix $\boldsymbol{V}^w$. This allows us to write the consistency constraint

$$t \in T_p \quad \Longrightarrow \quad \boldsymbol{y}_t = \boldsymbol{x}_t^p = \boldsymbol{U}^p \boldsymbol{m}_t^w. \tag{3.4}$$

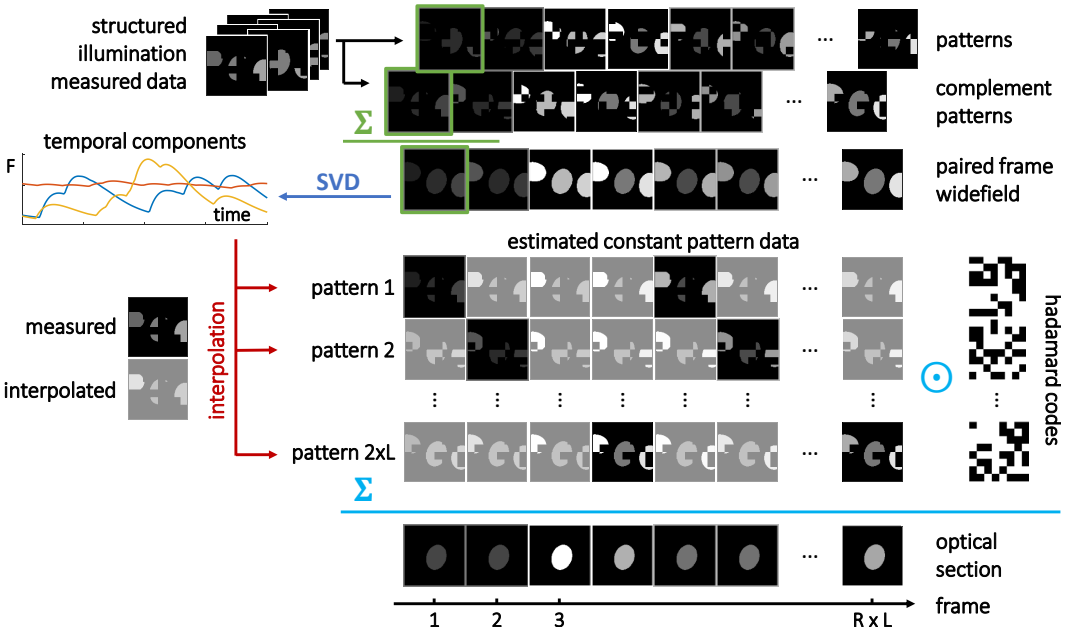

Figure 3.2: Estimation of optical section dynamics from compressed Hadamard measurements. Green: Pairs of images acquired with complement illumination patterns are summed to form a half-framerate widefield movie. **Blue:** Low rank temporal components are calculated using singular value decomposition (SVD). **Red:** Missing frames in constant-pattern movies are interpolated from measured patterns and temporal evolution of components. **Cyan:** Hadamard demodulation of estimated patterned frames results in a dynamic optical section.

We propose to estimate the matrix $\boldsymbol{U}^p$ by solving

$$\text{minimize} \quad \sum_{t \in T_p} \|\boldsymbol{y}_t - \boldsymbol{U}^p \boldsymbol{m}_t^w\|_F^2 \tag{3.5}$$

where $\|\cdot\|_F^2$ denotes the Frobenius norm squared, i.e., the sum of the squared entries of its argument. In the above, we assume we are trying to find as many components as there are present in the widefield data. In this case, as long as the number of repetitions of the patterns is larger than the number of components we are solving for, the solution is unique. The first-order optimality condition characterizes the optimal solution $\widehat{\boldsymbol{U}}^p$ as the solution to

$$\widehat{\boldsymbol{U}}^p \sum_{t \in T_p} \boldsymbol{m}_t^w \otimes \boldsymbol{m}_t^w = \sum_{t \in T_p} \boldsymbol{y}_t \otimes \boldsymbol{m}_t^w, \tag{3.6}$$

from where it is clear the solution is unique as long as the second factor in the left-hand side is non-singular; this is generically true if the number R of repetitions is at least the number of components of the widefield sequence. If one can cleanly divide the movie into non-overlapping spatial domains with independent dynamics, then each domain can be analyzed separately. In this case R must only exceed the rank of the domain with the largest number of components. We define the estimate for $\boldsymbol{X}^p$ as

$$\widehat{\boldsymbol{X}}^p = \widehat{\boldsymbol{U}}^p \boldsymbol{V}^{wT}.$$

This allows us to calculate a Hadamard optical section for time t as

$$\begin{aligned}\widehat{\boldsymbol{x}}_t^S &= \sum_{p=1}^{L} \partial \boldsymbol{c}^p \odot \widehat{\boldsymbol{x}}_t^p \\ &= \sum_{p=1}^{L} \partial \boldsymbol{c}^p \odot (\widehat{\boldsymbol{U}}^p \boldsymbol{m}_t^w) \\ &= \sum_i \left(\sum_{p=1}^{L} \partial \boldsymbol{c}^p \odot \widehat{\boldsymbol{u}}_i^p \right) \otimes \boldsymbol{v}_i^w.\end{aligned}$$

Consequently, our estimate of the optically sectioned movie $\widehat{\boldsymbol{X}}^p$ corresponds to the static Hadamard demodulation of the estimated spatial components, time-modulated by the temporal components of the widefield data.

3.2.9 Estimating widefield data from coded illumination patterns

The construction of our estimated optical section relies on the computation of the right-singular vectors of $\boldsymbol{X}^w$. As we cannot *both* acquire a structured illumination sequence and a uniform illumination sequence simultaneously, we designed illumination patterns to overcome this problem. At the cost of reducing the dynamic reconstruction frame-rate by a factor of two, a complement-interleaved sequence of patterns enabled estimation of the widefield sequence *and* the dynamic Hadamard optical section, as follows.

Consider the video sequence where L coded illumination patterns have been used and repeated R times. We interleave the acquisition of each pattern with the acquisition of its complement, i.e. the binary pattern obtained by inverting each entry. Adding both patterns yields a uniform

illumination pattern, i.e.

$$\hat{\boldsymbol{x}}_t^w = \boldsymbol{y}_t + \overline{\boldsymbol{y}}_{t+\delta t} \tag{3.7}$$

where $\boldsymbol{y}_t$ is the data image acquired at time t and $\overline{\boldsymbol{y}}_{t+\delta t}$ is the data image acquired one camera frame later, with the complementary illumination pattern.

We can now estimate the temporal components of the widefield sequence, which we denote as $\widehat{\boldsymbol{V}}^w$; similarly, we let $\widehat{\boldsymbol{m}}_t^w$ be the estimate for $\boldsymbol{m}_t^w$. The dynamic Hadamard optical section becomes

$$\hat{\boldsymbol{x}}_t^S = \sum_i \left(\sum_{p=1}^{L} \delta \boldsymbol{c}_p \odot \widehat{\boldsymbol{u}}_i^p \right) \otimes \hat{\boldsymbol{v}}_i^w$$

where $\widehat{\boldsymbol{U}}^p$ is now computed from **Equation 3.6** by replacing $\boldsymbol{m}_t^w$ by its estimate $\widehat{\boldsymbol{m}}_t^w$.

In our implementation we found small fluctuations in illumination that varied with the same period as the sequence of illumination patterns, a consequence of an un-identified instrumentation artifact. To correct this artifact, the widefield estimated movies were digitally divided by an estimate of the intensity variations.

3.2.10 Pseudocode

A pseudocode of the data analysis method is shown in **Algorithm 3.1**. The computational complexity not including the computation of the SVD is $O\ (N \times R \times L \times P)$ where N is the number of SVD components, and P the number of camera pixels. MATLAB source code that generates **Figure 3.4b** from raw data is available at

https://github.com/adamcohenlab/Compressed-Hadamard-Code

Algorithm 3.1 Compressed Hadamard estimation

parameters:
N ▷ number of components for truncated SVD
inputs:
$\boldsymbol{M}$ ▷ tissue activity movie with $R \times 2 \times L$ patterned frames
$\boldsymbol{C}$ ▷ calibration movie with $2 \times L$ patterned frames
initialization:
map $\leftarrow [1, 2, 3, ..., 2 \times L, 1, 2, 3, ...]$ ▷ pattern order in $\boldsymbol{M}$
procedure CHI($\boldsymbol{M}, \boldsymbol{C}$)
$\boldsymbol{M}^w \leftarrow \boldsymbol{M}_{\text{even}} + \boldsymbol{M}_{\text{odd}}$
$\boldsymbol{C}^\partial \leftarrow \boldsymbol{C}_{\text{even}} - \boldsymbol{C}_{\text{odd}}$
$\boldsymbol{U}, \boldsymbol{S}, \boldsymbol{V} \leftarrow \text{SVD}(\boldsymbol{M}^w, N)$ ▷ $\boldsymbol{U}\boldsymbol{S}\boldsymbol{V}^T$ approximates $\boldsymbol{M}^w$ with rank N
$\boldsymbol{M}^r \leftarrow \boldsymbol{M}^w$
for $i \leftarrow 1$ to N **do**
$\boldsymbol{v} \leftarrow \boldsymbol{S}_{i,i}\boldsymbol{V}_i$
for $j \leftarrow 1$ to $2 \times L$ **do**
$\widehat{\boldsymbol{U}}^p_j \leftarrow \sum_{k \in \text{map}=j} \boldsymbol{M}^r_k \boldsymbol{v}_k \,/\, \sum_{k \in \text{map}=j} \boldsymbol{v}_k^2$ ▷ estimation
end for
$\widehat{\boldsymbol{U}}^w_i \leftarrow \sum_{k=1}^{2\times L} \widehat{\boldsymbol{U}}^p_k$
$\widehat{\boldsymbol{U}}^{p\partial} \leftarrow \widehat{\boldsymbol{U}}^p_{\text{even}} - \widehat{\boldsymbol{U}}^p_{\text{odd}}$
$\widehat{\boldsymbol{U}}^H_i \leftarrow \sum_{k=1}^{L} \widehat{\boldsymbol{U}}^{p\partial}_k \odot \boldsymbol{C}^\partial_k$ ▷ Hadamard demodulation
$\boldsymbol{M}^r \leftarrow \boldsymbol{M}^r - \widehat{\boldsymbol{U}}^p_{\text{map}} \boldsymbol{v}^T$ ▷ remove estimated component from residual
end for
end procedure
outputs:
$\widehat{\boldsymbol{M}}^w \leftarrow \widehat{\boldsymbol{U}}^w \boldsymbol{S}\boldsymbol{V}^T$ ▷ widefield movie
$\widehat{\boldsymbol{M}}^H \leftarrow \widehat{\boldsymbol{U}}^H \boldsymbol{S}\boldsymbol{V}^T$ ▷ optical section movie

3.2.11 Robustness

Accurate estimation of the spatial components relies on being able to: (i) estimate accurately the widefield sequence; and (ii) compute the time-modulation factors according to the rank of the sequence. Several factors may impact either step. For instance, the changes in sample intensity might be too fast relative to the rate at which the interleaved complementary patterns are illuminated, leading to an inaccurate estimate of the widefield sequence. Even if the widefield sequence is estimated accurately, its rank could be too high relative to the number of repetitions, and therefore the number of time-modulation factors might be underestimated.

This section addresses the variability of the proposed estimate for $\boldsymbol{U}^p$ with respect to these two factors. Suppose the widefield sequence $\boldsymbol{X}^w$ has a rank N_w, which we do not assume to be small, and consider a rank $\widehat{N}_w$ estimate $\widehat{\boldsymbol{X}}^w$ of $\boldsymbol{X}^w$ with $\widehat{N}_w \leq N_w$. Furthermore, assume the number of repetitions to be greater than the number of components to be estimated ($\widehat{N}_w \leq R$). As indicated before, this makes the estimate uniquely defined. In movies with e.g. a modest number of neurons, this is often the case. If the sources are compact and one can divide the movie into sub-regions each with a modest number of sources, one can then decrease the requirement on R in each sub-region.

In this setting $\boldsymbol{U}^p$ has N_w columns and each $\boldsymbol{m}_t^w$ has N_w entries. We can decompose their product as

$$\boldsymbol{U}^p \boldsymbol{m}_t^w = \begin{bmatrix} \boldsymbol{U}_0^p & \boldsymbol{U}_R^p \end{bmatrix} \begin{bmatrix} \boldsymbol{m}_{0,t}^w \\ \\ \boldsymbol{m}_{R,t}^w \end{bmatrix} = \boldsymbol{U}_0^p \boldsymbol{m}_{0,t}^w + \boldsymbol{U}_R^p \boldsymbol{m}_{R,t}^w,$$

where $\boldsymbol{U}_0^p$ has now $\widehat{N}_w$ columns and $\boldsymbol{m}_{0,t}^w$ has $\widehat{N}_w$ entries. In this decomposition, $\boldsymbol{U}_0^p$ represents the $\widehat{N}_w$ components that we ought to estimate accurately, whereas $\boldsymbol{U}_R^p$ represents the remaining $N_w - \widehat{N}_w \geq 0$ components that we are neglecting. From **Equation 3.6** we see that $\widehat{\boldsymbol{U}}^p$ is determined by

$$\begin{aligned}
\widehat{\boldsymbol{U}}^p \sum\nolimits_{t\in T_p} \widehat{\boldsymbol{m}}_t^w \otimes \widehat{\boldsymbol{m}}_t^w &= \sum\nolimits_{t\in T_p} \boldsymbol{y}_t^w \otimes \widehat{\boldsymbol{m}}_t^w \\
&= \sum\nolimits_{t\in T_p} (\boldsymbol{U}^p \boldsymbol{m}_t^w) \otimes \widehat{\boldsymbol{m}}_t^w \\
&= \boldsymbol{U}_0^p \sum\nolimits_{t\in T_p} \boldsymbol{m}_{0,t}^w \otimes \widehat{\boldsymbol{m}}_t^w + \boldsymbol{U}_R^p \sum\nolimits_{t\in T_p} \boldsymbol{m}_{R,t}^w \otimes \widehat{\boldsymbol{m}}_t^w.
\end{aligned}$$

A straightforward algebraic manipulation shows that

$$\begin{aligned}
\left(\widehat{\boldsymbol{U}}^p - \boldsymbol{U}_0^p\right) \sum\nolimits_{t\in T_p} \widehat{\boldsymbol{m}}_t^w \otimes \widehat{\boldsymbol{m}}_t^w &= \boldsymbol{U}_R^p \sum\nolimits_{t\in T_p} \boldsymbol{m}_{R,t}^w \otimes \widehat{\boldsymbol{m}}_t^w \\
&\quad + \boldsymbol{U}_0^p \sum\nolimits_{t\in T_p} (\boldsymbol{m}_{0,t}^w - \widehat{\boldsymbol{m}}_t^w) \otimes \widehat{\boldsymbol{m}}_t^w
\end{aligned}$$

Consequently, when the second factor in the left-hand side is well-conditioned, the error $\widehat{\boldsymbol{U}}^p$ incurs in estimating $\boldsymbol{U}_0^p$ is essentially controlled by two dependent factors: (i) the decay in the singular values of the widefield sequence $\boldsymbol{X}^w$ as quantified by the size of the modulation factors $\boldsymbol{m}_{R,t}^w$ for the components we are *not* estimating; and (ii) the accuracy in the estimate of the modulation factors $\boldsymbol{m}_{0,t}^w$ for the components we are estimating.

This analysis shows that our approach to estimating $\boldsymbol{X}^w$ should be evaluated according to these criteria. The first criterion depends on the properties of the sample being imaged, namely the

activity of the cells during the observation and the number of cells active in the field of view at any given time. It thus depends on the specifics of the experimental setup. The second criterion can be analyzed as follows. If we let $\overline{\boldsymbol{U}}^p$ be the components corresponding to the inverted p-th pattern and the p-th pattern is illuminated at time t, the estimate in **Equation 3.7** implies

$$\begin{aligned}\hat{\boldsymbol{x}}_t^w &= (\boldsymbol{U}^p + \overline{\boldsymbol{U}}^p)\boldsymbol{m}_t^w + \overline{\boldsymbol{U}}^p(\boldsymbol{m}_{t+\delta t}^w - \boldsymbol{m}_t^w) \\ &\approx \boldsymbol{x}_t^w + \overline{\boldsymbol{U}}^p(\boldsymbol{m}_{t+\delta t}^w - \boldsymbol{m}_t^w)\end{aligned}$$

where we consider that $\boldsymbol{U}^p + \overline{\boldsymbol{U}}^p \approx \boldsymbol{U}^w$. Consequently, the error when estimating the components of the widefield sequence will be mostly due to the rate of change of the temporal components, which depends on the rate at which each cell in the sample activates. Dynamics faster than the temporal resolution (half the camera frame rate) will not be accurately captured by the proposed method. Large variations of fluorescence between the instants when the sample is illuminated by a given pattern and by its complement will give rise to artifacts. In the estimated widefield movie, a spatial artifact corresponding to the momentary illumination pattern will arise. This effect is formalized in **Appendix C**.

3.3 Results

3.3.1 Numerical experiments

We simulated movies of a dynamic 3-dimensional sample, approximately matched to brain tissue expressing a nuclear-localized Ca^{2+} indicator. This process is illustrated in **Figure 3.3a**, left panel.

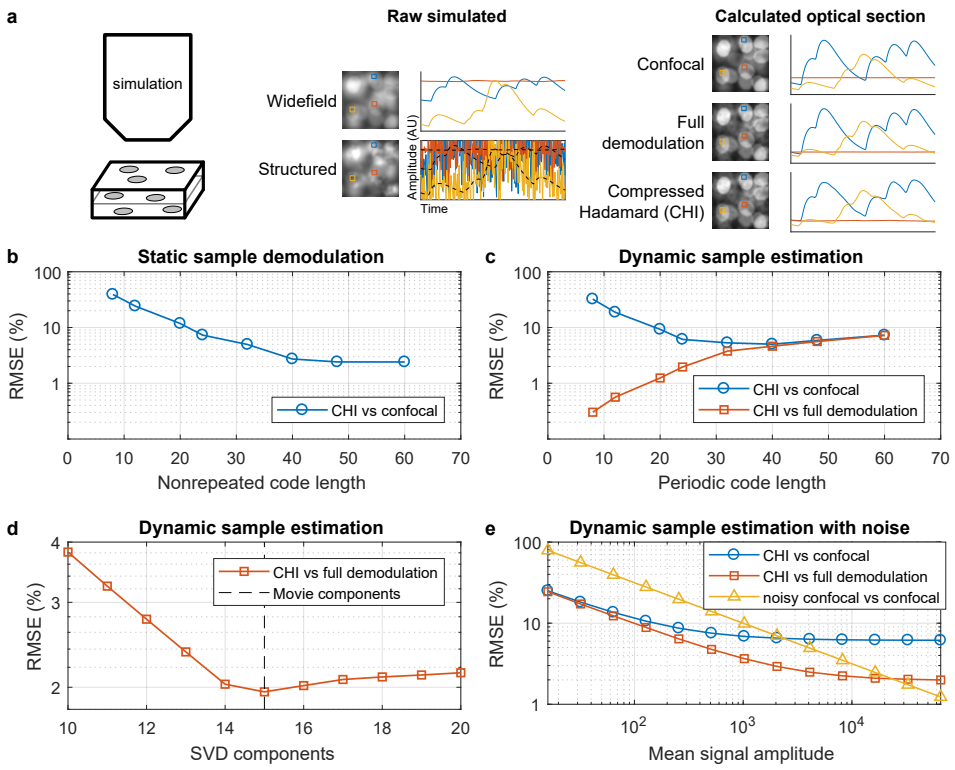

Figure 3.3: Dynamic optical sectioning in simulated data. (a) Left: Simulations modeled a 3-dimensional sample of neuronal activation under patterned illumination. Center: simulated datasets used in calculation. The fluctuations in the 'Structured' traces represent the effect of modulated illumination. Right: Optical section datasets computed by different methods. 'Confocal' is an idealized instantaneously acquired confocal image. 'Full demodulation' is an idealized Hadamard section in which images with all illumination patterns are known for each frame. 'Compressed Hadamard' represents a physically realizable approach in which one illumination pattern is used per frame, and the missing data are inferred (CHI). **(b)** In a static sample, increasing the Hadamard code length increased the size of the spatial tiles, and reduced systematic error due to tile-to-tile crosstalk. **(c)** In a dynamic sample with a fixed number of frames (enforcing a tradeoff between code length L and number of repeats R), short codes introduced errors into Hadamard reconstructions due to tile-to-tile crosstalk. Long codes had less tile-to-tile crosstalk, but fewer repetitions, R, leading CHI to suffer relative to 'full demodulation'. **(d)** For a fixed code length, the CHI error relative to full demodulation was minimized when the number of SVD components used (e.g. in **Equation 3.2**) was equal to the rank of the data. **(e)** CHI reconstructions encountered a shot noise limited regime at low counts under Poisson noise (where error is inversely proportional to square root of intensity), but at higher counts errors approached the level of systematic errors present in the noiseless case. The shot noise limited error in CHI was ~3-fold smaller than in confocal when signal levels were matched. The two techniques were comparable when raw photon counts were matched.

For each set of sample dynamics, we simulated several different imaging modalities. 1) spatially uniform illumination and wide-field imaging onto a camera ($\boldsymbol{X}^w$); 2) patterned illumination and widefield imaging ($\boldsymbol{Y}$); 3) instantaneous confocal acquisition of the whole FOV; 4) a hypothetical set of movies where each illumination pattern was acquired for all frames ($\boldsymbol{X}^p$); and 5) a calibration pattern dataset ($\boldsymbol{C}$) that simulated projection on a thin constant fluorescent layer in the focal plane. **Figure 3.3a** shows calculations of input datasets in the center panel, and resulting optical sections in the right panel. These experiments investigate how the proposed method is affected by measurement noise, and by parameter choices in the code length, the number of repetitions of periodic codes, and the number of SVD components.

To first characterize the static Hadamard demodulation method, we simulated the ideal (noiseless) acquisition of a static sample using different lengths of Hadamard code. Ideal Hadamard demodulation results in a confocal-like optical section. However our simulation represented two non-ideal aspects of practical Hadamard microscopy: 1) codes were repeated to tile the FOV, introducing crosstalk between spatial repetitions of the same code; 2) the calibration method measured the illumination pattern convolved with the collection PSF, whereas one would ideally measure the illumination pattern at the sample itself. Errors were calculated as the root mean squared deviations for all pixels and all timepoints, normalized by the mean of the reference movie. As anticipated, for a time-invariant sample, increasing Hadamard code length led to improved correspondence of Hadamard demodulation and simulated confocal (**Figure 3.3b**).

We then tested the dynamic estimation method with simulated movies of time-varying samples. For a desired length of experiment, camera framerate, and total number of pictures, one

could choose more repetitions of a short code, or fewer repetitions of a long code. To characterize this tradeoff, we simulated an ideal (noiseless) movie for a range of Hadamard code lengths (8, 12, 20, 24, 32, 40, 48, and 60), using periodic repetitions of the complement-interleaved pattern sequence (60, 40, 24, 20, 15, 12, 10, and 8 repetitions respectively) for a total of 960 frames in all cases. Estimated CHI optically sectioned movies ($\widehat{\boldsymbol{X}}^S$) were compared to confocal images (accounting for the confocal point-spread function, but assuming instantaneous image acquisition across the whole field of view) and to 'full demodulation' Hadamard optical section movies ($\boldsymbol{X}^S$, calculated by demodulating the full set $\boldsymbol{X}^p$ for each t, i.e. assuming that images with all Hadamard illumination patterns were available at each time-point).

Figure 3.3c shows the discrepancy between CHI vs. the confocal simulations (blue circles), indicating an intermediate value of code length as optimal. The comparison of CHI with 'full demodulation' Hadamard showed the reconstruction error due to the dynamic estimation process, while avoiding confusion with systematic errors (relative to confocal) that were present in both Hadamard demodulation processes, i.e. from tile-to-tile optical crosstalk. **Figure 3.3c** (red squares) shows that the dynamic estimation error increased with code length, as the number of code repetitions decreased. We ascribe this effect to rank under-representation at longer code lengths. The dynamic estimation error was less than 2% for code length 24, the longest code length for which the simulated sample rank (15) was over-represented by the number of code repetitions (20).

CHI uses the singular value decomposition (SVD) to represent movie dynamics. To characterize the effect of the number of SVD components, we applied CHI with code length 24 (corre-

sponding to $R = 20$ replicates) to a simulated movie with 15 components. We calculated reconstruction error as a function of number of SVD components. The error, shown in **Figure 3.3d**, was minimized when using the same number of components as in the data, but did not suffer very much from using more than the ideal number of SVD components.

To test the effect of shot noise on CHI reconstructions, we simulated camera movies with mean counts per pixel ranging from ~1 to 5×10^4 and imposed Poisson-distributed noise. We used CHI to estimate optically sectioned movies, and compared with noiseless confocal and noiseless 'full demodulation' Hadamard movies (**Figure 3.3e**). Two noise regimes were apparent. At low counts, shot noise dominated and error was inversely proportional to the square root of the signal amplitude. At high counts, the noise asymptotically approached the level of the noiseless case. No instabilities or numerical artifacts were observed in estimates from noisy datasets.

To benchmark the photon economy of CHI reconstructions, we compared CHI and confocal when both were subject to Poisson-distributed shot noise. The two sets of images were scaled to have the same mean counts, and the error in each was calculated relative to a noiseless confocal dataset. As expected, the confocal shot noise error was inversely proportional to the square root of mean counts. At low intensity, the confocal error was larger than the CHI error by a factor of 3.28. This discrepancy reflects the 11.36-fold greater mean counts in the raw CHI frames ($\sqrt{11.36} = 3.37$), i.e. the two techniques have comparable shot noise properties when raw photon counts are matched. We attribute the favorable noise properties of CHI to the denoising properties of the SVD truncation step, which has been characterized previously[161,162]. In general, the noise properties of CHI will depend on the amount of background autofluorescence

(the image reconstruction process removes this background on average, but not its shot noise), whereas the noise properties of confocal are insensitive to the background because background is rejected physically before photon detection. Practical implementations of camera-based spinning disk and point-scanning confocal systems can produce optical sections with minimal noise from background fluorescence. Spinning disk confocal can readily image at a 1 kHz camera frame-rate, while point-scanning is typically slower due to limitations on galvo mirror acceleration. However neither spinning disk nor point-scanning confocal techniques readily extend to high *NA* large FOV optics, as further elaborated in **Section 3.4**.

3.3.2 Compressed Hadamard Imaging in live tissue

All-optical electrophysiology in acute brain slice. We tested Compressed Hadamard Imaging in acute mouse brain slice. A sparse subset of neurons co-expressed a blue-excited optogenetic actuator and a red-excited genetically encoded voltage indicator. Targeted blue light stimulation evoked action potentials (APs), which registered via the fluorescence of the voltage indicator (**Figure 3.4a**, left). Similar preparations have previously been used for high-throughoupt all-optical mapping of neuronal excitability in intact brain tissue[163]. Data acquisition at 1 kHz framerate allowed activity reconstructions at 500 Hz. This experiment used a Hadamard code length of 20 patterns in complement-interleaved sequence, repeated 240 times over 9.6 s.

We tested the ability of CHI to register the short fluorescence transients associated with APs. The blue stimulation pattern consisted of 500 ms on every 1 s, increasing in intensity from 10 to 40 mW/cm^2. To reconstruct images, each acquisition was analyzed with the same algorithm,

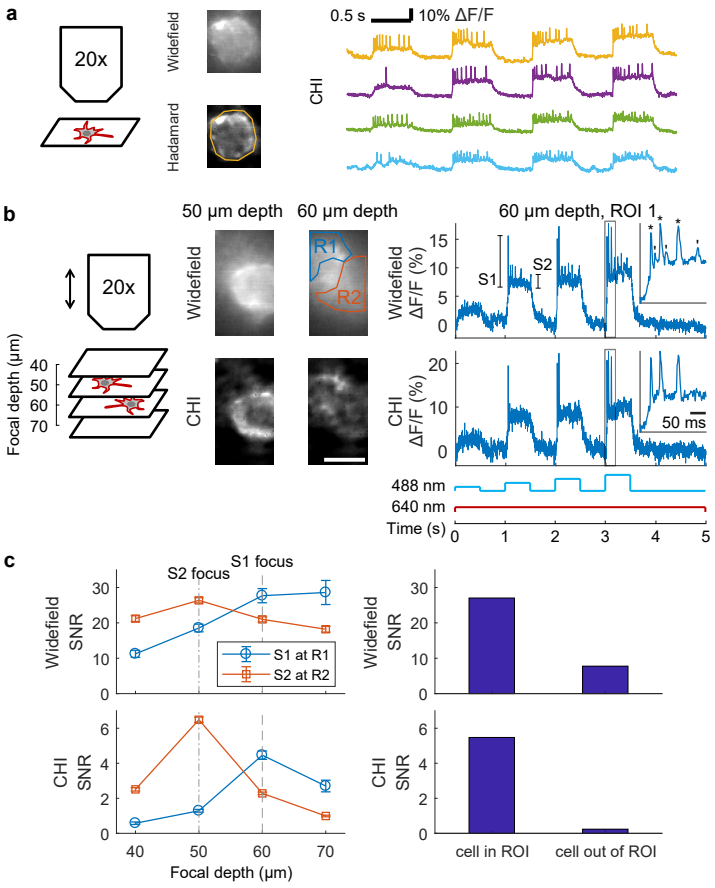

Figure 3.4: (Compressed Hadamard Imaging of high-speed neuronal voltage dynamics in brain tissue. CHI optical sections were computed at a 500 Hz reconstructed frame rate in acute mouse brain slices expressing an Optopatch construct. **(a)** Example single-neuron recordings showing optically evoked and optically recorded action potentials. The CHI cell images showed increased membrane contrast and background suppression relative to wide-field images. The first 2 traces come from the cell and ROI in the image. The last 2 come from another cell. **(b)** Two partially overlapping neurons (S1 and S2) were recorded in the same FOV, and the measurement repeated at multiple depths. Scale bar 10 μm. Two ROIs (R1 and R2) reported mixed signals from both neurons in the wide-field images. The same ROIs reported single-cell spike patterns in the CHI images. **(c)** Quantification of action potential SNR as a function of focal plane depth. Left, top: in wide-field recordings, both cells contributed to the spikes in both ROIs at all focal depts. In CHI, the signal from each cell was localized around the corresponding focal plane. Error bars represent s.e.m. Right: Hadamard removed spurious signals from out-of-focus cells, increasing the signal contrast. Maximum SNR was reduced by a factor of ~5 in CHI sections compared to the widefield reference.

selecting 5 components for the SVD. This procedure yielded estimates of the widefield epifluorescence movie and Hadamard optical section. **Figure 3.4a** (center panel) shows time-averaged images of an example movie reconstructed in Widefield (top) and CHI (bottom), showing an increased membrane contrast and background rejection in the CHI optical section; the right panel shows time traces integrated from a cell mask ROI in multiple CHI movies. Slow transients uncorrelated with optogenetic stimulation were attributed to sub-threshold potential fluctuations.

To test the ability to reject out-of-focus signals, we studied two nearby, partially overlapping neurons, located at 50 and 60 μm below the tissue surface. We repeated the stimulation and imaging protocol while translating the objective z position to focus at different depths (z = 40, 50, 60 and 70 μm below the tissue surface, left panel of **Figure 3.4b**). Widefield and Hadamard movies were reconstructed at 500 Hz from each recording. **Figure 3.4b** shows in the center panel time averaged images at the depths focused on each neuron soma. CHI images showed reduced background fluorescence and higher cell membrane contrast, compared to the widefield images.

Two ROIs were manually defined to cover part of each neuron and to avoid their region of overlap. ROI-integrated time traces clearly showed APs in each recording. In widefield movies, the APs were mixed in each ROI, with distinct amplitudes from the two cells (**Figure 3.4b**, right panel insets, asterisks and apostrophes). The SNR was defined as the ratio of mean AP spike height to baseline standard deviation during a spike-free interval. In CHI movies, the signal from each cell was localized to the corresponding focal plane, and there was little crosstalk between ROIs (**Figure 3.4c**, left). These metrics indicate that CHI provided fast optical sectioning and reduced crosstalk relative to widefield Imaging.

However, the CHI signals had reduced SNR relative to widefield by a factor of 4 for neuron 1, and by a factor of 7 for neuron 2 (**Figure 3.4c**, left), reflecting the fact that CHI optical sections sampled data from only a single focal plane in the cell, whereas widefield images included fluorescence from the whole cell.

Brain-wide neuronal recording in live zebrafish. We implemented CHI in a larger FOV format to make neuronal recoding across a zebrafish brain densely expressing the Ca^{2+} indicator GCaMP6 (**Figure 3.5a**). The animal was paralyzed with α-bungarotoxin to avoid motion artifacts, and the drug PTZ was administered to induce brain-wide epileptiform activity. No optogenetic stimulation was used. We recorded at a framerate of 100 Hz, with a 410 μm FOV. These parameters yielded brain-wide recordings with CHI reconstructions at 50 Hz, sufficient to capture Ca^{2+} dynamics. Movie data were analyzed block-wise (40 μm side square blocks, 13 μm sliding step, with posterior weighted average reconstruction) under the assumption of locally low rank dynamics (SVD with 50 components per block). This experiment used a Hadamard code length of 36 patterns in complement-interleaved sequence, repeated 30 times over 21.6 s.

From one acquisition, widefield and Hadamard movies were estimated with CHI. **Figure 3.5b** shows the dramatic difference in contrast between widefield and CHI in the time-averaged images. To favor an unbiased ROI-based analysis, 15 cell-sized ROIs were automatically selected by Gram-Schmidt orthogonalization of the widefield movie, iteratively selecting ROIs of largest variance over time in the residual movie after projecting out the signals from previous ROIs. This process selected ROIs with the most different and significative signals in the widefield movie. ROIs in widefield data revealed a diversity of transients, with a large common mode decay beginning at

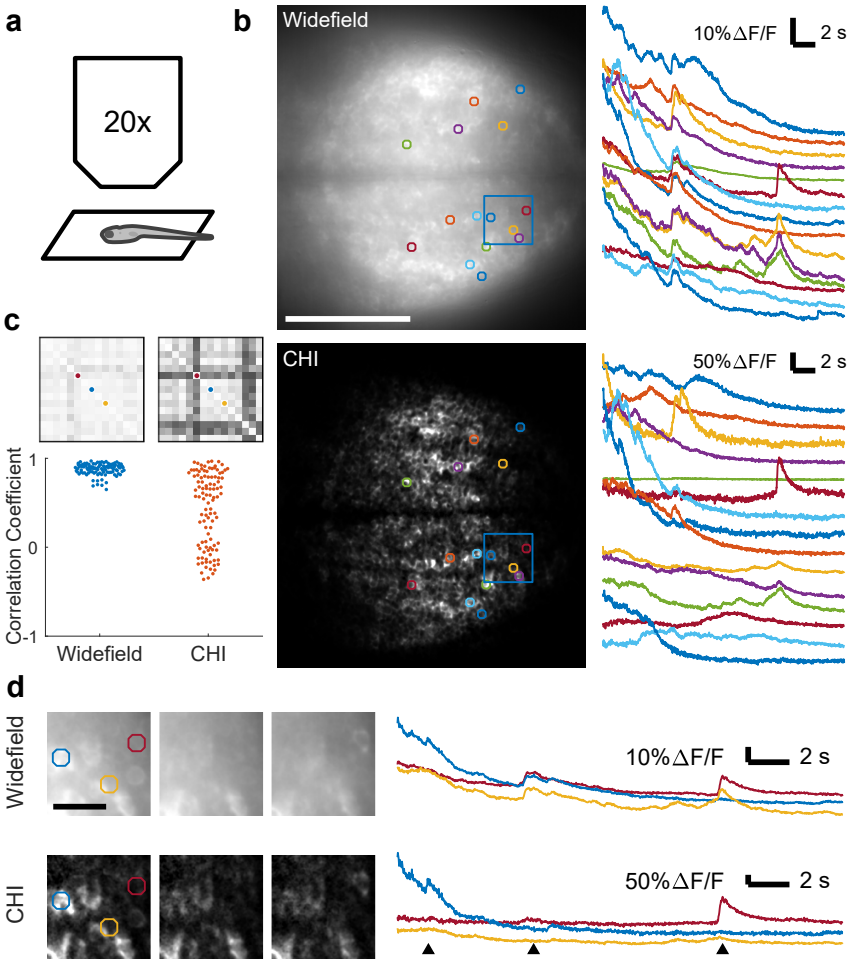

Figure 3.5: CHI high speed optical sectioning of large FOV, high dynamic rank data. (a) Experimental setup for *in vivo* zebrafish imaging. **(b)** Brain-wide FOV containing hundreds of neurons reconstructed at 50 Hz time resolution. Top: Widefield; bottom: CHI. Images show the time average of movies. Scale bar 100 μm. Traces correspond to ROIs sorted from top to bottom. **(c)** CHI recordings showed increased contrast relative to widefield in the cell-to-cell cross correlation matrix, reflecting rejection of out-of-focus common mode signals. Top: Cross-correlation matrices for widefield (left) and CHI (right) signals. Bottom: Distribution of the off-diagonal correlation coefficients showing the spuriously high widefield cross-correlations due to out-of-focus signals. **(d)** Small ROI corresponding to one reconstructed block (from blue frame in b), showing selected Widefield and Hadamard movie frames and ROIs. Triangles indicate timepoints of selected movie frames. Scale bar 20 μm.

$t = 0$, attributed to visually-evoked neural activity (**Figure 3.5b**, right panel). The CHI movie showed large initial transients in only a subset of ROIs. To quantify how different were the neural signals among each set, we calculated their normalized cross-correlations, shown in **Figure 3.5c**. **Figure 3.5d** shows the detail of one reconstruction block, with selected ROIs and corresponding time traces, illustrating the suppression of out-of-focus fluorescence and mixed signal transients. This experiment demonstrated the implementation of high spatiotemporal bandwidth computational optical sectioning, allowing wide-brain neural recording of Ca^{2+} transients.

3.4 Discussion

Compressed Hadamard Imaging (CHI) microscopy is a novel form of computational optical sectioning using structured illumination and ideas from compressed sensing to achieve simultaneously high spatial and temporal resolution. We performed detailed numerical simulations to characterize the properties of the technique. The CHI technique relies on the low-rank statistical structure of neural recordings: while the number of pixels in each image is large, the number of independently varying fluorescence components is much smaller. The spatial and corresponding temporal components of the signals are estimated separately, and then combined to yield a high spatio-temporal resolution reconstructed movie.

We demonstrated these advances by recording wide-area optically sectioned movies in live tissue, including voltage imaging of neurons in acute mouse brain slice with 500 Hz time resolution, and brain-wide Ca^{2+} imaging in live zebrafish with 50 Hz time resolution. These recordings

represent a ~100-fold increase in time resolution compared to the previous report of Hadamard microscopy to generate anti-epileptic drug inhibition maps in **Chapter 2** (without compressed sensing dynamic reconstruction) in which Ca^{2+} dynamics were recorded at 5.6 Hz. CHI can be readily adapted to measure other fast physiological signals with fluorescence microscopy, such as pH, glutamate, acetylcholine, and membrane tension, enabling wide-area high speed optically sectioned recordings while avoiding off-focal contaminating signals.

How does CHI compare to other optical sectioning microscopy techniques? CHI allows optical sectioning at half the maximum pixel rate of the camera, far surpassing point-scanning methods in temporal resolution. The time resolution of CHI is equivalent to that of HiLo microscopy[52,164], but in **Chapter 2** we showed that Hadamard image reconstruction offers better background rejection than HiLo and avoids systematic speckle noise that occurs in HiLo due to the use of a single pseudo-random illumination mask in that technique[138]. Both CHI and HiLo microscopy are susceptible to shot noise from out-of-focus background. The extent to which this noise degrades the signal depends on the sample structure. CHI is anticipated to have lower shot noise than HiLo in the computed images due to the filtering effect of the low-rank representation of the data; though we note that similar post-processing could be applied to HiLo data. Commercially available spinning disk confocal systems offer high-speed imaging and physical optical sectioning, but are incompatible with large-area, high numerical aperture objectives. The micromirror-based optical patterning system of CHI is compatible with any objective. The micromirror system also facilitates combination of the technique with patterned illumination for optogenetic stimulation or photochemistry. To retrofit a fluorescence microscope with a CHI

system is approximately $1/5^{\text{th}}$ of the cost of a spinning disk system and $1/10^{\text{th}}$ of the cost of a two-photon imaging system.

We note that the dynamic estimation algorithm could be adapted to work with any structured illumination technique, including stripe SIM [51,156] or HiLo [139]. For instance, the PSF of stripe SIM could be improved by successive illumination with stripes of different orientation and spatial frequency. With conventional image reconstruction algorithms this approach would decrease time resolution; but with compressed sensing image reconstruction, the full time resolution would be maintained. Hadamard encoding achieves the shortest possible packing of orthogonal codes in binary matrices, and is optimal to minimize the code length while having a flexible choice of spatial code separation.

For practical CHI implementations, acquisition parameters have to be chosen to match experimental needs. The biological process and sample of interest will determine the necessary spatial and temporal resolution. Here follows a step-by-step guide to choose these parameters:

1. Imaging resolution, including optical system and camera spatial resolution, should be determined by the size of static sample features that need to be resolved.
2. DMD projection elements should be resolvable by the imaging system, but smaller than the dynamic objects to be measured.
3. Camera framerate should be twice the maximum temporal resolution of interest.
4. Recording length should be maximized within the limits set by sample stability and technical limitations such as data storage.
5. Finally, the code length L should be maximized, but constrained such that code repetitions R surpass the rank of dynamic data in the sample FOV to be analyzed. For example, if 1000 frames are to be recorded, and the rank is expected to be 10, the code length should

not exceed 50 (100 frames are required to cycle through the code and its interleaved complement).

The reconstruction algorithm for optical section movies has only one adjustable parameter: the number of SVD components should be set to exceed the rank of the underlying sample, and it does not need to be higher than the number of code repetitions. An upper bound to the rank of the sample can be estimated by calculating how many neurons would contribute distinguishable activity to a widefield movie.

Compressed Sensing theory has been used in other microscopy applications[165,166,157–159,167]. These other techniques require explicit regularization to constrain solutions with sparsity properties, together with computationally intensive, parameter-dependent calculations to minimize an objective function. In this work, measurements are compressed but the requirement for low-rank sample representation is implicit, with optical section estimations that result from an analytic and sample-independent direct calculation. There are no adjustable parameters to enforce spatial or temporal sparsity, iterative optimization, or convergence criteria.

Conclusion

This work presents an extension to existing computational optical sectioning methods, to record neuronal activity at high temporal resolution by leveraging the natural redundant structure of these biological signals. Future work could extend the algorithm to accommodate moving or shape-changing samples, that is, samples with low dynamic rank under a more complex signal generation model.

3.5 Manuscript Information

Previously published as

A version of this chapter appeared in[168]:

V. J. Parot*, C. Sing-Long*, Y. Adam, U. L. Böhm, L. Z. Fan, S. L. Farhi, and A. E. Cohen, "Compressed hadamard microscopy for high-speed optically sectioned neuronal activity recordings," *Journal of Physics D: Applied Physics*, vol. 52, p. 144001, 2 2019.

Acknowledgements

This work was supported by the Harvard Data Science Initiative, the Harvard Brain Initiative, and the Howard Hughes Medical Institute. Vicente J. Parot was supported by a Becas Chile scholarship. Carlos Sing-Long was supported by a Harvard Brain Initiative Young Scientist grant awarded to Vicente J. Parot, and was partially supported by Fondecyt grant #11160728.

The author's contribution

Vicente J. Parot and Carlos Sing-Long designed compressed Hadamard imaging, performed experiments, and analyzed data. Vicente J. Parot assisted Yoav Adam in building the Optopatch microscope, and implemented Hadamard microscopy. Urs L. Böhm helped set up zebrafish experiments. Linlin Z. Fan shared Optopatch reagents. Samouil L. Farhi helped in early design of

*These authors contributed equally.

compressed Hadamard imaging. Adam E. Cohen supervised the research. Vicente J. Parot, Carlos Sing-Long, and Adam E. Cohen wrote the paper.

4

Conclusion

Even though all-optical neurophysiology (AON) techniques have been highly optimized for behavioral studies in live animals, their application to *ex vivo* brain tissue has lagged. Acute brain slices offer optical, electrical, and chemical access to any brain region, exposing ~ 10^5 neurons of interest near the tissue surface to be potentially interrogated.

Using advances described in this dissertation, unbiased AON mapping can now be applied to new area-based studies, e.g. to functionally identify rare cell populations, to characterize subtle regional variations in functional properties, and to probe many neurons or regions in parallel with matched conditions.

Context of cross-disciplinary methods

In this work, a cross-disciplinary approach has brought technical innovations from established fields and applied them to neuronal activity recordings.

The main connection is the inspiration from digital telecommunications to implement coded patterns for structured illumination optical sectioning (SIM). The original linear SIM method[48] used sinusoidal illumination patterns, which contain a pure spatial frequency. The resolution gain obtained with linear SIM was attributed to the modulation of image features into a high spatial frequency band. But in scattering tissue, this method could be prone to errors caused by phase distortions of the illumination patterns, when phase distortions are localized to the spatial frequency of the patterns. The origin of this problem is similar to in radio-frequency digital communication, where scattering of radio waves by physical objects cause interference. Code division multiple access (CDMA) and orthogonal frequency-division multiplexing (OFDM) are codification methods that transmit multiple streams of data through a scattering channel, also using Walsh-Hadamard codes to impart orthogonal codification to each data stream[169]. This codification distributes the information content over a spread spectrum, making the codes robust to scattering containing localized phase distortions. This strategy inspired the application of the same orthogonal codes to microscopy in **Chapter 2**, to distinguish neighboring sample locations by their uncorrelated illumination. The resulting Hadamard-coded illumination patterns have a uniform power spectral density in space and in time.

Similarly, the matched filtering demodulation method used for reconstructing optical sections

introduced in **Chapter 2** is a robust method for detecting signals of known shape in noisy measurements. This method is applied widespread, from decoding CDMA and OFDM signals in our cellphones, to detection of gravitational waves[170].

Finally, compressed sensing ideas applied in **Chapter 3** were inspired in its successful application to acceleration in other fields, including MRI data acquisition[171] and black hole imaging[172]. In neuronal activity recordings, the information of interest can be represented concisely (in a factorized representation of cell intensity over space and fluctuations over time), and the measurements are distributed over the concise representation (on average, each patterned illumination frame captures information uniformly from all cells). In this work the sparse quality of the sample is implicit in a direct reconstruction of data, thus the method avoids numerical optimization with explicit sparsity and consistency that are standard in prior compressed sensing applications[173].

Future applications

This work enables wide-area all-optical studies of genetic mechanisms underlying neurological disorders such as epilepsy. Dysfunction in subtype-specific excitability[174], or in synaptic transmission of specific neuronal subpopulations[175] are suspected causes for epileptogenesis. Wide-area AON mapping of excitability perturbations and functional connectivity by tool pharmacology is a high-throughput method with the potential to transform current mapping efforts, which commonly use a single point patch-clamp measurement in combination with Ca^{2+} reporters and/or voltage-sensitive dyes.

One promising application is the use of compressed Hadamard imaging for 1P voltage recordings in live animals. Many existing *in vivo* fluorescence neural imaging techniques rely on unmixing methods to separate signals from neighboring neurons that mix into common measurements. However, to study single-cell correlations in subthreshold membrane voltage fluctuations[83], optical sectioning based on a physical basis of geometrical source of detected light may provide an advantage compared with unmixing methods, which have to rely on signal decorrelation in order to separate units. Thus it is likely that compressed Hadamard optical sectioning allows for a denser expression of voltage reporter for 1P excitation measurements, compared to the single cell performance limit that may be expected with or without unmixing.

Remaining optical sectioning challenges

In wide-area AON, limited availability of fluorescent signals imposes a tradeoff between spatiotemporal resolution and number of cells that can be recorded. Protocols in this work record from a single focal plane, treating many other cells in the volume as unwanted background. However, there is no fundamental reason why microscopes shouldn't have a focal volume instead of a focal plane. Wide-area Hadamard AON could be extended to three-dimensions. By adding depth modulation to the illumination and/or detection paths, the cells' depth could be measured in addition to their functional responses to optogenetic stimulation, thereby converting unwanted off-focal signals into useful volumetric neurophysiology data. These advances would accelerate the application of wide-area all-optical neurophysiology to other neurobiology problems.

A

Continuous domain image formation model

This Appendix extends **Section 2.2.4.6** by presenting an analysis of static Hadamard microscopy using a linear optical system model analysis of image formation and image reconstruction. The result shows that this process produces a confocal optical section. This analysis is equivalent to the one presented in **Section 2.2.4.6**, but in continuous notation and with a more detailed presentation of steps.

Throughout this Appendix, we use $g(x, z)$ to represent the three-dimensional fluorescence distribution in the sample for location x and depth z, where x represents a two-component vector of position in the plane. We use $p(x, t) \in \{-1, 1\}$ to represent an idealized binary illumination pattern for location x at time t. Scattering and defocus of light are represented by the point-spread functions (PSF) $s_1(x, z)$ and $s_2(x, z)$, corresponding to illumination and collection respectively (i.e. s_1 is the three-dimensional distribution of light intensity at the sample caused by a point source illumination pattern, and s_2 is the three-dimensional distribution of sensitivity from the sample in a point detector at the camera plane).

We define *in extenso* the two-dimensional convolution in the plane between functions $f(x_0, x_1)$ and $h(x_0, x_1)$ as

$$f(x_0, x_1) * h(x_0, x_1) = \int \int f(x_0 - u_0, x_1 - u_1) h(u_0, u_1) d u_0 d u_1$$

although we will use the simplified notation where x is the two-component position vector from hereon:

$$f(x) * h(x) = \int f(x - u) h(u) d u$$

We begin by modeling the patterned illumination at the sample as the convolution of the designed patterns with the illumination PSF

$$p(x,t) * s_1(x,z) = \int p(x-u,t)s_1(u,z)\,du$$

The emission is given by the product of the fluorescence distribution and the illumination at the sample, $g(x,z)\left(p(x,t) * s_1(x,z)\right)$, and the measurement $m(x,t)$ at the camera is obtained convolving the emission with the collection PSF, then integrating across depths at the detector plane.

$$m(x,t) = \int \left[g(x,z)\left(p(x,t) * s_1(x,z)\right)\right] * s_2(x,z)\,dz$$

developing the inner terms of the expression, we rewrite

$$p(x,t) * s_1(x,z) = \int p(x-u,t)s_1(u,z)\,du$$

and

$$\left[g(x,z)\left(p(x,t) * s_1(x,z)\right)\right] * s_2(x,z) = \int g(x-v,z) \int p(x-v-u,t)s_1(u,z)\,du\; s_2(v,z)\,dv$$

leading to

$$m(x,t) = \int\int g(x-v,z) \int p(x-v-u,t) s_1(u,z)\,du\; s_2(v,z)\,dv\; dz$$

Hadamard reconstructions $r(x)$ are obtained by multiplying measured data with the reference illumination patterns and then aggregating over all patterns, as shown in **Section 2.2.4.4**

$$r(x) = \int m(x,t)\,p(x,t)\,dt$$
$$r(x) = \int\int \left[g(x,z)\left(p(x,t) * s_1(x,z)\right)\right] * s_2(x,z)\,dz\; p(x,t)\,dt$$
$$r(x) = \int\int\int g(x-v,z) \int p(x-v-u,t) s_1(u,z)\,du\; s_2(v,z)\,dv\; dz\; p(x,t)\,dt$$
$$r(x) = \int\int g(x-v,z) \int\int p(x-v-u,t)\,p(x,t)\,dt\; s_1(u,z)\,du\; s_2(v,z)\,dv\; dz$$

The choice of illumination patterns forming an orthogonal basis allows

$$\int p(x-(v+u),t)\,p(x,t)\,dt = \delta(u+v)$$

which yields

$$r(x) = \int\int g(x-v,z) \int \delta(u+v) s_1(u,z)\,du\; s_2(v,z)\,dv\; dz$$

Recall that by the sifting property of convolution,

$$\int \delta(u+v)s_1(u,z)\,du = s_1(-v,z)$$

and then

$$r(x) = \int\int g(x-v,z)s_1(-v,z)s_2(v,z)\,dv\,dz$$

We identify this integral as a convolution,

$$\int g(x-v,z)s_1(-v,z)s_2(v,z)\,dv = g(x,z) * (s_1(-x,z)s_2(x,z))$$

and defining a confocal PSF as the product of the illumination and collection PSFs, $s(x,z) \equiv s_1(-x,z)s_2(x,z)$, we can conclude:

$$r(x) = \int m(x,t)p(x,t)\,dt = \int g(x,z) * s(x,z)\,dz$$

That is, the static Hadamard optical section reconstruction $r(x)$, calculated as the time-correlation with the designed patterns, is an image of the focal plane, given by the convolution of the fluorescent distribution and a PSF composed of the product of illumination and collection PSFs.

B

The relation between confocal and Hadamard data

This Appendix extends **Section 3.2.1.2** by exploring the optical sectioning property of Hadamard demodulation, as applied to static samples, and considering a practical calibration method for illumination patterns. The system is modeled as a continuous intensity-linear space-invariant optical system with patterned illumination. The illumination is further assumed to consist of spatially-uncorrelated illumination functions of time. Demodulation using matched

filtering results in a confocal optical section.

The model for image formation is

$$u(\boldsymbol{p}, t) = \int_{z \geq 0} p_C(\boldsymbol{p} - \boldsymbol{q}, z) f(\boldsymbol{q}, z) \mu(\boldsymbol{q}, z, t) \, d\boldsymbol{q} \, dz$$

where p_C is the collection PSF, f is the sample fluorescence and μ is the illumination onto the sample. Here we have assumed the camera is imaged to the xy-plane at the $z = 0$ coordinate, and that the sample is on the positive z-axis. The illumination process is modeled as

$$\mu(\boldsymbol{q}, z, t) = \int p_I(\boldsymbol{q} - \boldsymbol{r}, z) \pi(\boldsymbol{r}, t) \, d\boldsymbol{r},$$

where p_I is the illumination PSF, and π is the illumination pattern. Using this model, the practical calibration data can be ideally represented as

$$c(\boldsymbol{p}, t) = \int p_C(\boldsymbol{p} - \boldsymbol{q}, z_0) \mu(\boldsymbol{q}, z_0, t) \, d\boldsymbol{q},$$

i.e., the calibration screen corresponds to a uniform f fully concentrated on the plane $z = z_0$. The location z_0 represents deviation between the calibration plane and the focal plane, normally set to $z_0 = 0$. The positive-only illumination pattern is compensated by

$$c^{\partial}(\boldsymbol{p}, t) = c(\boldsymbol{p}, t) - \int_{t \geq 0} c(\boldsymbol{p}, t) \, dt,$$

and matched filtering demodulation using the calibration data becomes

$$\int_{t\geq 0} c^{\delta}(\boldsymbol{p},t)u(\boldsymbol{p},t)\,dt = \int_{z\geq 0} p_C(\boldsymbol{p}-\boldsymbol{q}',z_0)p_C(\boldsymbol{p}-\boldsymbol{q},z)f(\boldsymbol{q},z)\left(\int_{t\geq 0}\mu(\boldsymbol{q}',z_0,t)\mu(\boldsymbol{q},z,t)\,dt\right)d\boldsymbol{q}\,d\boldsymbol{q}'\,dz$$

whence

$$\int_{t\geq 0}\mu(\boldsymbol{q}',z_0,t)\mu(\boldsymbol{q},z,t)\,dt = \int_{z\geq 0} p_I(\boldsymbol{q}'-\boldsymbol{r}',z_0)p_I(\boldsymbol{q}-\boldsymbol{r},z)\left(\int_{t\geq 0}\pi(\boldsymbol{r}',t)\pi(\boldsymbol{r},t)\,dt\right)d\boldsymbol{r}'\,d\boldsymbol{r}.$$

We assume a full orthonormal set of illumination patterns such that

$$\int_{t\geq 0}\pi(\boldsymbol{r}',t)\pi(\boldsymbol{r},t)\,dt = \delta(\boldsymbol{r}-\boldsymbol{r}')$$

and it follows that

$$\begin{aligned}\int_{t\geq 0}\mu(\boldsymbol{q}',z_0,t)\mu(\boldsymbol{q},z,t)\,dt &= \int p_I(\boldsymbol{q}'-\boldsymbol{r}',z_0)p_I(\boldsymbol{q}-\boldsymbol{r}',z)d\boldsymbol{r}' \\ &= \int p_I(\boldsymbol{r}',z_0)p_I(\boldsymbol{q}-\boldsymbol{q}'-\boldsymbol{r}',z)d\boldsymbol{r}'\end{aligned}$$

where we used the change of variables $\boldsymbol{r}' \to \boldsymbol{r}' + \boldsymbol{q}'$ to obtain the last equality. Since the change

of variables $\boldsymbol{q}' \to \boldsymbol{q}' + \boldsymbol{q}$ yields

$$\int p_C(\boldsymbol{p} - \boldsymbol{q}', z_0) p_C(\boldsymbol{p} - \boldsymbol{q}, z) p_I(\boldsymbol{r}', z_0) p_I(\boldsymbol{q} - \boldsymbol{q}' - \boldsymbol{r}', z)\, d\boldsymbol{q}'\, d\boldsymbol{r}' =$$
$$\int p_C(\boldsymbol{p} - \boldsymbol{q} - \boldsymbol{q}', z_0) p_C(\boldsymbol{p} - \boldsymbol{q}, z) p_I(\boldsymbol{r}', z_0) p_I(\boldsymbol{q}' - \boldsymbol{r}', z)\, d\boldsymbol{q}'\, d\boldsymbol{r}'$$

we conclude

$$\int_{t \geq 0} c^{\partial}(\boldsymbol{p}, t) u(\boldsymbol{p}, t)\, dt = \int_{z \geq 0} p_H(\boldsymbol{p} - \boldsymbol{q}, z) f(\boldsymbol{q}, z) d\boldsymbol{q}\, dz$$

with

$$p_H(\boldsymbol{p}, z) = p_C(\boldsymbol{p}, z) \int p_C(\boldsymbol{p} - \boldsymbol{q}', z_0) \left(\int p_I(\boldsymbol{r}', z_0) p_I(\boldsymbol{q}' - \boldsymbol{r}', z)\, d\boldsymbol{r}' \right) d\boldsymbol{q}'.$$

The optical section PSF given by p_H is the product of the collection PSF and the illumination PSF, modified by the in-plane imaging quality of the calibration pattern used for demodulation.

C

Estimating widefield sequences from complementary illumination patterns

This Appendix extends **Section 3.2.11** by considering the effect of fast fluorescence dynamics, e.g. when there is a transient increase in intensity that persists during one illumination pattern but not its complement. The estimated widefield movie then includes an artifact comprising the change in intensity, multiplied by the illumination pattern used at that time.

Appendix B shows that the estimate of the widefield sequence for a time-dependent fluores-

cence is given by

$$u(\boldsymbol{p}, t + \Delta t) + u(\boldsymbol{p}, t) =$$

$$\int_{z \geq 0} p_C(\boldsymbol{p} - \boldsymbol{q}, z)(f(\boldsymbol{q}, z, t + \Delta t)\mu(\boldsymbol{q}, z, t + \Delta t) + f(\boldsymbol{q}, z, t)\mu(\boldsymbol{q}, z, t))\, d\boldsymbol{q}\, dz.$$

If the illumination at $t + \Delta t$ is complementary to that used at t we have both $\pi(\boldsymbol{r}, t + \Delta t) + \pi(\boldsymbol{r}, t) = 1$ and $\mu(\boldsymbol{q}, z, t + \Delta t) + \mu(\boldsymbol{q}, z, t) = 1$. It follows that

$$f(\boldsymbol{q}, z, t + \Delta t)\mu(\boldsymbol{q}, z, t + \Delta t) + f(\boldsymbol{q}, z, t)\mu(\boldsymbol{q}, z, t) =$$

$$f(\boldsymbol{q}, z, t) + \mu(\boldsymbol{q}, z, t + \Delta t)(f(\boldsymbol{q}, z, t + \Delta t) - f(\boldsymbol{q}, z, t)).$$

A straightforward manipulation shows that

$$u(\boldsymbol{p}, t + \Delta t) + u(\boldsymbol{p}, t) =$$

$$u_w(\boldsymbol{p}, t) + \int_{z \geq 0} p_C(\boldsymbol{p} - \boldsymbol{q}, z)(f(\boldsymbol{q}, z, t + \Delta t) - f(\boldsymbol{q}, z, t))\mu(\boldsymbol{q}, z, t + \Delta t)\, d\boldsymbol{q}\, dz,$$

where u_w denotes the widefield sequence. Observe the additive component depends *only* on the variations of the fluorescence at times t and $t + \Delta t$.

References

[1] S. R. y. Cajal, *Reglas y consejos sobre investigación científica: los tónicos de la voluntad*. Editorial CSIC - CSIC Press, 1999.

[2] J.-A. Conchello and J. W. Lichtman, "Optical sectioning microscopy," *Nature Methods*, vol. 2, pp. 920–931, 12 2005.

[3] T. Itoh, "Fluorescence and phosphorescence from higher excited states of organic molecules," *Chemical Reviews*, vol. 112, pp. 4541–4568, 8 2012.

[4] P. T. C. So, C. Y. Dong, B. R. Masters, and K. M. Berland, "Two-photon excitation fluorescence microscopy," *Annual Review of Biomedical Engineering*, vol. 2, no. 1, pp. 399–429, 2000.

[5] S. L. Jacques, "Optical properties of biological tissues: a review," *Physics in Medicine and Biology*, vol. 58, p. R37–R61, 5 2013.

[6] J. M. Schmitt and G. Kumar, "Turbulent nature of refractive-index variations in biological tissue," *Optics Letters*, vol. 21, pp. 1310–1312, 8 1996.

[7] J. S. O'Brien and E. L. Sampson, "Lipid composition of the normal human brain: gray matter, white matter, and myelin," *Journal of Lipid Research*, vol. 6, pp. 537–544, 10 1965.

[8] A. N. Yaroslavsky, P. C. Schulze, I. V. Yaroslavsky, R. Schober, F. Ulrich, and H.-J. Schwarzmaier, "Optical properties of selected native and coagulated human brain tissues in vitro in the visible and near infrared spectral range," *Physics in Medicine and Biology*, vol. 47, p. 2059–2073, 6 2002.

[9] C. Mätzler, "MATLAB Functions for Mie Scattering and Absorption," Tech. Rep. 2002-08, Institut für Angewandte Physik, Bern, Switzerland, 2002.

[10] S. A. Prahl, "Mie scattering calculator," 2018.

[11] W. F. Cheong, S. A. Prahl, and A. J. Welch, "A review of the optical properties of biological tissues," *IEEE Journal of Quantum Electronics*, vol. 26, pp. 2166–2185, 12 1990.

[12] P. Nelson, *From Photon to Neuron: Light, Imaging, Vision*. Princeton University Press, May 2017.

[13] R. F. Cleveland and J. L. Ulcek, "Questions and answers about biological effects and potential hazards of radiofrequency electromagnetic fields," *OET Bulletin*, p. 1–36, 1999.

[14] S. J. Blanksby and G. B. Ellison, "Bond dissociation energies of organic molecules," *Accounts of Chemical Research*, vol. 36, pp. 255–263, 4 2003.

[15] S. R. Cherry, J. Sorenson, M. E. Phelps, and B. M. Methé, "Physics in nuclear medicine," *Medical Physics*, vol. 31, no. 8, pp. 2370–2371, 2004.

[16] A. Zumbusch, G. R. Holtom, and X. S. Xie, "Three-dimensional vibrational imaging by coherent anti-stokes raman scattering," *Physical Review Letters*, vol. 82, pp. 4142–4145, 5 1999.

[17] G. Scarcelli and S. H. Yun, "Confocal brillouin microscopy for three-dimensional mechanical imaging," *Nature Photonics*, vol. 2, pp. 39–43, 1 2008.

[18] F. Helmchen and W. Denk, "Deep tissue two-photon microscopy," *Nature Methods*, vol. 2, pp. 932–940, Dec. 2005.

[19] C. Lefort, "A review of biomedical multiphoton microscopy and its laser sources," *Journal of Physics D: Applied Physics*, vol. 50, p. 423001, 9 2017.

[20] N. G. Horton, K. Wang, D. Kobat, C. G. Clark, F. W. Wise, C. B. Schaffer, and C. Xu, "In vivo three-photon microscopy of subcortical structures within an intact mouse brain," *Nature Photonics*, vol. 7, pp. 205–209, 3 2013.

[21] W. Min, S. Lu, M. Rueckel, G. R. Holtom, and X. S. Xie, "Near-degenerate four-wave-mixing microscopy," *Nano Letters*, vol. 9, pp. 2423–2426, 6 2009.

[22] M.-H. Yang, M. Abashin, P. A. Saisan, P. Tian, C. G. L. Ferri, A. Devor, and Y. Fainman, "Non-degenerate 2-photon excitation in scattering medium for fluorescence microscopy," *Optics Express*, vol. 24, pp. 30173–30187, 12 2016.

[23] D. Débarre, W. Supatto, A.-M. Pena, A. Fabre, T. Tordjmann, L. Combettes, M.-C. Schanne-Klein, and E. Beaurepaire, "Imaging lipid bodies in cells and tissues using third-harmonic generation microscopy," *Nature Methods*, vol. 3, pp. 47–53, 1 2006.

[24] L. Moreaux, O. Sandre, and J. Mertz, "Membrane imaging by second-harmonic generation microscopy," *JOSA B*, vol. 17, pp. 1685–1694, 10 2000.

[25] S. W. Hell and J. Wichmann, "Breaking the diffraction resolution limit by stimulated emission: stimulated-emission-depletion fluorescence microscopy," *Optics Letters*, vol. 19, pp. 780–782, 6 1994.

[26] W. Min, S. Lu, S. Chong, R. Roy, G. R. Holtom, and X. S. Xie, "Imaging chromophores with undetectable fluorescence by stimulated emission microscopy," *Nature*, vol. 461, pp. 1105–1109, 10 2009.

[27] C. W. Freudiger, W. Min, B. G. Saar, S. Lu, G. R. Holtom, C. He, J. C. Tsai, J. X. Kang, and X. S. Xie, "Label-free biomedical imaging with high sensitivity by stimulated raman scattering microscopy," *Science*, vol. 322, pp. 1857–1861, 12 2008.

[28] W. Becker, "Fluorescence lifetime imaging – techniques and applications," *Journal of Microscopy*, vol. 247, no. 2, pp. 119–136, 2012.

[29] J. R. Lakowicz, H. Szmacinski, K. Nowaczyk, and M. L. Johnson, "Fluorescence lifetime imaging of free and protein-bound NADH," *Proceedings of the National Academy of Sciences*, vol. 89, pp. 1271–1275, 2 1992.

[30] D. Fu, T. Ye, T. E. Matthews, G. Yurtsever, and W. S. Warren, "Two-color, two-photon, and excited-state absorption microscopy," *Journal of Biomedical Optics*, vol. 12, p. 054004, 9 2007.

[31] V. Ntziachristos, "Going deeper than microscopy: the optical imaging frontier in biology," *Nature Methods*, vol. 7, pp. 603–614, 8 2010.

[32] M. Born and E. Wolf, *Principles of Optics: Electromagnetic Theory of Propagation, Interference and Diffraction of Light*. Cambridge University Press, 2 2000.

[33] J. W. Goodman, *Introduction to Fourier Optics*. Roberts and Company Publishers, 2005.

[34] E. Abbe, "Beiträge zur theorie des mikroskops und der mikroskopischen wahrnehmung," *Archiv für mikroskopische Anatomie*, vol. 9, pp. 413–468, 12 1873.

[35] E. Betzig, G. H. Patterson, R. Sougrat, O. W. Lindwasser, S. Olenych, J. S. Bonifacino, M. W. Davidson, J. Lippincott-Schwartz, and H. F. Hess, "Imaging intracellular fluorescent proteins at nanometer resolution," *Science*, vol. 313, pp. 1642–1645, 9 2006.

[36] M. J. Rust, M. Bates, and X. Zhuang, "Sub-diffraction-limit imaging by stochastic optical reconstruction microscopy (storm)," *Nature Methods*, vol. 3, pp. 793–796, 10 2006.

[37] H. A. Haus, *Waves and Fields in Optoelectronics*. Prentice Hall, Incorporated, 1984.

[38] J. Pawley, *Handbook of Biological Confocal Microscopy*. Springer Science & Business Media, 8 2010.

[39] W. Denk and K. Svoboda, "Photon upmanship: Why multiphoton imaging is more than a gimmick," *Neuron*, vol. 18, pp. 351–357, 3 1997.

[40] A. C. Chan, T. T. Wong, K. K. Wong, E. Y. Lam, and K. K. Tsia, "Revisit laser scanning fluorescence microscopy performance under fluorescence-lifetime-limited regime," in *Imaging, Manipulation, and Analysis of Biomolecules, Cells, and Tissues XII*, vol. 8947, p. 894726, International Society for Optics and Photonics, 2014.

[41] D. Toomre and J. B. Pawley, "Disk-scanning confocal microscopy," in *Handbook Of Biological Confocal Microscopy* (J. B. Pawley, ed.), pp. 221–238, Boston, MA: Springer US, 2006.

[42] T. A. Planchon, L. Gao, D. E. Milkie, M. W. Davidson, J. A. Galbraith, C. G. Galbraith, and E. Betzig, "Rapid three-dimensional isotropic imaging of living cells using bessel beam plane illumination," *Nature Methods*, vol. 8, pp. 417–423, 5 2011.

[43] P. J. Verveer, J. Swoger, F. Pampaloni, K. Greger, M. Marcello, and E. H. K. Stelzer, "High-resolution three-dimensional imaging of large specimens with light sheet–based microscopy," *Nature Methods*, vol. 4, pp. 311–313, 4 2007.

[44] H.-U. Dodt, U. Leischner, A. Schierloh, N. Jährling, C. P. Mauch, K. Deininger, J. M. Deussing, M. Eder, W. Zieglgänsberger, and K. Becker, "Ultramicroscopy: three-dimensional visualization of neuronal networks in the whole mouse brain," *Nature Methods*, vol. 4, pp. 331–336, 4 2007.

[45] S. Wolf, W. Supatto, G. Debrégeas, P. Mahou, S. G. Kruglik, J.-M. Sintes, E. Beaurepaire, and R. Candelier, "Whole-brain functional imaging with two-photon light-sheet microscopy," *Nature Methods*, vol. 12, pp. 379–380, 5 2015.

[46] M. Tokunaga, N. Imamoto, and K. Sakata-Sogawa, "Highly inclined thin illumination enables clear single-molecule imaging in cells," *Nature Methods*, vol. 5, pp. 159–161, 2 2008.

[47] M. B. Bouchard, V. Voleti, C. S. Mendes, C. Lacefield, W. B. Grueber, R. S. Mann, R. M. Bruno, and E. M. C. Hillman, "Swept confocally-aligned planar excitation (scape) microscopy for high-speed volumetric imaging of behaving organisms," *Nature Photonics*, vol. 9, pp. 113–119, 2 2015.

[48] M. a. A. Neil, R. Juškaitis, and T. Wilson, "Method of obtaining optical sectioning by using structured light in a conventional microscope," *Optics Letters*, vol. 22, pp. 1905–1907, 12 1997.

[49] D. Débarre, E. J. Botcherby, M. J. Booth, and T. Wilson, "Adaptive optics for structured illumination microscopy," *Optics Express*, vol. 16, pp. 9290–9305, 6 2008.

[50] L. Shao, "Suitable samples for structured-illumination microscopy," 12 2014.

[51] M. G. L. Gustafsson, "Surpassing the lateral resolution limit by a factor of two using structured illumination microscopy," *Journal of Microscopy*, vol. 198, pp. 82–87, 5 2000.

[52] D. Lim, T. N. Ford, K. K. Chu, and J. Mertz, "Optically sectioned in vivo imaging with speckle illumination hilo microscopy," *Journal of Biomedical Optics*, vol. 16, no. 1, pp. 016014–016014–8, 2011.

[53] J. Mertz and J. Kim, "Scanning light-sheet microscopy in the whole mouse brain with hilo background rejection," *Journal of Biomedical Optics*, vol. 15, no. 1, 2010.

[54] E. Mudry, K. Belkebir, J. Girard, J. Savatier, E. L. Moal, C. Nicoletti, M. Allain, and A. Sentenac, "Structured illumination microscopy using unknown speckle patterns," *Nature Photonics*, vol. 6, pp. 312–315, 5 2012.

[55] D. H. Kim, J. Kim, J. C. Marques, A. Grama, D. G. Hildebrand, W. Gu, J. M. Li, and D. N. Robson, "Pan-neuronal calcium imaging with cellular resolution in freely swimming zebrafish," *Nature methods*, vol. 14, no. 11, p. 1107, 2017.

[56] Q. S. Hanley, P. J. Verveer, M. J. Gemkow, D. Arndt-Jovin, and T. M. Jovin, "An optical sectioning programmable array microscope implemented with a digital micromirror device," *Journal of Microscopy*, vol. 196, no. 3, pp. 317–331, 1999.

[57] T. Wilson, M. A. A. Neil, and R. Juskaitis, "Confocal microscopy apparatus and method," 2 2004.

[58] J. Mertz, "Optical sectioning microscopy with planar or structured illumination," *Nature Methods*, vol. 8, pp. 811–819, 10 2011.

[59] E. M. Izhikevich, *Dynamical Systems in Neuroscience*. MIT Press, 2007.

[60] R. Sherman-Gold, ed., *The Axon Guide for Electrophysiology & Biophysics Laboratory Techniques*. Axon Instruments, 1993.

[61] E. Neher and B. Sakmann, "Single-channel currents recorded from membrane of denervated frog muscle fibres," *Nature*, vol. 260, p. 799, 4 1976.

[62] J. M. Fernandez, E. Neher, and B. D. Gomperts, "Capacitance measurements reveal stepwise fusion events in degranulating mast cells," *Nature*, vol. 312, p. 453, 11 1984.

[63] F. A. Edwards, A. Konnerth, B. Sakmann, and T. Takahashi, "A thin slice preparation for patch clamp recordings from neurones of the mammalian central nervous system," *Pflügers Archiv*, vol. 414, pp. 600–612, 9 1989.

[64] A. Citri and R. C. Malenka, "Synaptic plasticity: Multiple forms, functions, and mechanisms," *Neuropsychopharmacology*, vol. 33, pp. 18–41, 1 2008.

[65] R. Heim, D. C. Prasher, and R. Y. Tsien, "Wavelength mutations and posttranslational autoxidation of green fluorescent protein," *Proceedings of the National Academy of Sciences*, vol. 91, pp. 12501–12504, 12 1994.

[66] A. Miyawaki, J. Llopis, R. Heim, J. M. McCaffery, J. A. Adams, M. Ikura, and R. Y. Tsien, "Fluorescent indicators for ca 2+ based on green fluorescent proteins and calmodulin," *Nature*, vol. 388, p. 882, 8 1997.

[67] N. C. Shaner, R. E. Campbell, P. A. Steinbach, B. N. G. Giepmans, A. E. Palmer, and R. Y. Tsien, "Improved monomeric red, orange and yellow fluorescent proteins derived from *Discosoma* sp. red fluorescent protein," *Nature Biotechnology*, vol. 22, pp. 1567–1572, 12 2004.

[68] Y. Zhao, S. Araki, J. Wu, T. Teramoto, Y.-F. Chang, M. Nakano, A. S. Abdelfattah, M. Fujiwara, T. Ishihara, T. Nagai, and R. E. Campbell, "An expanded palette of genetically encoded ca2+ indicators," *Science*, vol. 333, pp. 1888–1891, 9 2011.

[69] J. Akerboom, N. Carreras Calderón, L. Tian, S. Wabnig, M. Prigge, J. Tolö, A. Gordus, M. B. Orger, K. E. Severi, J. J. Macklin, R. Patel, S. R. Pulver, T. J. Wardill, E. Fischer, C. Schüler, T.-W. Chen, K. S. Sarkisyan, J. S. Marvin, C. I. Bargmann, D. S. Kim, S. Kügler, L. Lagnado, P. Hegemann, A. Gottschalk, E. R. Schreiter, and L. L. Looger, "Genetically encoded calcium indicators for multi-color neural activity imaging and combination with optogenetics," *Frontiers in Molecular Neuroscience*, vol. 6, 2013.

[70] H. Dana, Y. Sun, B. Mohar, B. Hulse, J. P. Hasseman, G. Tsegaye, A. Tsang, A. Wong, R. Patel, J. J. Macklin, Y. Chen, A. Konnerth, V. Jayaraman, L. L. Looger, E. R. Schreiter, K. Svoboda, and D. S. Kim, "High-performance gfp-based calcium indicators for imaging activity in neuronal populations and microcompartments," *bioRxiv*, p. 434589, 10 2018.

[71] D. E. Clapham, "Calcium signaling," *Cell*, vol. 131, pp. 1047–1058, 12 2007.

[72] M. Z. Lin and M. J. Schnitzer, "Genetically encoded indicators of neuronal activity," *Nature neuroscience*, vol. 19, no. 9, p. 1142, 2016.

[73] K. Svoboda and R. Yasuda, "Principles of two-photon excitation microscopy and its applications to neuroscience," *Neuron*, vol. 50, pp. 823–839, 6 2006.

[74] M. B. Ahrens, M. B. Orger, D. N. Robson, J. M. Li, and P. J. Keller, "Whole-brain functional imaging at cellular resolution using light-sheet microscopy," *Nature Methods*, vol. 10, pp. 413–420, May 2013.

[75] P. Symvoulidis, A. Lauri, A. Stefanoiu, M. Cappetta, S. Schneider, H. Jia, A. Stelzl, M. Koch, C. C. Perez, A. Myklatun, S. Renninger, A. Chmyrov, T. Lasser, W. Wurst, V. Ntziachristos, and G. G. Westmeyer, "NeuBtracker—imaging neurobehavioral dynamics in freely behaving fish," *Nature Methods*, vol. 14, pp. 1079–1082, Nov. 2017.

[76] N. J. Sofroniew, D. Flickinger, J. King, and K. Svoboda, "A large field of view two-photon mesoscope with subcellular resolution for in vivo imaging," *eLife*, vol. 5, p. e14472, 6 2016.

[77] S. Weisenburger, F. Tejera, J. Demas, B. Chen, J. Manley, F. T. Sparks, F. Martínez Traub, T. Daigle, H. Zeng, A. Losonczy, and A. Vaziri, "Volumetric Ca2+ Imaging in the Mouse Brain Using Hybrid Multiplexed Sculpted Light Microscopy," *Cell*, vol. 177, pp. 1050–1066.e14, May 2019.

[78] S. Weisenburger and A. Vaziri, "A Guide to Emerging Technologies for Large-Scale and Whole-Brain Optical Imaging of Neuronal Activity," *Annual Review of Neuroscience*, vol. 41, no. 1, pp. 431–452, 2018.

[79] L. B. Cohen, "Changes in neuron structure during action potential propagation and synaptic transmission.," *Physiological Reviews*, vol. 53, pp. 373–418, Apr. 1973.

[80] E. W. Miller, "Small molecule fluorescent voltage indicators for studying membrane potential," *Current opinion in chemical biology*, vol. 33, pp. 74–80, 8 2016.

[81] J. M. Kralj, A. D. Douglass, D. R. Hochbaum, D. Maclaurin, and A. E. Cohen, "Optical recording of action potentials in mammalian neurons using a microbial rhodopsin," *Nature Methods*, vol. 9, pp. 90–95, 1 2012.

[82] D. R. Hochbaum, Y. Zhao, S. L. Farhi, N. Klapoetke, C. A. Werley, V. Kapoor, P. Zou, J. M. Kralj, D. Maclaurin, N. Smedemark-Margulies, J. L. Saulnier, G. L. Boulting, C. Straub, Y. K. Cho, M. Melkonian, G. K.-S. Wong, D. J. Harrison, V. N. Murthy, B. L. Sabatini, E. S. Boyden, R. E. Campbell, and A. E. Cohen, "All-optical electrophysiology in mammalian neurons using engineered microbial rhodopsins," *Nature Methods*, vol. 11, pp. 825–833, 8 2014.

[83] Y. Adam, J. J. Kim, S. Lou, Y. Zhao, M. E. Xie, D. Brinks, H. Wu, M. A. Mostajo-Radji, S. Kheifets, V. Parot, S. Chettih, K. J. Williams, B. Gmeiner, S. L. Farhi, L. Madisen, E. K. Buchanan, I. Kinsella, D. Zhou, L. Paninski, C. D. Harvey, H. Zeng, P. Arlotta, R. E. Campbell, and A. E. Cohen, "Voltage imaging and optogenetics reveal behaviour-dependent changes in hippocampal dynamics," *Nature*, p. 1, May 2019.

[84] Y. Kubota, F. Karube, M. Nomura, A. T. Gulledge, A. Mochizuki, A. Schertel, and Y. Kawaguchi, "Conserved properties of dendritic trees in four cortical interneuron subtypes," *Scientific Reports*, vol. 1, p. 89, Sept. 2011.

[85] Y. Xu, P. Zou, and A. E. Cohen, "Voltage imaging with genetically encoded indicators," *Current opinion in chemical biology*, vol. 39, pp. 1–10, 8 2017.

[86] S. Sankaranarayanan, D. De Angelis, J. E. Rothman, and T. A. Ryan, "The use of phluorins for optical measurements of presynaptic activity," *Biophysical Journal*, vol. 79, pp. 2199–2208, 10 2000.

[87] V. M. Paramonov, V. Mamaeva, C. Sahlgren, and A. Rivero-Muller, "Genetically-encoded tools for cAMP probing and modulation in living systems," *Frontiers in Pharmacology*, vol. 6, 2015.

[88] J. Berg, Y. P. Hung, and G. Yellen, "A genetically encoded fluorescent reporter of atp:adp ratio," *Nature Methods*, vol. 6, pp. 161–166, 2 2009.

[89] J. S. Marvin, B. G. Borghuis, L. Tian, J. Cichon, M. T. Harnett, J. Akerboom, A. Gordus, S. L. Renninger, T.-W. Chen, C. I. Bargmann, M. B. Orger, E. R. Schreiter, J. B. Demb, W.-B. Gan, S. A. Hires, and L. L. Looger, "An optimized fluorescent probe for visualizing glutamate neurotransmission," *Nature Methods*, vol. 10, pp. 162–170, 2 2013.

[90] M. Jing, P. Zhang, G. Wang, J. Feng, L. Mesik, J. Zeng, H. Jiang, S. Wang, J. C. Looby, N. A. Guagliardo, L. W. Langma, J. Lu, Y. Zuo, D. A. Talmage, L. W. Role, P. Q. Barrett, L. I. Zhang, M. Luo, Y. Song, J. J. Zhu, and Y. Li, "A genetically encoded fluorescent acetylcholine indicator for *in vitro* and *in vivo* studies," *Nature Biotechnology*, vol. 36, pp. 726–737, 8 2018.

[91] F. Sun, J. Zeng, M. Jing, J. Zhou, J. Feng, S. F. Owen, Y. Luo, F. Li, H. Wang, T. Yamaguchi, Z. Yong, Y. Gao, W. Peng, L. Wang, S. Zhang, J. Du, D. Lin, M. Xu, A. C. Kreitzer, G. Cui, and Y. Li, "A genetically encoded fluorescent sensor enables rapid and specific detection of dopamine in flies, fish, and mice," *Cell*, vol. 174, pp. 481–496.e19, 7 2018.

[92] J. Feng, C. Zhang, J. E. Lischinsky, M. Jing, J. Zhou, H. Wang, Y. Zhang, A. Dong, Z. Wu, H. Wu, W. Chen, P. Zhang, J. Zou, S. A. Hires, J. J. Zhu, G. Cui, D. Lin, J. Du, and Y. Li, "A genetically encoded fluorescent sensor for rapid and specific in vivo detection of norepinephrine," *Neuron*, vol. 0, 3 2019.

[93] A. Colom, E. Derivery, S. Soleimanpour, C. Tomba, M. D. Molin, N. Sakai, M. González-Gaitán, S. Matile, and A. Roux, "A fluorescent membrane tension probe," *Nature Chemistry*, vol. 10, p. 1118, 11 2018.

[94] W. Wang, C. K. Kim, and A. Y. Ting, "Molecular tools for imaging and recording neuronal activity," *Nature Chemical Biology*, vol. 15, p. 101, 2 2019.

[95] E. S. Boyden, F. Zhang, E. Bamberg, G. Nagel, and K. Deisseroth, "Millisecond-timescale, genetically targeted optical control of neural activity," *Nature Neuroscience*, vol. 8, p. 1263, 9 2005.

[96] K. Deisseroth and P. Hegemann, "The form and function of channelrhodopsin," *Science*, vol. 357, p. eaan5544, 9 2017.

[97] C. K. Kim, A. Adhikari, and K. Deisseroth, "Integration of optogenetics with complementary methodologies in systems neuroscience," *Nature Reviews Neuroscience*, vol. 18, pp. 222–235, 4 2017.

[98] W. E. Allen, I. V. Kauvar, M. Z. Chen, E. B. Richman, S. J. Yang, K. Chan, V. Gradinaru, B. E. Deverman, L. Luo, and K. Deisseroth, "Global Representations of Goal-Directed Behavior in Distinct Cell Types of Mouse Neocortex," *Neuron*, vol. 94, pp. 891–907.e6, May 2017.

[99] O. A. Shemesh, D. Tanese, V. Zampini, C. Linghu, K. Piatkevich, E. Ronzitti, E. Papagiakoumou, E. S. Boyden, and V. Emiliani, "Temporally precise single-cell-resolution optogenetics," *Nature Neuroscience*, vol. 20, p. 1796, 12 2017.

[100] E. Ronzitti, C. Ventalon, M. Canepari, B. C. Forget, E. Papagiakoumou, and V. Emiliani, "Recent advances in patterned photostimulation for optogenetics," *Journal of Optics*, vol. 19, p. 113001, 10 2017.

[101] M. Mahn, L. Gibor, P. Patil, K. C.-K. Malina, S. Oring, Y. Printz, R. Levy, I. Lampl, and O. Yizhar, "High-efficiency optogenetic silencing with soma-targeted anion-conducting channelrhodopsins," *Nature Communications*, vol. 9, p. 4125, Oct. 2018.

[102] A. Forli, D. Vecchia, N. Binini, F. Succol, S. Bovetti, C. Moretti, F. Nespoli, M. Mahn, C. A. Baker, M. M. Bolton, O. Yizhar, and T. Fellin, "Two-Photon Bidirectional Control and Imaging of Neuronal Excitability with High Spatial Resolution In Vivo," *Cell Reports*, vol. 22, pp. 3087–3098, Mar. 2018.

[103] I.-W. Chen, E. Papagiakoumou, and V. Emiliani, "Towards circuit optogenetics," *Current Opinion in Neurobiology*, vol. 50, pp. 179–189, June 2018.

[104] T.-W. Chen, N. Li, K. Daie, and K. Svoboda, "A Map of Anticipatory Activity in Mouse Motor Cortex," *Neuron*, vol. 94, pp. 866–879.e4, May 2017.

[105] A. E. Cohen and S. L. Farhi, "Sculpting light to reveal brain function," *Nature Neuroscience*, vol. 21, p. 776, 6 2018.

[106] A. M. Stamatakis, M. J. Schachter, S. Gulati, K. T. Zitelli, S. Malanowski, A. Tajik, C. Fritz, M. Trulson, and S. L. Otte, "Simultaneous Optogenetics and Cellular Resolution Calcium Imaging During Active Behavior Using a Miniaturized Microscope," *Frontiers in Neuroscience*, vol. 12, 2018.

[107] J. P. Rickgauer, K. Deisseroth, and D. W. Tank, "Simultaneous cellular-resolution optical perturbation and imaging of place cell firing fields," *Nature Neuroscience*, vol. 17, pp. 1816–1824, 12 2014.

[108] A. M. Packer, L. E. Russell, H. W. P. Dalgleish, and M. Häusser, "Simultaneous all-optical manipulation and recording of neural circuit activity with cellular resolution *in vivo*," *Nature Methods*, vol. 12, pp. 140–146, 2 2015.

[109] L. Carrillo-Reid, W. Yang, Y. Bando, D. S. Peterka, and R. Yuste, "Imprinting and recalling cortical ensembles," *Science*, vol. 353, pp. 691–694, 8 2016.

[110] M. dal Maschio, J. C. Donovan, T. O. Helmbrecht, and H. Baier, "Linking Neurons to Network Function and Behavior by Two-Photon Holographic Optogenetics and Volumetric Imaging," *Neuron*, vol. 94, pp. 774–789.e5, May 2017.

[111] D. Förster, M. D. Maschio, E. Laurell, and H. Baier, "An optogenetic toolbox for unbiased discovery of functionally connected cells in neural circuits," *Nature Communications*, vol. 8, p. 116, July 2017.

[112] A. R. Mardinly, I. A. Oldenburg, N. C. Pégard, S. Sridharan, E. H. Lyall, K. Chesnov, S. G. Brohawn, L. Waller, and H. Adesnik, "Precise multimodal optical control of neural ensemble activity," *Nature Neuroscience*, vol. 21, p. 881, 6 2018.

[113] S. N. Chettih and C. D. Harvey, "Single-neuron perturbations reveal feature-specific competition in v1," *Nature*, vol. 567, p. 334, 3 2019.

[114] K. Podgorski and G. Ranganathan, "Brain heating induced by near-infrared lasers during multiphoton microscopy," *Journal of Neurophysiology*, vol. 116, pp. 1012–1023, 6 2016.

[115] A. Picot, S. Dominguez, C. Liu, I.-W. Chen, D. Tanese, E. Ronzitti, P. Berto, E. Papagiakoumou, D. Oron, G. Tessier, B. C. Forget, and V. Emiliani, "Temperature Rise under Two-Photon Optogenetic Brain Stimulation," *Cell Reports*, vol. 24, pp. 1243–1253.e5, July 2018.

[116] L. Z. Fan, R. Nehme, Y. Adam, E. S. Jung, H. Wu, K. Eggan, D. B. Arnold, and A. E. Cohen, "All-optical synaptic electrophysiology probes mechanism of ketamine-induced disinhibition," *Nature Methods*, vol. 15, p. 823, Oct. 2018.

[117] L. Z. Fan, S. Kheifets, U. L. Boehm, K. D. Piatkevich, H. Wu, V. Parot, M. Xie, E. S. Boyden, A. E. Takesian, and A. E. Cohen, "All-optical electrophysiology reveals excitation, inhibition, and neuromodulation in cortical layer 1," *bioRxiv*, p. 614172, Apr. 2019.

[118] L. Grosenick, J. H. Marshel, and K. Deisseroth, "Closed-Loop and Activity-Guided Optogenetic Control," *Neuron*, vol. 86, pp. 106–139, Apr. 2015.

[119] Z. Zhang, L. E. Russell, A. M. Packer, O. M. Gauld, and M. Häusser, "Closed-loop all-optical interrogation of neural circuits in vivo," *Nature Methods*, vol. 15, p. 1037, Dec. 2018.

[120] D. H. O'Connor, D. Huber, and K. Svoboda, "Reverse engineering the mouse brain," *Nature*, vol. 461, pp. 923–929, Oct. 2009.

[121] D. H. Hubel, "The brain," *Scientific American*, vol. 241, no. 3, pp. 45–53, 1979.

[122] V. Emiliani, A. E. Cohen, K. Deisseroth, and M. Häusser, "All-optical interrogation of neural circuits," *Journal of Neuroscience*, vol. 35, pp. 13917–13926, 10 2015.

[123] J. T. Ting, B. R. Lee, P. Chong, G. Soler-Llavina, C. Cobbs, C. Koch, H. Zeng, and E. Lein, "Preparation of acute brain slices using an optimized n-methyl-d-glucamine protective recovery method," *Journal of visualized experiments : JoVE*, vol. (132). doi, p. 10.3791/53825, 2 2018.

[124] X. Jiang, S. Shen, C. R. Cadwell, P. Berens, F. Sinz, A. S. Ecker, S. Patel, and A. S. Tolias, "Principles of connectivity among morphologically defined cell types in adult neocortex," *Science*, vol. 350, p. aac9462, 11 2015.

[125] M. T. Harnett, N.-L. Xu, J. C. Magee, and S. R. Williams, "Potassium channels control the interaction between active dendritic integration compartments in layer 5 cortical pyramidal neurons," *Neuron*, vol. 79, pp. 516–529, 8 2013.

[126] A. Blot and B. Barbour, "Ultra-rapid axon-axon ephaptic inhibition of cerebellar purkinje cells by the pinceau," *Nature Neuroscience*, vol. 17, pp. 289–295, 2 2014.

[127] C. J. Magnus, P. H. Lee, J. Bonaventura, R. Zemla, J. L. Gomez, M. H. Ramirez, X. Hu, A. Galvan, J. Basu, M. Michaelides, and S. M. Sternson, "Ultrapotent chemogenetics for research and potential clinical applications," *Science*, vol. 364, p. eaav5282, Apr. 2019.

[128] L. Petreanu, D. Huber, A. Sobczyk, and K. Svoboda, "Channelrhodopsin-2–assisted circuit mapping of long-range callosal projections," *Nature Neuroscience*, vol. 10, pp. 663–668, 5 2007.

[129] M. Inoue, A. Takeuchi, S.-i. Horigane, M. Ohkura, K. Gengyo-Ando, H. Fujii, S. Kamijo, S. Takemoto-Kimura, M. Kano, J. Nakai, K. Kitamura, and H. Bito, "Rational design of a high-affinity, fast, red calcium indicator r-camp2," *Nature Methods*, vol. 12, pp. 64–70, 1 2015.

[130] N. C. Klapoetke, Y. Murata, S. S. Kim, S. R. Pulver, A. Birdsey-Benson, Y. K. Cho, T. K. Morimoto, A. S. Chuong, E. J. Carpenter, Z. Tian, J. Wang, Y. Xie, Z. Yan, Y. Zhang, B. Y. Chow, B. Surek, M. Melkonian, V. Jayaraman, M. Constantine-Paton, G. K.-S. Wong, and E. S. Boyden, "Independent optical excitation of distinct neural populations," *Nature Methods*, vol. 11, pp. 338–346, 3 2014.

[131] T.-W. Chen, T. J. Wardill, Y. Sun, S. R. Pulver, S. L. Renninger, A. Baohan, E. R. Schreiter, R. A. Kerr, M. B. Orger, V. Jayaraman, L. L. Looger, K. Svoboda, and D. S. Kim, "Ultrasensitive fluorescent proteins for imaging neuronal activity," *Nature*, vol. 499, pp. 295–300, 7 2013.

[132] S. Klein, M. Staring, K. Murphy, M. A. Viergever, and J. P. W. Pluim, "elastix: A toolbox for intensity-based medical image registration," *IEEE Transactions on Medical Imaging*, vol. 29, pp. 196–205, 1 2010.

[133] Y.-L. Huang, A. S. Walker, and E. W. Miller, "A photostable silicon rhodamine platform for optical voltage sensing," *Journal of the American Chemical Society*, vol. 137, pp. 10767–10776, 8 2015.

[134] J. Freeman, N. Vladimirov, T. Kawashima, Y. Mu, N. J. Sofroniew, D. V. Bennett, J. Rosen, C. T. Yang, L. L. Looger, and M. B. Ahrens, "Mapping brain activity at scale with cluster computing," *Nature methods*, vol. 11, pp. 941–950, 9 2014.

[135] O. Skocek, T. Nöbauer, L. Weilguny, F. M. Traub, C. N. Xia, M. I. Molodtsov, A. Grama, M. Yamagata, D. Aharoni, D. D. Cox, P. Golshani, and A. Vaziri, "High-speed volumetric

imaging of neuronal activity in freely moving rodents," *Nature Methods*, vol. 15, p. 429, 6 2018.

[136] A. Eder and H. Bading, "Calcium signals can freely cross the nuclear envelope in hippocampal neurons: somatic calcium increases generate nuclear calcium transients," *BMC neuroscience*, vol. 8, p. 57, 7 2007.

[137] C. P. Bengtson, H. E. Freitag, J. M. Weislogel, and H. Bading, "Nuclear calcium sensors reveal that repetition of trains of synaptic stimuli boosts nuclear calcium signaling in ca1 pyramidal neurons," *Biophysical journal*, vol. 99, pp. 4066–4077, 12 2010.

[138] J. Mazzaferri, D. Kunik, J. M. Belisle, K. Singh, S. Lefrançois, and S. Costantino, "Analyzing speckle contrast for hilo microscopy optimization," *Optics Express*, vol. 19, pp. 14508–14517, 7 2011.

[139] D. Lim, K. K. Chu, and J. Mertz, "Wide-field fluorescence sectioning with hybrid speckle and uniform-illumination microscopy," *Optics letters*, vol. 33, no. 16, pp. 1819–1821, 2008.

[140] M. J. Gunthorpe, C. H. Large, and R. Sankar, "The mechanism of action of retigabine (ezogabine), a first-in-class k+ channel opener for the treatment of epilepsy," *Epilepsia*, vol. 53, pp. 412–424, 3 2012.

[141] E. S. Lein, M. J. Hawrylycz, N. Ao, M. Ayres, A. Bensinger, A. Bernard, A. F. Boe, M. S. Boguski, K. S. Brockway, E. J. Byrnes, L. Chen, L. Chen, T.-M. Chen, M. Chi Chin, J. Chong, B. E. Crook, A. Czaplinska, C. N. Dang, S. Datta, N. R. Dee, A. L. Desaki, T. Desta, E. Diep, T. A. Dolbeare, M. J. Donelan, H.-W. Dong, J. G. Dougherty, B. J. Duncan, A. J. Ebbert, G. Eichele, L. K. Estin, C. Faber, B. A. Facer, R. Fields, S. R. Fischer, T. P. Fliss, C. Frensley, S. N. Gates, K. J. Glattfelder, K. R. Halverson, M. R. Hart, J. G. Hohmann, M. P. Howell, D. P. Jeung, R. A. Johnson, P. T. Karr, R. Kawal, J. M. Kidney, R. H. Knapik, C. L. Kuan, J. H. Lake, A. R. Laramee, K. D. Larsen, C. Lau, T. A. Lemon, A. J. Liang, Y. Liu, L. T. Luong, J. Michaels, J. J. Morgan, R. J. Morgan, M. T. Mortrud, N. F. Mosqueda, L. L. Ng, R. Ng, G. J. Orta, C. C. Overly, T. H. Pak, S. E. Parry, S. D. Pathak, O. C. Pearson, R. B. Puchalski, Z. L. Riley, H. R. Rockett, S. A. Rowland, J. J. Royall, M. J. Ruiz, N. R. Sarno, K. Schaffnit, N. V. Shapovalova, T. Sivisay, C. R. Slaughterbeck, S. C. Smith, K. A. Smith, B. I. Smith, A. J. Sodt, N. N. Stewart, K.-R. Stumpf, S. M. Sunkin, M. Sutram, A. Tam, C. D. Teemer, C. Thaller, C. L. Thompson, L. R. Varnam, A. Visel, R. M. Whitlock, P. E. Wohnoutka, C. K. Wolkey, V. Y. Wong, M. Wood, M. B. Yaylaoglu,

R. C. Young, B. L. Youngstrom, X. Feng Yuan, B. Zhang, T. A. Zwingman, and A. R. Jones, "Genome-wide atlas of gene expression in the adult mouse brain," *Nature*, vol. 445, pp. 168–176, 1 2007.

[142] M. J. Saganich, E. Machado, and B. Rudy, "Differential expression of genes encoding subthreshold-operating voltage-gated k+ channels in brain," *The Journal of neuroscience : the official journal of the Society for Neuroscience*, vol. 21, pp. 4609–4624, 7 2001.

[143] L. A. Ibrahim, L. Mesik, X. Y. Ji, Q. Fang, H. F. Li, Y. T. Li, B. Zingg, L. I. Zhang, and H. W. Tao, "Cross-modality sharpening of visual cortical processing through layer-1-mediated inhibition and disinhibition," *Neuron*, vol. 89, pp. 1031–1045, 3 2016.

[144] Y. W. Wu, J. I. Kim, V. L. Tawfik, R. R. Lalchandani, G. Scherrer, and J. B. Ding, "Input- and cell-type-specific endocannabinoid-dependent ltd in the striatum," *Cell reports*, vol. 10, pp. 75–87, 1 2015.

[145] A. Saunders, C. Johnson, and B. Sabatini, "Novel recombinant adeno-associated viruses for cre activated and inactivated transgene expression in neurons," *Frontiers in Neural Circuits*, vol. 6, 2012.

[146] W. Afshar Saber, F. M. Gasparoli, M. G. Dirks, F. J. Gunn-Moore, and M. Antkowiak, "All-optical assay to study biological neural networks," *Frontiers in Neuroscience*, vol. 12, 2018.

[147] Y. Kozorovitskiy, R. Peixoto, W. Wang, A. Saunders, and B. L. Sabatini, "Neuromodulation of excitatory synaptogenesis in striatal development," *eLife*, vol. 4, p. e10111, 11 2015.

[148] A. Naka and H. Adesnik, "Inhibitory circuits in cortical layer 5," *Frontiers in Neural Circuits*, vol. 10, 2016.

[149] H. Adesnik, "Layer-specific excitation/inhibition balances during neuronal synchronization in the visual cortex," *The Journal of Physiology*, vol. 596, no. 9, pp. 1639–1657, 2018.

[150] G. Szalay, L. Judak, G. Katona, K. Ocsai, G. Juhasz, M. Veress, Z. Szadai, A. Feher, T. Tompa, B. Chiovini, P. Maak, and B. Rozsa, "Fast 3d imaging of spine, dendritic, and neuronal assemblies in behaving animals," *Neuron*, vol. 92, pp. 723–738, 10 2016.

[151] K. Y. Chan, M. J. Jang, B. B. Yoo, A. Greenbaum, N. Ravi, W. L. Wu, L. Sanchez-Guardado, C. Lois, S. K. Mazmanian, B. E. Deverman, and V. Gradinaru, "Engineered

aavs for efficient noninvasive gene delivery to the central and peripheral nervous systems," *Nature neuroscience*, vol. 20, pp. 1172–1179, 8 2017.

[152] S. L. Farhi, V. J. Parot, A. Grama, M. Yamagata, A. S. Abdelfattah, Y. Adam, S. Lou, J. J. Kim, R. E. Campbell, D. D. Cox, and A. E. Cohen, "Wide-area all-optical neurophysiology in acute brain slices," *Journal of Neuroscience*, pp. 0168–19, Apr. 2019.

[153] M. Tribus and E. C. McIrvine, "Energy and information," *Scientific American*, vol. 225, no. 3, pp. 179–188, 1971.

[154] E. A. Rodriguez, R. E. Campbell, J. Y. Lin, M. Z. Lin, A. Miyawaki, A. E. Palmer, X. Shu, J. Zhang, and R. Y. Tsien, "The growing and glowing toolbox of fluorescent and photoactive proteins," *Trends in biochemical sciences*, vol. 42, no. 2, pp. 111–129, 2017.

[155] V. Sample, S. Mehta, and J. Zhang, "Genetically encoded molecular probes to visualize and perturb signaling dynamics in living biological systems," *J Cell Sci*, vol. 127, no. 6, pp. 1151–1160, 2014.

[156] M. Saxena, G. Eluru, and S. S. Gorthi, "Structured illumination microscopy," *Advances in Optics and Photonics*, vol. 7, no. 2, pp. 241–275, 2015.

[157] E. A. Pnevmatikakis, D. Soudry, Y. Gao, T. A. Machado, J. Merel, D. Pfau, T. Reardon, Y. Mu, C. Lacefield, W. Yang, *et al.*, "Simultaneous denoising, deconvolution, and demixing of calcium imaging data," *Neuron*, vol. 89, no. 2, pp. 285–299, 2016.

[158] T. Nöbauer, O. Skocek, A. J. Pernía-Andrade, L. Weilguny, F. M. Traub, M. I. Molodtsov, and A. Vaziri, "Video rate volumetric ca 2+ imaging across cortex using seeded iterative demixing (sid) microscopy," *Nature methods*, vol. 14, no. 8, p. 811, 2017.

[159] N. C. Pégard, H.-Y. Liu, N. Antipa, M. Gerlock, H. Adesnik, and L. Waller, "Compressive light-field microscopy for 3d neural activity recording," *Optica*, vol. 3, no. 5, pp. 517–524, 2016.

[160] T. W. Dunn, Y. Mu, S. Narayan, O. Randlett, E. A. Naumann, C.-T. Yang, A. F. Schier, J. Freeman, F. Engert, and M. B. Ahrens, "Brain-wide mapping of neural activity controlling zebrafish exploratory locomotion," *Elife*, vol. 5, p. e12741, 2016.

[161] D. W. Tufts, R. Kumaresan, and I. Kirsteins, "Data adaptive signal estimation by singular value decomposition of a data matrix," *Proceedings of the IEEE*, vol. 70, no. 6, pp. 684–685, 1982.

[162] T. Furnival, R. K. Leary, and P. A. Midgley, "Denoising time-resolved microscopy image sequences with singular value thresholding," *Ultramicroscopy*, vol. 178, pp. 112–124, 2017.

[163] S. Lou, Y. Adam, E. N. Weinstein, E. Williams, K. Williams, V. Parot, N. Kavokine, S. Liberles, L. Madisen, H. Zeng, *et al.*, "Genetically targeted all-optical electrophysiology with a transgenic cre-dependent optopatch mouse," *Journal of Neuroscience*, vol. 36, no. 43, pp. 11059–11073, 2016.

[164] M. A. Lauterbach, E. Ronzitti, J. R. Sternberg, C. Wyart, and V. Emiliani, "Fast calcium imaging with optical sectioning via hilo microscopy," *PloS one*, vol. 10, p. e0143681, 12 2015.

[165] V. Studer, J. Bobin, M. Chahid, H. S. Mousavi, E. Candès, and M. Dahan, "Compressive fluorescence microscopy for biological and hyperspectral imaging," *Proceedings of the National Academy of Sciences*, vol. 109, no. 26, pp. E1679–E1687, 2012.

[166] L. Zhu, W. Zhang, D. Elnatan, and B. Huang, "Faster storm using compressed sensing," *Nature methods*, vol. 9, no. 7, p. 721, 2012.

[167] W. Meiniel, P. Spinicelli, E. D. Angelini, A. Fragola, V. Loriette, F. Orieux, E. Sepulveda, and J. Olivo-Marin, "Reducing data acquisition for fast structured illumination microscopy using compressed sensing," in *2017 IEEE 14th International Symposium on Biomedical Imaging (ISBI 2017)*, pp. 32–35, April 2017.

[168] V. J. Parot, C. Sing-Long, Y. Adam, U. L. Böhm, L. Z. Fan, S. L. Farhi, and A. E. Cohen, "Compressed hadamard microscopy for high-speed optically sectioned neuronal activity recordings," *Journal of Physics D: Applied Physics*, vol. 52, p. 144001, 2 2019.

[169] K. Fazel, "Performance of CDMA/OFDM for mobile communication system," in *Proceedings of 2nd IEEE International Conference on Universal Personal Communications*, vol. 2, pp. 975–979 vol.2, Oct. 1993.

[170] LIGO Scientific Collaboration and Virgo Collaboration, "Observation of Gravitational Waves from a Binary Black Hole Merger," *Physical Review Letters*, vol. 116, p. 061102, Feb. 2016.

[171] M. Lustig, D. Donoho, and J. M. Pauly, "Sparse MRI: The application of compressed sensing for rapid MR imaging," *Magnetic Resonance in Medicine*, vol. 58, pp. 1182–1195, Dec. 2007.

[172] The Event Horizon Telescope Collaboration, "First M87 Event Horizon Telescope Results. IV. Imaging the Central Supermassive Black Hole," *The Astrophysical Journal Letters*, p. 52, 2019.

[173] E. Candes and M. Wakin, "An Introduction To Compressive Sampling," *IEEE Signal Processing Magazine*, vol. 25, pp. 21–30, Mar. 2008.

[174] F. H. Yu, M. Mantegazza, R. E. Westenbroek, C. A. Robbins, F. Kalume, K. A. Burton, W. J. Spain, G. S. McKnight, T. Scheuer, and W. A. Catterall, "Reduced sodium current in GABAergic interneurons in a mouse model of severe myoclonic epilepsy in infancy," *Nature Neuroscience*, vol. 9, p. 1142, Sept. 2006.

[175] C. W. Ang, G. C. Carlson, and D. A. Coulter, "Massive and Specific Dysregulation of Direct Cortical Input to the Hippocampus in Temporal Lobe Epilepsy," *Journal of Neuroscience*, vol. 26, pp. 11850–11856, Nov. 2006.